Passive source reverse time migration based on the spectral element method

Bin He[1], Yu Chen[1], David E Lumley[1], Qinya Liu[2], Nozomu Takeuchi[3], Hitoshi Kawakatsu[4], and Hejun Zhu[1]

[1]University of Texas at Dallas
[2]University of Toronto
[3]University of Tokyo
[4]Earthquake Research Institute, The University of Tokyo

December 1, 2023

Abstract

Increasing deployment of dense arrays has facilitated detailed structure imaging for tectonic investigation, hazard assessment and resource exploration. Strong velocity heterogeneity and topographic changes have to be considered during passive source imaging. However, it is quite challenging for ray-based methods, such as Kirchhoff migration or the widely used teleseismic receiver function, to handle these problems. In this study, we propose a 3-D passive source reverse time migration strategy based on the spectral element method. It is realized by decomposing the time reversal full elastic wavefield into amplitude-preserved vector P and S wavefields by solving the corresponding weak-form solutions, followed by a dot-product imaging condition to get images for the subsurface structures. It enables us to use regional 3-D migration velocity models and take topographic variations into account, helping us to locate reflectors at more accurate positions than traditional 1-D model-based methods, like teleseismic receiver functions. Two synthetic tests are used to demonstrate the advantages of the proposed method to handle topographic variations and complex velocity heterogeneities. Furthermore, applications to the Laramie array data using both teleseismic P and S waves enable us to identify several south-dipping structures beneath the Laramie basin in southeast Wyoming, which are interpreted as the Cheyenne Belt suture zone and agree with, and improve upon previous geological interpretations.

Passive source reverse time migration based on the spectral element method

Bin He[1], **Yu Chen**[1], **David Lumley**[1,2], **Qinya Liu**[3,4], **Nozomu Takeuchi**[5], **Hitoshi Kawakatsu**[5], **and Hejun Zhu**[1,2]

[1]Department of Geosciences, The University of Texas at Dallas, Richardson, TX 75080, USA
[2]Department of Physics, The University of Texas at Dallas, Richardson, TX 75080, USA
[3]Department of Physics, University of Toronto, Toronto M5S 1A7, Canada
[4]Department of Earth Sciences, University of Toronto, Toronto M5S 3B1, Canada
[5]Earthquake Research Institute, University of Tokyo, Tokyo 1130032, Japan

Key Points:

- A 3-D passive source reverse time migration based on the spectral element method is proposed to image complex structures.
- Amplitude-preserved vector P and S wavefields are accurately decomposed by solving corresponding weak-form solutions.
- Several south-dipping structures can be identified from P and S migration results beneath the Laramie basin, which are interpreted as the Cheyenne Belt suture zone.

Corresponding author: Hejun Zhu, `hejun.zhu@utdallas.edu`

Abstract

Increasing deployment of dense arrays has facilitated detailed structure imaging for tectonic investigation, hazard assessment and resource exploration. Strong velocity heterogeneity and topographic changes have to be considered during passive source imaging. However, it is quite challenging for ray-based methods, such as Kirchhoff migration or the widely used teleseismic receiver function, to handle these problems. In this study, we propose a 3-D passive source reverse time migration strategy based on the spectral element method. It is realized by decomposing the time reversal full elastic wavefield into amplitude-preserved vector P and S wavefields by solving the corresponding weak-form solutions, followed by a dot-product imaging condition to get images for the subsurface structures. It enables us to use regional 3-D migration velocity models and take topographic variations into account, helping us to locate reflectors at more accurate positions than traditional 1-D model-based methods, like teleseismic receiver functions. Two synthetic tests are used to demonstrate the advantages of the proposed method to handle topographic variations and complex velocity heterogeneities. Furthermore, applications to the Laramie array data using both teleseismic P and S waves enable us to identify several south-dipping structures beneath the Laramie basin in southeast Wyoming, which are interpreted as the Cheyenne Belt suture zone and agree with, and improve upon previous geological interpretations.

Plain Language Summary

Increasing deployment of dense arrays has allowed detailed structure imaging for tectonic investigation, hazard assessment and resource exploration. However, traditional ray-based migration methods or 1-D velocity model-based receiver function methods may greatly degrade the imaging quality without considering the full wavefield propagation effect and velocity heterogeneities. Therefore, in this study, we develop a 3-D passive source migration based on the spectral element method, which is capable of handling topographic variations as well as complex velocity heterogeneities for real data applications. Several synthetic tests and applications to the Laramie array data using both teleseismic P and S waves are used to demonstrate the capability of our method to image complex structures, such as subduction and suture zones.

1 Introduction

In past decades, teleseismic receiver functions have been widely used for imaging discontinuities within the Earth's crust and upper mantle (Burdick & Langston, 1977; Langston & Corvallis, 1977; Vinnik, 1977; Ai et al., 2007; Kawakatsu & Watada, 2007; Kind et al., 2012; H. Zhang et al., 2016; Long et al., 2019). Based on the assumption of a 1-D Earth model where discontinuities are horizontal, common convert point stacking (Dueker & Sheehan, 1997; L. Zhu, 2000; Gilbert et al., 2003) has generally been used to improve the image quality by mapping the receiver functions to depths. In the case of a single station, like the SEIS on Mars (Banerdt et al., 2020; Knapmeyer-Endrun et al., 2020; Lognonné et al., 2020) or sparse station distributions such as the USArray (Meltzer et al., 1999), such simplifications are natural and useful. However, it indeed degrades the image quality of geologically complex structures, such as subsurface environments with steep faults and laterally discontinuous interfaces, without considering the effects of wavefield diffraction and scattering caused by lateral variations of impedance contracts and velocities (L. Chen et al., 2005; Shang et al., 2012). In addition, increasing deployment of dense and nodal arrays has facilitated detailed structure imaging for tectonic investigation, hazard assessment and resource exploration (Okada et al., 2004; Zheng et al., 2008; Nábělek et al., 2009; H. Zhang et al., 2016; X. Yang et al., 2017; X. Chen et al., 2018; Li et al., 2018; Clayton et al., 2019; X. Wang et al., 2021; Onyango et al., 2022; Wu et al., 2023). Therefore, it calls for advanced imaging methods, such as seismic migration/inversion, which exploit the full complexity of recorded wavefields and rely less on a priori information about the Earth's structures, to get accurate images of complex subsurface discontinuities (Sheehan et al., 2000; L. Chen et al., 2005; Shang et al., 2012; Cheng et al., 2016; Li et al., 2018; Millet et al., 2019).

Among many seismic migration approaches, Kirchhoff migration/inversion (Schneider, 1978; Gray & May, 1994) has been widely used in the oil and gas industry to image shallow sedimentary structures owing to its high efficiency and simplicity. It was later introduced to global seismology for imaging large-scale structures using multi-component teleseismic data recorded by local dense arrays (Burridge et al., 1998; Bostock, 1998; Bostock & Rondenay, 1999; Rondenay et al., 2000; Bostock et al., 2001; Bostock, 2002; Levander et al., 2005; Rondenay, 2009; Liu & Levander, 2013; Cheng et al., 2016; Millet et al., 2019). Teleseismic Kirchhoff migration/inversion is implemented by weighting and stacking data along diffraction hyperbola for every possible scattering point in a regular grid

(Schneider, 1978; Gray & May, 1994; Bostock et al., 2001; Cheng et al., 2016; Millet et al., 2019). To date, most Kirchhoff migration/inversion approaches are based on the infinite high-frequency assumption by neglecting the finite frequency property of seismic wave propagation, which enables us to efficiently get images by using ray tracing (Richards & Aki, 1980) or solving the Eikonal equation (Gray & May, 1994; Cheng et al., 2016). However, It is difficult for ray-tracing to handle multiple arrivals, shadow zones, and even chaotic rays in complex subsurface environments (Audebert et al., 1997; L. Chen et al., 2005). Although the Eikonal equation-based Kirchhoff migration is capable of dealing with complex structures, it is not easy to handle the multipathing challenge (H. Zhao, 2005; Waheed et al., 2015; Tong, 2021). Furthermore, Kirchhoff migration requires more efforts to correct image amplitudes, and therefore, the wave-equation Kirchhoff migration has been developed to balance accuracy and efficiency (Andrade et al., n.d.; Jin & Etgen, n.d.). To mitigate the finite-frequency, multi-arrivals and inaccurate amplitude problems, Gaussian beam migration (Hill, 1990, 2001) has been proposed to apply local slant stacks by using complex-valued traveltimes and amplitudes. These complex quantities come from the approximation of seismic wave propagation with a sum of Gaussian beams, which are finite-frequency, ray-theoretical approximations to the wave equation (Notfors et al., n.d.). It is further extended to the wave-equation-based two-way beam wave method, which has comparable accuracy and efficiency in comparison to the wave-equation-based methods (J. Yang et al., 2022).

On the other hand, wave equation-based migration methods can essentially avoid most difficulties from the ray-based method by using the full wavefields (Claerbout, 1985). Among many different types of wave equation-based migration methods, synthetic and field experiments have shown that reverse-time migration (RTM) (Baysal et al., 1983; Whitmore, 1983; McMechan, 1983) has better performance for imaging complex structures. Active source RTM includes a forward wavefield modeling from the source and a backward wavefield modeling from the receivers, followed by applying imaging conditions to these two wavefields. In contrast, passive source RTM only requires one backward wavefield modeling for each earthquake. Therefore, inaccuracies due to source locations and velocity variations between earthquake locations and local study regions could be neglected. During the wavefield back-propagation, P and S wavefields are usually separated by polarization decomposition (Shang et al., 2012; H. Zhu, 2017; J. Yang et al., 2018). Then, the imaging condition is applied to cross-correlate separated P and S wavefields, followed by the summation of individual events. As pointed out by Shang et al. (2012), passive source RTM of converted waves differs fundamentally from single station receiver function analysis, and also in several important ways from more traditional receiver function migration (L. Chen et al., 2005). However, both current 2-D and 3-D pioneer works are based on the finite difference method, which requires projecting station locations on the model grids, and it is not easy to handle complex topography in real applications (Rajasekaran & McMechan, 1995; Bevc, 1997; Shragge, 2014; Shang et al., 2017; Yi et al., 2019). In addition, there are few real data applications for 3-D passive source RTM to image crustal and uppermost mantle structures.

In this study, we combine passive source RTM with the spectral-element method (SEM) (Komatitsch & Vilotte, 1998; Fichtner et al., 2009). Owning to its advantages in handling complex topographic variations, wavefield coupling between different media, flexibility to handle station distributions and so on, the SEM has been widely applied to construct crustal and mantle velocity models at regional and global scales (Tromp et al., 2005; Fichtner et al., 2009; Tape et al., 2009; Fichtner, 2010; Liu & Levander, 2013; H. Zhu et al., 2012; Y. Wang et al., 2016; K. Wang et al., 2020, 2021; Tromp, 2020; H. Zhu et al., 2020; Maguire et al., 2022). Here, we use it for passive source RTM. Because the wave-equation is solved in a weak-form fashion in SEM, directly taking strong-form spatial derivatives for wavefield decomposition results in significant discontinuities between element boundaries. To solve this problem, we propose to solve the corresponding weak-form solutions for P and S wavefield decomposition. This paper is organized into the following parts, we first briefly review passive source RTM based on the wavefield decomposition, followed by the theory of weak-form solutions for wavefield decomposition, and then several synthetic tests are used to demonstrate the advantages of the proposed method. Finally, we apply it to the Laramie array for suture zone imaging.

2 Methodology

2.1 Passive source RTM based on vector wavefield decomposition

Based on the principle that all back-propagating direct P and S receiver wavefields ($\mathbf{u}^P$ and $\mathbf{u}^S$) should coincide at “source” locations, wave-equation-based passive source imaging seeks strong energy in space as the source locations (McMechan, 1982; Nakata & Beroza, 2016; J. Yang et al., 2020; Duan et al., 2021). Similarly, the vector $\mathbf{u}^P$ and

$\mathbf{u}^S$ wavefields constructed by back-propagating multichannel direct P and Ps converted (or direct S and Sp converted) seismograms, should coincide at the scattering locations in depths, such as the Moho (Shang et al., 2012; Li et al., 2018). The imaging condition can be given as

$$I(\mathbf{x}) = \sum_{i_e=1}^{Ne} \int_{t=0}^{T} \boldsymbol{u}(\mathbf{x})_{i_e}^{P}(t) \cdot \boldsymbol{u}(\mathbf{x})_{i_e}^{S}(t) dt \quad , \tag{1}$$

where $I(\mathbf{x})$ is the image, $\boldsymbol{u}(\mathbf{x})_{i_e}^{P}$ and $\boldsymbol{u}(\mathbf{x})_{i_e}^{S}$ are the constructed vector P and S wavefields for i_eth event at the spatial coordinate $\mathbf{x}$. N_e is the total number of events for imaging. t represents the current time and T denotes the total time for wavefield back-propagation. " $\cdot$ " denotes the dot product between two vector fields. The final image is obtained by summing over all the time steps during wavefield back-propagation and all seismic events.

Because the vector $\mathbf{u}^P$ and $\mathbf{u}^S$ wavefields are coupled during elastic wavefield simulations, one may consider back-propagate multichannel P and Ps (or S and Sp) seismograms independently by solving two acoustic wave-equations (Sun et al., 2004; Duan et al., 2021) or decouple them during the wavefield back-propagation. H. Zhu (2017) proposed an amplitude-preserved wavefield decomposition method to decouple the vector $\mathbf{u}^P$ and $\mathbf{u}^S$ from elastic wavefield $\mathbf{u}$ by introducing a vector $\mathbf{w}$ in the form of

$$\nabla^2 \mathbf{w} = \mathbf{u} = \mathbf{u}^P + \mathbf{u}^S \quad , \tag{2}$$

where vector P and S wavefields can be obtained according to

$$\mathbf{u}^P = \nabla(\nabla \cdot \mathbf{w}), \quad \mathbf{u}^S = -\nabla \times \nabla \times \mathbf{w} \quad . \tag{3}$$

Here ∇, $\nabla\cdot$ and $\nabla\times$ are the gradient, divergence and curl operators, respectively. However, solving Equation 3 requires explicitly solving the Poisson's equation in Equation 2. To reduce the computational costs, J. Yang et al. (2018) further extended this method to avoid solving Poisson's equation under the isotropic media assumption with

$$\mathbf{u}^P = \nabla(\nabla \cdot \alpha^2 \hat{\mathbf{u}}), \quad \mathbf{u}^S = -\nabla \times (\nabla \times \beta^2 \hat{\mathbf{u}}) \quad , \tag{4}$$

where $\hat{\mathbf{u}}$ denotes the extrapolated wavefield excited by a double integral of the original seismograms, α and β are the local P and S velocities, respectively.

2.2 Strong- and weak-form solutions for the wavefield decomposition

In this section, we introduce H. Zhu (2017) and J. Yang et al. (2018)'s method to the SEM, so that it is more convenient to handle irregular surface topography and station locations. Different from the finite difference (FD) method, SEM seeks a weak solution $\bar{\boldsymbol{u}}(\mathbf{x}, t)$ to the equation of motion in the Galerkin sense (Komatitsch & Vilotte, 1998; Fichtner, 2010). Lagrange polynomials collocated at the Gauss–Lobatto–Legendre(GLL) points are used to interpolate the wavefield at any spatial locations in the form of

$$\boldsymbol{u}(\mathbf{x}, t) \approx \bar{\boldsymbol{u}}(\mathbf{x}, t) = \sum_{i,j,k=1}^{N+1} \boldsymbol{u}^{ijk}(t) L_{ijk}(\mathbf{x}) \quad , \tag{5}$$

where $\boldsymbol{u}(\mathbf{x}, t)$ and $\bar{\boldsymbol{u}}(\mathbf{x}, t)$ represent the true and weak-form solutions of the wave-equation, respectively. $\mathbf{x}$ represents the spatial coordinate and t represents time. N denotes the degree of the Lagrange polynomials, and therefore we have $N+1$ GLL points for one element along each direction. $L_{ijk} = l_i(x)l_j(y)l_k(z)$ represents the basis function chosen as the product of three Lagrange polynomials $l(x)$, $l(y)$ and $l(z)$ along the x, y and z directions collocated at the corresponding GLL points.

Owing to the continuous prosperities of the Lagrange polynomials, a straightforward solution of Equation 4 based on SEM, noted as the strong-form solution, can be realized by

$$\mathbf{u}^P = \nabla[\nabla \cdot \alpha^2 \sum_{i,j,k=1}^{N+1} \boldsymbol{u}^{ijk}(t) L_{ijk}(\mathbf{x})], \quad \mathbf{u}^S = -\nabla \times [(\nabla \times \beta^2 \sum_{i,j,k=1}^{N+1} \boldsymbol{u}^{ijk}(t) L_{ijk}(\mathbf{x})] \quad , \tag{6}$$

which is fairly easy to implement because the spatial derivatives from the gradient, divergence and curl operators are taken from the Lagrange polynomials. However, we expect quite strong artifacts in the separated vector wavefields, which could contaminate the final imaging result. As illustrated in Figure 1, strong S mode artifacts appear in the P mode. This is because the solution of SEM is a weak-form approximation, and although the wavefield is continuous cross elements, the continuity of spatial derivatives is not guaranteed. To mitigate this leakage during wavefield decomposition, we use the weak solutions for Equation 4 as follows:

$$\int_{G_e} \mathbf{\Phi} \cdot \mathbf{u}^P d^3\mathbf{x} = \int_{G_e} \mathbf{\Phi} \cdot \nabla(\nabla \cdot \alpha^2 \mathbf{u}) d^3\mathbf{x} = -\int_{G_e} [\nabla \cdot \mathbf{\Phi}][\nabla \cdot (\alpha^2 \mathbf{u})] \quad , \tag{7}$$

$$\int_{G_e} \mathbf{\Phi} \cdot \mathbf{u}^S d^3\mathbf{x} = -\int_{G_e} \mathbf{\Phi} \cdot \nabla \times (\nabla \times \beta^2 \mathbf{u}) d^3\mathbf{x} = \int_{G_e} [\nabla \times \mathbf{\Phi}] \cdot [\nabla \times \beta^2 \mathbf{u}] d^3\mathbf{x} \quad , \tag{8}$$

where $\mathbf{\Phi}$ denotes any arbitrary, differentiable, time-independent test function, which will be chosen as the basis functions similar to the way we get SEM solutions. As shown in Figure 2, both P and S modes are clearly separated without significant leakages. This indicates that the weak-form solutions can significantly improve the quality of wavefield decomposition, which is the basis for the following imaging tests. The deviations of Equations 7 and 8 can be found in the supplementary material.

2.3 The workflow for passive source RTM

The implementation of passive source RTM can be summarised in the following four steps:

1. Teleseimic data preprocessing. During this step, we estimate source time functions for each teleseismic event based on the principle component analysis for the aligned incident waves (Bostock & Rondenay, 1999; Shang et al., 2017), such as P, S or SKS waves. For this purpose, the incident waves are aligned according to the onset time of the incident phases estimated using the TauP package (Crotwell et al., 1999). Then, an iterative time deconvolution (Kikuchi & Kanamori, 1982) is applied to each component of original(unaligned) data to remove the source time function, followed by bandpass filtering for later finite frequency simulations.
2. Injecting the preprocessed teleseismic data for the SEM solver as adjoint sources to the acceleration vector. Given the linear relation between the source time function and wavefield, this step further avoids obtaining the double integral of the teleseismic data, which should be injected to construct the second time integral of the displacement wavefield indicated by Equation 4.
3. During the reverse time wavefield propagation, solving the weak-form solutions shown in Equations 7 and 8 to get vector wavefields $\mathbf{u}_{i_e}^P$ and $\mathbf{u}_{i_e}^S$, followed by applying the zero-lag cross-correlation imaging condition (Equation 1), noted as $\mathbf{I}_{ie}^{PS}$. To save computational costs, one may consider performing wavefield separation for every several time steps according to the Nyquist rule. We also apply the imaging condition to $\mathbf{u}_{i_e}^P$ with $\mathbf{u}_{i_e}^P$ to get the PP image as $\mathbf{I}_{i_e}^{PP}$.
4. Sum all corresponding event images to obtain $\mathbf{I}_{PS}$ and $\mathbf{I}_{PP}$, and then get the image with $\mathbf{I}_{PS} = \frac{\mathbf{I}_{PS}}{\mathbf{I}_{PP}+\epsilon}$ to compensate for energies at great depths. Here, ϵ is a small damping value used to avoid dividing by zeros.

3 Applications

In this section, we use two synthetic tests and one real data example to validate our method based on linear array recordings although we are using 3-D modeling and migration. It is well-known that station spacing together with the data frequency are important factors that may result in spatial aliasing during passive source RTM (Gray, 2013; Shang et al., 2012). Therefore, most teleseismic migration methods used to image lithospheric structures rely on dense arrays (station spacing is ∼5 km) (Bostock, 1998; Rondenay et al., 2000; Rondenay, 2009; Shang et al., 2017). Therefore, all synthetic simulations in our tests are implemented using a 3-D plane-wave injection method, FK-SEM (Tong, Komatitsch, et al., 2014; Tong, Chen, et al., 2014) and recorded by a dense linear array. Then, passive source RTM is implemented based on 3-D migration. We note here, there are mainly three advantages to implement 3-D rather than 2-D migration even using recordings from a linear array: 1) no 3-D/2-D transformation is needed ("Line-source simulation for shallow-seismic data. Part 1: Theoretical background, author=Forbriger, Thomas and Groos, Lisa and Schäfer, Martin", 2014; Schäfer et al., 2014; C. Zhang et al., 2018), which is important to correct phase and amplitude differences between 3-D and 2-D simulations; 2) more teleseismic events can be chosen for real data applications; 3) no needs to project stations onto a line, which is required for 2-D migration even with linear arrays because their locations are not critically located on 2-D linear mesh grid (Shang et al., 2017).

3.1 Synthetic test 1: effects of topographic variations

The first synthetic test is used to highlight the effects of topographic variations on passive source migration when using high-frequency teleseismic data. The input model is a two-layer model with an interface at 30 km depth. The density, Vp and Vs for the first layer between 0 and 30 km depth are 2.72 g/cm^3, 5.8 km/s and 3.46 km/s, which are 3.423 g/cm^3, 8.06 km/s and 4.53 km/s between 30 and 60 km depths. These values are taken from the AK135 model (Kennett et al., 1995). The simulation domain spans -90 to 90 km along the X (longitude) direction, -60 to 60 km along the Y (latitude) direction and 0 to 60 km along the depth direction. The element size is 1.0 km, which allows for the wavefield simulation with the highest frequency around 3.0 Hz. The Stacey absorption boundary condition is used for each face of the model except for the top, which is a free-surface boundary condition for our simulations (Mahrer, 1990). A 1.5-D topographic change (no change along the Y direction) following the solid line shown in Figure 4b is designed to validate its effects on passive source RTM. We note here, the model will be stretched in depth direction within the SPECFEM package to handle the topographic changes. 161 stations with a horizontal station spacing of 1.0 km are distributed on the surface of the model. We use a Ricker source wavelet with a peak frequency of 1.0 Hz to initialize the incident plane waves. 12 P-wave plane waves, with incident angles ranging from 12°-27°, are injected into the local simulation domain to simulate the teleseismic waves. The back-azimuthal angles for events 1, 3, 7, 9 and 11 are 90° and 270° for the rest events. This makes a symmetric coverage of plane waves propagating through the model. The corresponding teleseismic data are recorded by the station for each event. Seismograms for the first teleseismic event with an incident angle of 27° and the back-azimuthal angle of 90° are shown in Figure 3. By using the short-time average over long-time average (STA/LTA) algorithm (Withers et al., 1998), it is feasible to detect the onset of the incident wavefield. The magenta lines in Figure 3 denote the time windows used in our imaging, which are 5 seconds before and 6 seconds after the onset of the incident P waves. It helps us to isolate multiple refections that may distort our imaging results. We speculate that the onset of incident P waves in both Z and X components shows the imprint of the topographic changes. Without considering the topographic changes, i.e., injecting teleseismic data at 0 km elevation of each station, a significant imprint of topography can be observed in the imaging result in Figure 4a, which looks like a mirror of the topography. On the contrary, the reflector can be accurately imaged by injecting the teleseismic data at the right locations by considering the topographic changes (Figure 4b).

3.2 Synthetic test 2: imaging subduction slabs

In this synthetic test, we validate the capability of our method to image complex structures in subduction zones. The background model is a two-layer crust and mantle structure, with density, Vp and Vs, the same as the previous example. A 3-D subducting slab (Figure 6a-b) is designed between -60 to 60 km along the X (Longitude) direction, -30 to 30 km along the Y (Latitude) direction and 40 to 140 km in depth with a thickness of 50 km. The Moho depth is 35 km. The model parameters (density, Vp and Vs) of the subducting slab are 12% greater than the background model. Our simulation domain spans from -120 to 120 km along the X direction, -48 to 48 km along the Y direction and 0 to 160 km along the depth direction. We use 201 stations with 1.0 km station spacing evenly distributed from -100.0 km to 100.0 km. 12 teleseismic P wave events with the same back-azimuth and incident angles as the previous example are injected into the local study region, starting from an initial depth at 240 km. The rest parameters are the same as the previous synthetic test. Synthetic Z and X component seismograms for the first teleseismic event are illustrated in Figures 5a and b. Because the back-azimuth angle of this event is 90°, the X components are equal to the radial components, which could be used to investigate Ps-converted waves. Due to the complexity of the velocity model, we speculate several kinds of multiple reflections (Moho and slab-related) for the P waves in Z components. The corresponding Ps-converted waves can be investigated from X components in Figure 5b. Interestingly, despite being weaker than Moho-related converted waves (S), slab-related as well as multiple reflection-related S-converted waves can also be seen.

Our RTM is implemented using a smoothed two-layer background model (Figures 6 c-d) to avoid artifacts arising from sharp velocity interfaces during the wavefield separation (J. Yang et al., 2018). It is smoothed vertically using a Gaussian function with a radius of 5.0 km. This means we do not include the slab in our migration velocity model, which is close to the real cases. After stacking and illuminating, the interfaces of the slab are well imaged as displayed in Figure 6g. It suggests that our method is capable of imaging complex structures, such as velocity anomalies with high dipping angles. Because it is quite difficult to isolate multiple reflections in this case, we also see different-order multiple imaging artifacts in our stacked result. We also show the imaging result from the first four teleseismic events, which also successfully captures the main features of the slab and the Moho, but with stronger artifacts due to not enough stacking. In addition, the images along the Y (Latitude) direction (Figures 6f and h), which is perpendicular to our stations' distribution, indicate that with only several effective stations, the migration will map the converted waveforms along the isochrone interfaces in depths (Schneider, 1978). Because we only use one linear array across the slab, it is necessary to consider the contributions of teleseismic events with back-azimuthal angles away from the array direction. We test another three back-azimuthal angle pairs, which are 0°/180°, 45°/225° and 135°/315° with the same incident angle as the previous test. Figure 7 shows the migration results from the back-azimuthal angle pairs of 0°/180° and 45°/225°. The migration result from 135°/315° azimuthal-angle pair is similar to the one from 45°/225°. As expected, when the azimuthal angles are away from the linear array direction, the interfaces of the imaged slab and the Moho become weaker and more incoherent artifacts become stronger. Interestingly, the Moho interface disappears when using teleseismic events with the 0°/180 ° azimuthal pair. This could be explained by the concept of the Fresnel zone. Bostock (1998) pointed out that the Fresnel zone of the scattering points depends on the dominant frequencies and depths of the interface. Assuming that constructive interference arises for phase differences less than a quarter period, the diameter of the Fresnel zone around the interface varies between ∼25 km for P_mS (Moho converted wave) at 0.5 Hz to ∼160 km for $P_{660}S$ (generated at the 660 km discontinuity) at 0.25 Hz. This means the converted waves recorded at stations that arise from deeper interfaces (e.g., X=0, Y=0 and Z=660 km) could be the response to a larger range of interfaces, e.g., X=[-80, 80], Y=[-80, 80], Z=[580, 740] km. We note here, the estimations of X and Y ranges are fairly rough. For teleseismic events with back-azimuthal angles away from the linear array, their Fresnel zone is also away from the structures beneath the linear array. As a consequence of small Fresnel zones, shallow interfaces, such as the Moho, gradually disappear beneath the linear array due to incoherence stacking from different events. Therefore, reasonable good station, incident angle and azimuthal angle coverages are preferred for our method if we intend to image the interfaces beneath a linear array (Shang et al., 2012; Li et al., 2018).

3.3 Imaging the Cheyenne Belt suture zone (CBSZ) using the Laramie array

3.3.1 Geological setting

The CBSZ is a tectonic suture zone between the Archean Wyoming craton to the north and the Paleoproterozoic Yavapai province to the south (Karlstrom & Houston, 1984; Sims & Stein, 2003; Hansen & Dueker, 2009; Jones et al., 2010). It contains a set of steeply south-dipping shear zones formed during the 1.78–1.75 Ga Medicine Bow orogeny when the Proterozoic Green Mountain arc collided with the passive margin of the Wyoming craton via south-facing subduction (Tyson et al., 2002; Hansen & Dueker, 2009). Steep stretching lineations and shear-sense features indicate south-side-up motion (Tyson et al., 2002; Hansen & Dueker, 2009). To better constrain the structure of the CBSZ, the Laramie array was deployed within the Laramie basin across the inferred trace of the Cheyenne belt (Figure 8) (Hansen & Dueker, 2009). It is a dense 80 km long linear array with broadband seismometers, which consists of 30 sensors spaced 2.2 km apart and was deployed for a period of eight months in 2000–2001. Based on P and S receiver functions together with teleseismic P wave traveltime tomography, Hansen and Dueker (2009) found an imbricated Moho north of the Cheyenne belt. It is basically consistent with the interpretation of seismic results from the CDROM (Continental Dynamics Rocky Mountain) project (Tyson et al., 2002). However, either due to the limited aperture of the Laramie array, or the methodologies, the CBSZ hasn't been clearly imaged as shown in Figure 7 of Hansen and Dueker (2009). Ruigrok et al. (2010) used seismic interferometry to extract reflection responses from the coda of the transmitted energy from distant earthquakes, where they found discontinuities in their migration images, which were interpreted as the CBSZ. Here, we use our passive source RTM method to further investigate the detailed shape of the CBSZ with converted teleseismic P and S waves.

3.3.2 Data

The teleseismic P wave dataset is constructed from 11 events at 30°–90° distance with body-wave magnitudes greater than 5.5. The S wave dataset is selected from 1 S-wave and 7 SKS events from 55°–85° and 85°-120° epicentral distances, respectively (Wilson & Aster, 2005; Yuan et al., 2006). Detailed information about these events can be found in Table 1 and displayed in Figure 9. The data is selected, downloaded and preprocessed with the standing order for data package (SOD) (Owens et al., 2004). For each P wave event, three-component waveforms within the time window of two minutes before and three minutes after direct P arrivals predicted by the AK135 model (Kennett et al., 1995) are collected. The north-south and west-east component seismograms are rotated to radial and transverse components after removing instrument response, linear trend, and mean values, followed by a bandpass filter of 1-20 s. Then, the preprocessed three-component waveforms of each event are visually inspected, and only those with a signal-to-noise ratio (SNR) larger than 3.0 and 2.0 for vertical and radial components are kept. Afterward, we use the open-source software AIMBAT (Lou et al., 2013) to remove bad seismograms with spurious amplitudes and cross-correlation coefficients lower than 0.80 for vertical and radial components. To avoid spatial aliasing, only events with more than 15 seismograms are remained. The data selection process for S and SKS events is similar except: (1) the time window is defined as two minutes before and three minutes after incident S arrivals; (2) seismograms with SNR larger than 2.0 and 3.0 for vertical and radial components are kept. This is because S waves are mainly in radial components. In the end, most events have more than 25 high-quality seismograms for each component.

Gray (2013) and Li et al. (2018) suggested that station spacing is an important factor for spatial aliasing during passive source RTM. For example, 5 km station spacing will result in slightly aliased P-wave migration with 1 Hz data, given the incident angles range from 12 ° to 27°. Therefore, we interpolate those deleted bad seismograms using 2-D cubic-spline interpolation (J. Zhang & Zheng, 2015). The 2-D cubic-spline interpolation was originally used to refine the receiver functions from sparse station distributions. Here, we use it to interpolate the aligned vertical and radial component seismograms. It mainly includes three steps: (1) align the seismograms according to the onset of incident waves (P or S), predicted by the reference model, such as AK135 (Kennett et al., 1995). The reference time could be further adjusted by applying a multichannel cross-correlation algorithm (VanDecar & Crosson, 1990); (2) perform 2-D interpolation for each time step using the cubic-spline method for each component; (3) shift the interpolated data back according to the reference time. We note here, the absolute amplitudes are kept during interpolation for each channel and component, which is different from J. Zhang and Zheng (2015). This is important for dealing with multi-component data. As compared in Figure 9, the interpolated seismograms follow the same trend of nearby stations in great details for both P and S waves. We use 10 s before and 30 s after the onset of P and 30 s before and 30 s after the onset of S waves for the following migration.

3.3.3 Migration

Our computational domain for wavefield propagation spans from -106.25° to -105.30° along longitude, 40.85° to 41.75° along latitude, and -10 to 110 km in the depth direction. We use 48, 60 and 80 elements along these three directions, yielding an average element size of 1.5 km. Given the minimal Vp of 5.05 km/s from our migration model and about two elements for each P wavelength, it allows us to use periods greater than 0.65 s for accurate wave simulation. A 7.5 km (about 3 elements) perfect-matched layer (PML) absorbing boundary condition is applied to each surface of the simulation domain to avoid artificial reflections from the boundaries (Komatitsch & Tromp, 2003). As outlined in section 2.3, source time functions are estimated from the aligned vertical component of each P wave event (radial for S wave), followed by an iterative time deconvolution (Kikuchi & Kanamori, 1982) to remove the source time function effect (Bostock, 1998; Rondenay et al., 2000; Bostock et al., 2001; Bostock, 2002; Shang et al., 2017). Given an average station spacing about 2-3 km, the deconvolved event data are bandpass filtered at 1-20 s as the adjoint sources for finite frequency wavefield modeling. The migration velocity model is extracted from a 3-D regional model US2016 (Shen & Ritzwoller, 2016). We smooth it using a Gaussian function with a radius of 5.0 km both vertically and horizontally. Then, the migration is implemented for each event and summed up to get the final stacked image. In this study, we perform the migration for P and S waves separately.

3.3.4 Results

Due to the finite frequency property, we identify velocity increase as positive migration phases flanked by negative ones as indicated by synthetic tests (Figures 4 and 6). The basement-sediment contact beneath the Laramie basin is identified in the P-wave image as the positive high amplitude phases beneath the negative phases around 2-7 km (Figure 10a), which becomes slightly deeper (dip to the northwest) between 30-40 km in the horizon, right beneath the Laramie basin. Whereas this feature is not clear from the S wave image shown in Figure 10b, possibly due to the back azimuthal angles of most S events being basically perpendicular to the array direction (Figure 9d). The most prominent features in both P and S wave images are the bunches of south-dipping positive/negative phases between -40 and 10 km in lateral direction and 0 and 70 km in depths. They are interpreted as the CBSZ, which situated juxtaposition of accreted Proterozoic terranes with the Archean Wyoming craton (Hansen & Dueker, 2009; Tyson et al., 2002). The northward crustal thickening seems to be indicated by the Proterozoic Moho, highlighted by dark green dots in the P wave image (Figure 10a). However, due to spatial aliasing in both P and S wave images between 20 and 40 km horizontally, the Archean Moho is not well constrained (Hansen & Dueker, 2009). Therefore, we try to suppress the spatial aliasing effect by refining the stations for every 1.0 km as illustrated in Figure 11. The comparison of the interpolated seismograms shows a good match both in trends and amplitudes of different events. We conduct P wave migration again using the refined data. As shown in Figure 11c, most spatial aliasing artifacts are suppressed and both the Archean Moho ($\sim$45 km) and the Proterozoic Moho ($\sim$60 km) can be clearly identified. They are slightly dipping northward to the north of the CBSZ. These are consistent with previous studies (Allmendinger et al., 1982; Prodehl et al., 1989; Snelson et al., 1998; Morozova et al., 2002). However, our Proterozoic Moho seems to be distorted with the CBSZ around 15 km in the horizontal direction (south of the CBSZ), whereas Hansen and Dueker (2009) found it to be continuous beneath the entire array. Nevertheless, we interpreted the CBSZ as the orange shadow zones in Figure 11c. Further investigation for a detailed migration velocity model will be helpful for better imaging and interpretation.

4 Discussions

We combine full wavefield passive source RTM with the spectral element method so that it is convenient to handle topographic changes and velocity heterogeneities. Both synthetic and suture zone imaging examples demonstrate the performance of our method.

4.1 2-D data interpolation

Migration antialiasing due to spatial frequency components (station spacing) is a longstanding problem in seismic imaging, for example, 5-D data interpolation (Trad, 2009) has been developed to improve the imaging quality. Therefore, it is important to consider the effects of station spacing for passive RTM (L. Chen et al., 2005; Li et al., 2018). The Nyquist-Shannon sampling theorem suggests that the station spacing is required to be smaller than the apparent half-wavelength to fully construct the wavefield from recorded seismograms at the surface (Gray, 2013; Li et al., 2018). Therefore, given constant crustal P and S wave velocities of 5.8 and 3.2 km/s, respectively, and incident angles of 12° to 27°, full construction of 1.0 Hz P waves at near-surface requires a station spacing ranging from 6.4 to 14.5 km, but 3.5 to 8.0 km for 1.0 Hz S waves. This gives us an upper bound limit for the station spacing. Smaller station spacing is expected because the incident angle for converted Ps waves could be larger, especially when the subsurface structures are complex, like subduction and suture zones. For example, given a high-frequency cut about 2.5 Hz, a 2.0 km station spacing would result in slight spatial aliasing as shown in Figure 12a compared to the result obtained with a 1.0 km station spacing shown in Figure 6g. As expected, a 4.0 km station spacing would result in even stronger spatial aliasing as shown in Figure 12b. Depending on the specific imaging target, 2-D data interpolation might be necessary for migration. However, most data interpolation (regularization) strategies developed for seismic exploration, like FX domain trace interpolation (Spitz, 1991), antileakage Fourier transformation (Xu et al., 2005) or curvelet transformation (Herrmann & Hennenfent, 2008; Shang et al., 2017) require linearity of station distributions, which is not straightforward to handle 2-D irregularly-spaced (3-D if we consider the station elevations) data. Therefore, we prefer to use the 2-D cubic-spline interpolation (J. Zhang & Zheng, 2015) or the radial function-based method (Shepard, n.d.), which can naturally handle irregularly-spaced data for our migration. We note here that, unlike its first application for interpolating 2-D receiver functions (J. Zhang & Zheng, 2015), we need to align the multi-channel data prior to interpolation for each component, and then shift the interpolated data back according to the onsets of incident waves for migration.

4.2 Source time function estimations

It is straightforward to estimate the source time functions for P waves, which has been successfully used for teleseismic full waveform inversion (Y. Wang et al., 2016; K. Wang et al., 2021). However, the estimation of source time functions for S waves should be carefully considered, because of relatively larger incident angles compared to P waves. This results in the leakage of S waves into vertical and transverse components. Therefore, rotation of vertical, radial and transverse components into P, SV and SH polarization directions could be helpful for source time function estimations for S waves (Bostock, 1998; Rondenay, 2009).

4.3 Migration velocity models

One advantage of our methodology is that we are able to implement migration based on 3-D velocity models with strong heterogeneities. The accuracy of migration velocity models is essential for mapping seismograms to correct locations and avoiding stacking artifacts (Mora, 1989; He & Liu, 2020). To illustrate the advantages of using more accurate migration velocity models for imaging, we conduct another migration for slab imaging, which is shown in Figure 13. The migration velocity model is obtained by smoothing the true velocity model using a Gaussian function with a radius of 5.0 km both horizontally and vertically. We speculate that, with a more reasonable migration velocity model, the vertical boundaries (see true model in Figure 6a) on the left and right sides of the slab are better constrained compared to those shown in Figure 6g. However, for our suture zone imaging, a smoothed regional 3-D model is not accurate enough because the grid spacing ($\sim$25 km) of model US2016 (Shen & Ritzwoller, 2016) is too large to capture velocity heterogeneities in such a small study region. Therefore, teleseismic body wave traveltime tomography (D. Zhao et al., 1992; Tong, 2021) or ambient noise tomography (C. Zhang et al., 2018) could be used to construct a more reasonable migration velocity model for our imaging in the future.

5 Conclusion

In this study, we propose to solve weak-form solutions to decompose elastic wavefields into vector P and S waves for teleseismic reverse time migration based on the spectral element method. Both synthetic tests and Cheyenne Belt suture zone imaging demonstrate the capability of our method to image complex structures with strong velocity heterogeneity. For linear array migration, our synthetic tests show that teleseismic events with back azimuthal angles parallel to the linear array direction contribute more to subsurface migration images than those away from the linear array direction. However, the latter could still contribute to the image beneath the array thanks to larger Fresnel zone contributions at greater depths. In addition, we reveal several south-dipping structures in the Laramie basin, which are interpreted as the Cheyenne Belt suture zone, and are consistent with geological interpretations from previous studies. For better performance of the migration-based imaging method, 2-D/3-D data interpolation is required to avoid spatial aliasing during the construction of wavefields in the subsurface.

Open Research

The Laramie array seismic data used in this study can be obtained from the IRIS Data Management Center (`https://ds.iris.edu/ds`) under the network codes XF. We use SPECFEM3-D Cartesian 4.0.0 (Komatitsch et al., 1999; Komatitsch & Tromp, 2002b, 2002a) published under the GPL 3 license for synthetic and real data simulations. PyGMT (Wessel et al., 2019) download from (`https://www.pygmt.org/latest/`) is used to plot figures.

Acknowledgments

This paper is contribution no. *** from the Department of Geosciences at the University of Texas at Dallas. The numerical results are computed through the Optane nodes on the UTD Seismology Group HPC clusters. This research is partially supported by the sponsors of the UT Dallas 3D + 4D Seismic Full Waveform Inversion research consortium.

Author Contributions

The authors confirm their contribution to the paper as follows: study conception and design: Hejun Zhu; Weak-form solutions were first proposed by Yu Chen, then theoretically derivated and tested by Bin He. Data collection: Bin He; Analysis and interpretation of results: Bin He, Hejun Zhu, David Lumley, Qinya Liu, Hitoshi Kawakatsu and Nozomu Takeuch; Draft manuscript preparation: Bin He, Hejun Zhu. All authors review the results and approve the final version of the manuscript.

References

Ai, Y., Chen, Q.-f., Zeng, F., Hong, X., & Ye, W. (2007). The crust and upper mantle structure beneath southeastern China. *Earth and Planetary Science Letters*, *260*(3-4), 549–563.

Allmendinger, R., Brewer, J., Brown, L., Kaufman, S., Oliver, J., & Houston, R. (1982). COCORP profiling across the Rocky Mountain Front in southern Wyoming, Part 2: Precambrian basement structure and its influence on Laramide deformation. *Geological Society of America Bulletin*, *93*(12), 1253–1263.

Andrade, P. N., Pestana, R. C., & dos Santos, A. W. (n.d.). Kirchhoff depth migration using maximum amplitude traveltimes computed by the Chebyshev polynomial recursion. In *14th International Congress of the Brazilian Geophysical Society & EXPOGEF, Rio de Janeiro, Brazil, 3-6 August 2015, pages=1109–1113, year=2015, organization=Brazilian Geophysical Society.*

Audebert, F., Nichols, D., Rekdal, T., Biondi, B., Lumley, D. E., & Urdaneta, H. (1997). Imaging complex geologic structure with single-arrival Kirchhoff prestack depth migration. *Geophysics*, *62*(5), 1533–1543.

Banerdt, W. B., Smrekar, S. E., Banfield, D., Giardini, D., Golombek, M., Johnson, C. L., ... others (2020). Initial results from the InSight mission on Mars. *Nature Geoscience*, *13*(3), 183–189.

Baysal, E., Kosloff, D. D., & Sherwood, J. W. (1983). Reverse time migration. *Geophysics*, *48*(11), 1514–1524.

Bevc, D. (1997). Flooding the topography: Wave-equation datuming of land data with rugged acquisition topography. *Geophysics*, *62*(5), 1558–1569.

Bostock, M. (1998). Mantle stratigraphy and evolution of the Slave province. *Jour-*

nal of Geophysical Research: Solid Earth, *103*(B9), 21183–21200.

Bostock, M. (2002). Kirchhoff-approximate inversion of teleseismic wavefields. *Geophysical Journal International*, *149*(3), 787–795.

Bostock, M., & Rondenay, S. (1999). Migration of scattered teleseismic body waves. *Geophysical journal international*, *137*(3), 732–746.

Bostock, M., Rondenay, S., & Shragge, J. (2001). Multiparameter two-dimensional inversion of scattered teleseismic body waves 1. Theory for oblique incidence. *Journal of Geophysical Research: Solid Earth*, *106*(B12), 30771–30782.

Burdick, L. J., & Langston, C. A. (1977). Modeling crustal structure through the use of converted phases in teleseismic body-wave forms. *Bulletin of the Seismological Society of America*, *67*(3), 677–691.

Burridge, R., de Hoop, M. V., Miller, D., & Spencer, C. (1998). Multiparameter inversion in anisotropic elastic media. *Geophysical Journal International*, *134*(3), 757–777.

Chen, L., Wen, L., & Zheng, T. (2005). A wave equation migration method for receiver function imaging: 1. Theory. *Journal of Geophysical Research: Solid Earth*, *110*(B11).

Chen, X., Li, Y., & Levin, V. (2018). Shear wave splitting beneath eastern North American continent: evidence for a multilayered and laterally variable anisotropic structure. *Geochemistry, Geophysics, Geosystems*, *19*(8), 2857–2871.

Cheng, C., Bodin, T., & Allen, R. M. (2016). Three-dimensional pre-stack depth migration of receiver functions with the fast marching method: a Kirchhoff approach. *Geophysical Journal International*, *205*(2), 819–829.

Claerbout, J. F. (1985). *Imaging the earth's interior* (Vol. 1). Blackwell Scientific Publications Oxford.

Clayton, R., Persaud, P., Denolle, M., & Polet, J. (2019). Exposing Los Angeles's shaky geologic underbelly, Eos, 100. *EOS. https://doi. org/10.1029*.

Crotwell, H. P., Owens, T. J., Ritsema, J., et al. (1999). The TauP Toolkit: Flexible seismic travel-time and ray-path utilities. *Seismological Research Letters*, *70*, 154–160.

Duan, C., Lumley, D., & Zhu, H. (2021). Estimation of micro-earthquake source locations based on full adjoint P and S wavefield imaging. *Geophysical Journal*

International, *226*(3), 2116–2144.

Dueker, K. G., & Sheehan, A. F. (1997). Mantle discontinuity structure from midpoint stacks of converted P to S waves across the Yellowstone hotspot track. *Journal of Geophysical Research: Solid Earth*, *102*(B4), 8313–8327.

Fichtner, A. (2010). *Full seismic waveform modelling and inversion.* Springer Science & Business Media.

Fichtner, A., Kennett, B. L., Igel, H., & Bunge, H.-P. (2009). Full seismic waveform tomography for upper-mantle structure in the Australasian region using adjoint methods. *Geophysical Journal International*, *179*(3), 1703–1725.

Gilbert, H. J., Sheehan, A. F., Dueker, K. G., & Molnar, P. (2003). Receiver functions in the western United States, with implications for upper mantle structure and dynamics. *Journal of Geophysical Research: Solid Earth*, *108*(B5).

Gray, S. H. (2013). Spatial sampling, migration aliasing, and migrated amplitudes. *Geophysics*, *78*(3), S157–S164.

Gray, S. H., & May, W. P. (1994). Kirchhoff migration using eikonal equation traveltimes. *Geophysics*, *59*(5), 810–817.

Hansen, S., & Dueker, K. (2009). P-and S-wave receiver function images of crustal imbrication beneath the Cheyenne Belt in southeast Wyoming. *Bulletin of the Seismological Society of America*, *99*(3), 1953–1961.

He, B., & Liu, Y. (2020). Wave-equation migration velocity analysis using Radon-domain common-image gathers. *Journal of Geophysical Research: Solid Earth*, *125*(2), e2019JB018938.

Herrmann, F. J., & Hennenfent, G. (2008). Non-parametric seismic data recovery with curvelet frames. *Geophysical Journal International*, *173*(1), 233–248.

Hill, N. R. (1990). Gaussian beam migration. *Geophysics*, *55*(11), 1416–1428.

Hill, N. R. (2001). Prestack Gaussian-beam depth migration. *Geophysics*, *66*(4), 1240–1250.

Jin, H., & Etgen, J. (n.d.). Evaluating Kirchhoff migration using wave-equation generated maximum amplitude traveltimes. In *SEG Technical Program Expanded Abstracts 2020, pages=2968–2972, year=2020, publisher=Society of Exploration Geophysicists.*

Jones, D. S., Snoke, A. W., Premo, W. R., & Chamberlain, K. R. (2010). New models for Paleoproterozoic orogenesis in the Cheyenne belt region: Evidence from the geology and U-Pb geochronology of the Big Creek Gneiss, southeastern Wyoming. *Bulletin*, *122*(11-12), 1877–1898.

Karlstrom, K., & Houston, R. (1984). The Cheyenne belt: Analysis of a Proterozoic suture in southern Wyoming. *Precambrian research*, *25*(4), 415–446.

Kawakatsu, H., & Watada, S. (2007). Seismic evidence for deep-water transportation in the mantle. *Science*, *316*(5830), 1468–1471.

Kennett, B. L., Engdahl, E., & Buland, R. (1995). Constraints on seismic velocities in the Earth from traveltimes. *Geophysical Journal International*, *122*(1), 108–124.

Kikuchi, M., & Kanamori, H. (1982). Inversion of complex body waves. *Bulletin of the Seismological Society of America*, *72*(2), 491–506.

Kind, R., Yuan, X., & Kumar, P. (2012). Seismic receiver functions and the lithosphere-asthenosphere boundary. *Tectonophysics*, *536*, 25–43.

Knapmeyer-Endrun, B., Bissig, F., Compaire, N., Garcia, R., Joshi, R., Khan, A., ... others (2020). First seismic constraints on the Martian crust-receiver functions for InSight.

Komatitsch, D., & Tromp, J. (2002a). Spectral-element simulations of global seismic wave propagation—II. Three-dimensional models, oceans, rotation and self-gravitation. *Geophysical Journal International*, *150*(1), 303–318.

Komatitsch, D., & Tromp, J. (2002b). Spectral-element simulations of global seismic wave propagation—I. Validation. *Geophysical Journal International*, *149*(2), 390–412.

Komatitsch, D., & Tromp, J. (2003). A perfectly matched layer absorbing boundary condition for the second-order seismic wave equation. *Geophysical Journal International*, *154*(1), 146–153.

Komatitsch, D., & Vilotte, J.-P. (1998). The spectral element method: an efficient tool to simulate the seismic response of 2D and 3D geological structures. *Bulletin of the seismological society of America*, *88*(2), 368–392.

Komatitsch, D., Vilotte, J.-P., Vai, R., Castillo-Covarrubias, J. M., & Sánchez-Sesma, F. J. (1999). The spectral element method for elastic wave equations—application to 2-D and 3-D seismic problems. *International Journal for numerical methods in engineering*, *45*(9), 1139–1164.

Langston, C., & Corvallis, O. (1977). crustal and upper mantle receiver structure from teleseismic P-waves and S-waves. *Bull. Seismol. Soc. Am*, *67*, 713–724.

Levander, A., Niu, F., Symes, W. W., & Nolet, G. (2005). Imaging teleseismic P to S scattered waves using the Kirchhoff integral. *GEOPHYSICAL MONOGRAPH-AMERICAN GEOPHYSICAL UNION*, *157*, 149.

Li, J., Shen, Y., & Zhang, W. (2018). Three-dimensional passive-source reverse-time migration of converted waves: The method. *Journal of Geophysical Research: Solid Earth*, *123*(2), 1419–1434.

Line-source simulation for shallow-seismic data. Part 1: Theoretical background, author=Forbriger, Thomas and Groos, Lisa and Schäfer, Martin. (2014). *Geophysical Journal International*, *198*(3), 1387–1404.

Liu, K., & Levander, A. (2013). Three-dimensional Kirchhoff-approximate generalized Radon transform imaging using teleseismic P-to-S scattered waves. *Geophysical Journal International*, *192*(3), 1196–1216.

Lognonné, P., Banerdt, W. B., Pike, W., Giardini, D., Christensen, U., Garcia, R. F., ... others (2020). Constraints on the shallow elastic and anelastic structure of Mars from InSight seismic data. *Nature Geoscience*, *13*(3), 213–220.

Long, M. D., Benoit, M. H., Aragon, J. C., & King, S. D. (2019). Seismic imaging of mid-crustal structure beneath central and eastern North America: Possibly the elusive Grenville deformation? *Geology*, *47*(4), 371–374.

Lou, X., Van Der Lee, S., & Lloyd, S. (2013). AIMBAT: A python/matplotlib tool for measuring teleseismic arrival times. *Seismological Research Letters*, *84*(1), 85–93.

Maguire, R., Schmandt, B., Li, J., Jiang, C., Li, G., Wilgus, J., & Chen, M. (2022). Magma accumulation at depths of prior rhyolite storage beneath Yellowstone Caldera. *Science*, *378*(6623), 1001–1004.

Mahrer, K. D. (1990). Numerical time step instability and Stacey's and Clayton-Engquist's absorbing boundary conditions. *Bulletin of the Seismological Society of America*, *80*(1), 213–217.

McMechan, G. A. (1982). Determination of source parameters by wavefield extrapolation. *Geophysical Journal International*, *71*(3), 613–628.

McMechan, G. A. (1983). Migration by extrapolation of time-dependent boundary values. *Geophysical prospecting*, *31*(3), 413–420.

Meltzer, A., Rudnick, R., Zeitler, P., Levander, A., Humphreys, G., Karlstrom, K.,

... others (1999). The USArray initiative. *Geological Society of America Today*, *9*, 8–10.

Millet, F., Bodin, T., & Rondenay, S. (2019). Multimode 3-D Kirchhoff migration of receiver functions at continental scale. *Journal of Geophysical Research: Solid Earth*, *124*(8), 8953–8980.

Mora, P. (1989). Inversion= migration+ tomography. *Geophysics*, *54*(12), 1575–1586.

Morozova, E., Wan, X., Chamberlain, K. R., Smithson, S. B., Morozov, I. B., Boyd, N. K., ... Foster, C. (2002). Geometry of Proterozoic sutures in the central Rocky Mountains from seismic reflection data: Cheyenne belt and Farwell Mountain structures. *Geophysical Research Letters*, *29*(13), 17–1.

Nábělek, J., Hetényi, G., Vergne, J., Sapkota, S., Kafle, B., Jiang, M., ... Team, t. H.-C. (2009). Underplating in the Himalaya-Tibet collision zone revealed by the Hi-CLIMB experiment. *Science*, *325*(5946), 1371–1374.

Nakata, N., & Beroza, G. C. (2016). Reverse time migration for microseismic sources using the geometric mean as an imaging condition. *Geophysics*, *81*(2), KS51–KS60.

Notfors, C., Xie, Y., & Gray, S. (n.d.). Gaussian Beam Migration-A Viable Alternative to Kirchhoff? In *68th EAGE Conference and Exhibition incorporating SPE EUROPEC 2006, pages=cp–2, year=2006, organization=EAGE Publications BV.*

Okada, Y., Kasahara, K., Hori, S., Obara, K., Sekiguchi, S., Fujiwara, H., & Yamamoto, A. (2004). Recent progress of seismic observation networks in Japan—Hi-net, F-net, K-NET and KiK-net. *Earth, Planets and Space*, *56*(8), xv–xxviii.

Onyango, E. A., Worthington, L. L., Schmandt, B., & Abers, G. A. (2022). Subduction Zone Interface Structure within the Southern MW9. 2 1964 Great Alaska Earthquake Asperity: Constraints from Receiver Functions Across a Spatially Dense Node Array. *Geophysical Research Letters*, *49*(15), e2022GL098334.

Owens, T. J., Crotwell, H. P., Groves, C., & Oliver-Paul, P. (2004). SOD: Standing order for data. *Seismological Research Letters*, *75*(4), 515–520.

Prodehl, C., Lipman, P. W., Pakiser, L., & Mooney, W. (1989). Crustal structure of the Rocky Mountain region. *Geophysical framework of the continental United*

States, *172*, 249–284.

Rajasekaran, S., & McMechan, G. A. (1995). Prestack processing of land data with complex topography. *Geophysics*, *60*(6), 1875–1886.

Richards, P. G., & Aki, K. (1980). *Quantitative seismology: theory and methods* (Vol. 859). Freeman San Francisco, CA.

Rondenay, S. (2009). Upper mantle imaging with array recordings of converted and scattered teleseismic waves. *Surveys in geophysics*, *30*, 377–405.

Rondenay, S., Bostock, M. G., Hearn, T. M., White, D. J., & Ellis, R. M. (2000). Lithospheric assembly and modification of the SE Canadian Shield: Abitibi-Grenville teleseismic experiment. *Journal of Geophysical Research: Solid Earth*, *105*(B6), 13735–13754.

Ruigrok, E., Campman, X., Draganov, D., & Wapenaar, K. (2010). High-resolution lithospheric imaging with seismic interferometry. *Geophysical Journal International*, *183*(1), 339–357.

Schäfer, M., Groos, L., Forbriger, T., & Bohlen, T. (2014). Line-source simulation for shallow-seismic data. Part 2: Full-waveform inversion—A synthetic 2-D case study. *Geophysical Journal International*, *198*(3), 1405–1418.

Schneider, W. A. (1978). Integral formulation for migration in two and three dimensions. *Geophysics*, *43*(1), 49–76.

Shang, X., de Hoop, M. V., & van der Hilst, R. D. (2012). Beyond receiver functions: Passive source reverse time migration and inverse scattering of converted waves. *Geophysical Research Letters*, *39*(15).

Shang, X., de Hoop, M. V., & van der Hilst, R. D. (2017). Common conversion point stacking of receiver functions versus passive-source reverse time migration and wavefield regularization. *Geophysical Journal International*, *209*(2), 923–934.

Sheehan, A. F., Shearer, P. M., Gilbert, H. J., & Dueker, K. G. (2000). Seismic migration processing of P-SV converted phases for mantle discontinuity structure beneath the Snake River Plain, western United States. *Journal of Geophysical Research: Solid Earth*, *105*(B8), 19055–19065.

Shen, W., & Ritzwoller, M. H. (2016). Crustal and uppermost mantle structure beneath the United States. *Journal of Geophysical Research: Solid Earth*, *121*(6), 4306–4342.

Shepard, D. (n.d.). A two-dimensional interpolation function for irregularly-spaced data. In *Proceedings of the 1968 23rd ACM national conference, pages=517–524, year=1968.*

Shragge, J. (2014). Reverse time migration from topography. *Geophysics*, *79*(4), S141–S152.

Sims, P. K., & Stein, H. J. (2003). Tectonic evolution of the Proterozoic Colorado province, Southern Rocky Mountains: A summary and appraisal. *Rocky Mountain Geology*, *38*(2), 183–204.

Snelson, C. M., Henstock, T. J., Keller, G. R., Miller, K. C., & Levander, A. (1998). Crustal and uppermost mantle structure along the Deep Probe seismic profile. *Rocky Mountain Geology*, *33*(2), 181–198.

Spitz, S. (1991). Seismic trace interpolation in the FX domain. *Geophysics*, *56*(6), 785–794.

Sun, R., McMechan, G. A., Hsiao, H.-H., & Chow, J. (2004). Separating P-and S-waves in prestack 3D elastic seismograms using divergence and curl. *Geophysics*, *69*(1), 286–297.

Tape, C., Liu, Q., Maggi, A., & Tromp, J. (2009). Adjoint tomography of the southern California crust. *Science*, *325*(5943), 988–992.

Tong, P. (2021). Adjoint-state traveltime tomography: Eikonal equation-based methods and application to the Anza Area in Southern California. *Journal of Geophysical Research: Solid Earth*, *126*(5), e2021JB021818.

Tong, P., Chen, C.-w., Komatitsch, D., Basini, P., & Liu, Q. (2014). High-resolution seismic array imaging based on an SEM-FK hybrid method. *Geophysical Journal International*, *197*(1), 369–395.

Tong, P., Komatitsch, D., Tseng, T.-L., Hung, S.-H., Chen, C.-W., Basini, P., & Liu, Q. (2014). A 3-D spectral-element and frequency-wave number hybrid method for high-resolution seismic array imaging. *Geophysical Research Letters*, *41*(20), 7025–7034.

Trad, D. (2009). Five-dimensional interpolation: Recovering from acquisition constraints. *Geophysics*, *74*(6), V123–V132.

Tromp, J. (2020). Seismic wavefield imaging of Earth's interior across scales. *Nature Reviews Earth & Environment*, *1*(1), 40–53.

Tromp, J., Tape, C., & Liu, Q. (2005). Seismic tomography, adjoint methods, time reversal and banana-doughnut kernels. *Geophysical Journal International*, *160*(1), 195–216.

Tyson, A. R., Morozova, E., Karlstrom, K., Dueker, K. C. S. S. K., & Foster, C. (2002). Proterozoic Farwell Mountain–Lester Mountain suture zone, northern Colorado: Subduction flip and progressive assembly of arcs. *Geology*, *30*(10), 943–946.

VanDecar, J., & Crosson, R. (1990). Determination of teleseismic relative phase arrival times using multi-channel cross-correlation and least squares. *Bulletin of the Seismological Society of America*, *80*(1), 150–169.

Vinnik, L. (1977). Detection of waves converted from P to SV in the mantle. *Physics of the Earth and planetary interiors*, *15*(1), 39–45.

Waheed, U. B., Yarman, C. E., & Flagg, G. (2015). An iterative, fast-sweeping-based eikonal solver for 3D tilted anisotropic media. *Geophysics*, *80*(3), C49–C58.

Wang, K., Jiang, C., Yang, Y., Schulte-Pelkum, V., & Liu, Q. (2020). Crustal deformation in southern California constrained by radial anisotropy from ambient noise adjoint tomography. *Geophysical Research Letters*, *47*(12), e2020GL088580.

Wang, K., Yang, Y., Jiang, C., Wang, Y., Tong, P., Liu, T., & Liu, Q. (2021). Adjoint tomography of ambient noise data and teleseismic P waves: Methodology and applications to central California. *Journal of Geophysical Research: Solid Earth*, *126*(6), e2021JB021648.

Wang, X., Zhan, Z., Zhong, M., Persaud, P., & Clayton, R. W. (2021). Urban basin structure imaging based on dense arrays and bayesian array-based coherent receiver functions. *Journal of Geophysical Research: Solid Earth*, *126*(9), e2021JB022279.

Wang, Y., Chevrot, S., Monteiller, V., Komatitsch, D., Mouthereau, F., Manatschal, G., ... others (2016). The deep roots of the western Pyrenees revealed by full waveform inversion of teleseismic P waves. *Geology*, *44*(6), 475–478.

Wessel, P., Luis, J., Uieda, L., Scharroo, R., Wobbe, F., Smith, W. H., & Tian, D. (2019). The generic mapping tools version 6. *Geochemistry, Geophysics, Geosystems*, *20*(11), 5556–5564.

Whitmore, N. D. (1983). Iterative depth migration by backward time propagation.

In *Seg technical program expanded abstracts 1983* (pp. 382–385). Society of Exploration Geophysicists.

Wilson, D., & Aster, R. (2005). Seismic imaging of the crust and upper mantle using regularized joint receiver functions, frequency–wave number filtering, and multimode Kirchhoff migration. *Journal of Geophysical Research: Solid Earth*, *110*(B5).

Withers, M., Aster, R., Young, C., Beiriger, J., Harris, M., Moore, S., & Trujillo, J. (1998). A comparison of select trigger algorithms for automated global seismic phase and event detection. *Bulletin of the Seismological Society of America*, *88*(1), 95–106.

Wu, S.-M., Huang, H.-H., Lin, F.-C., Farrell, J., & Schmandt, B. (2023). Extreme seismic anisotropy indicates shallow accumulation of magmatic sills beneath Yellowstone caldera. *Earth and Planetary Science Letters*, *616*, 118244.

Xu, S., Zhang, Y., Pham, D., & Lambaré, G. (2005). Antileakage Fourier transform for seismic data regularization. *Geophysics*, *70*(4), V87–V95.

Yang, J., Huang, J., Zhu, H., McMechan, G., & Li, Z. (2022). Introduction to a Two-Way Beam Wave Method and Its Applications in Seismic Imaging. *Journal of Geophysical Research: Solid Earth*, *127*(6), e2021JB023357.

Yang, J., Zhu, H., & Lumley, D. (2020). Time-lapse imaging of coseismic ruptures for the 2019 ridgecrest earthquakes using multiazimuth backprojection with regional seismic data and a 3-D crustal velocity model. *Geophysical Research Letters*, *47*(9), e2020GL087181.

Yang, J., Zhu, H., Wang, W., Zhao, Y., & Zhang, H. (2018). Isotropic elastic reverse time migration using the phase-and amplitude-corrected vector P-and S-wavefields. *Geophysics*, *83*(6), S489–S503.

Yang, X., Pavlis, G. L., Hamburger, M. W., Marshak, S., Gilbert, H., Rupp, J., … Carpenter, N. S. (2017). Detailed crustal thickness variations beneath the Illinois Basin area: Implications for crustal evolution of the midcontinent. *Journal of Geophysical Research: Solid Earth*, *122*(8), 6323–6345.

Yi, J., Liu, Y., Yang, Z., Lu, H., He, B., & Zhang, Z. (2019). A least-squares correlation-based full traveltime inversion for shallow subsurface velocity reconstruction. *Geophysics*, *84*(4), R613–R624.

Yuan, X., Kind, R., Li, X., & Wang, R. (2006). The S receiver functions: synthetics and data example. *Geophysical Journal International*, *165*(2), 555–564.

Zhang, C., Yao, H., Liu, Q., Zhang, P., Yuan, Y. O., Feng, J., & Fang, L. (2018). Linear array ambient noise adjoint tomography reveals intense crust-mantle interactions in North China Craton. *Journal of Geophysical Research: Solid Earth*, *123*(1), 368–383.

Zhang, H., van der Lee, S., Wolin, E., Bollmann, T. A., Revenaugh, J., Wiens, D. A., ... others (2016). Distinct crustal structure of the North American Midcontinent Rift from P wave receiver functions. *Journal of Geophysical Research: Solid Earth*, *121*(11), 8136–8153.

Zhang, J., & Zheng, T. (2015). Receiver function imaging with reconstructed wavefields from sparsely scattered stations. *Seismological Research Letters*, *86*(1), 165–172.

Zhao, D., Hasegawa, A., & Horiuchi, S. (1992). Tomographic imaging of P and S wave velocity structure beneath northeastern Japan. *Journal of Geophysical Research: Solid Earth*, *97*(B13), 19909–19928.

Zhao, H. (2005). A fast sweeping method for eikonal equations. *Mathematics of computation*, *74*(250), 603–627.

Zheng, T., Zhao, L., & Zhu, R. (2008). Insight into the geodynamics of cratonic reactivation from seismic analysis of the crust-mantle boundary. *Geophysical Research Letters*, *35*(8).

Zhu, H. (2017). Elastic wavefield separation based on the Helmholtz decompositionElastic wavefield separation. *Geophysics*, *82*(2), S173–S183.

Zhu, H., Bozdağ, E., Peter, D., & Tromp, J. (2012). Structure of the European upper mantle revealed by adjoint tomography. *Nature Geoscience*, *5*(7), 493–498.

Zhu, H., Stern, R. J., & Yang, J. (2020). Seismic evidence for subduction-induced mantle flows underneath Middle America. *Nature communications*, *11*(1), 2075.

Zhu, L. (2000). Crustal structure across the San Andreas Fault, southern California from teleseismic converted waves. *Earth and Planetary Science Letters*, *179*(1), 183–190.

Table 1: Teleseismic event information for passive source RTM using the Laramie array.

Event	Original Time	Lon(°)	Lat(°)	Depth(km)
P1	2000_10_04_14_37_44	-62.5590	11.1240	110.3
P2	2000_10_05_13_39_11	-40.9580	31.7320	10
P3	2000_11_08_06_59_58	-77.8290	7.0420	17
P4	2000_11_29_10_25_13	-70.8860	-24.8690	58.2
P5	2000_12_12_05_26_45	-82.6790	6.0150	10
P6	2001_01_10_16_02_42	-153.2810	56.7744	36.4
P7	2001_01_13_17_33_32	-88.6600	13.0490	60
P8	2001_02_13_14_22_05	-88.9380	13.6710	10
P9	2001_03_24_06_27_53	132.5260	34.0830	50
P10	2001_04_09_09_00_57	-73.1090	-32.6680	11
P11	2001_04_14_23_27_26	141.7680	30.0920	10
S1	2000_10_04_16_58_44	166.9100	-15.4210	23
S2	2000_10_27_04_21_51	140.4600	26.2660	388
S3	2000_10_29_08_37_08	153.9450	-4.7660	50
S4	2000_12_21_01_01_27	151.1220	-5.7060	33
S5	2001_01_09_16_49_28	167.1700	-14.9280	103
S6	2001_04_09_09_00_57	-73.1090	-32.6680	11
S7	2001_04_14_23_27_26	141.7680	30.0920	10
S8	2001_04_28_04_49_53	-176.9370	-18.0640	351.8

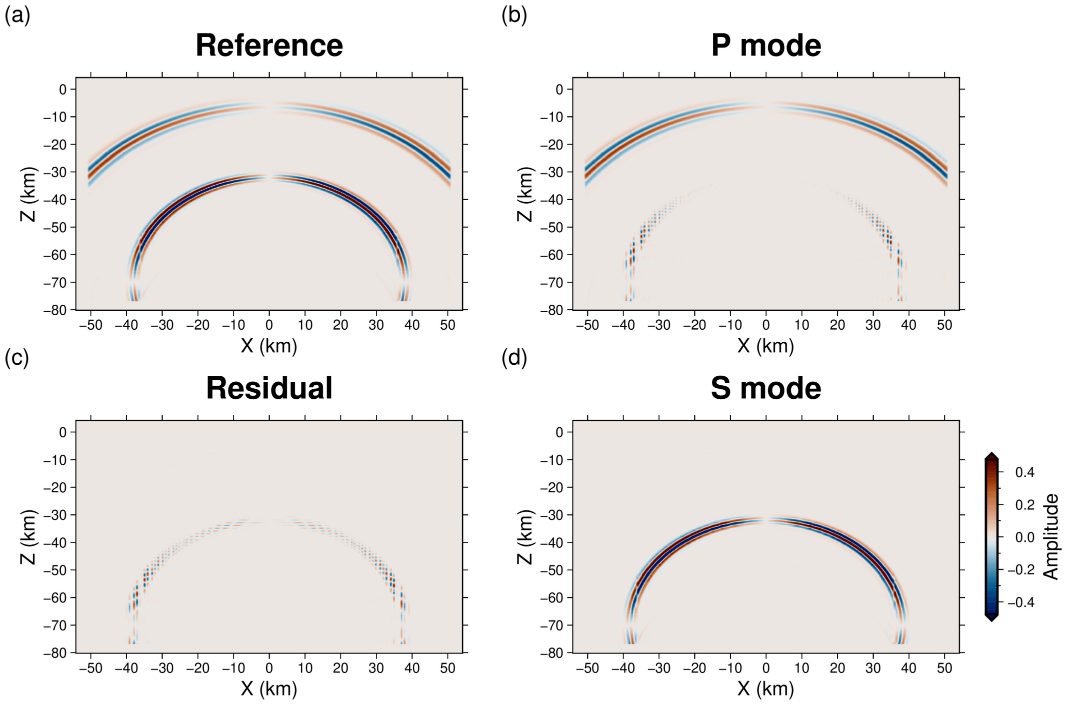

Figure 1: Strong-form solutions for wavefield decomposition based on Equation 6. Panel (a) shows the X component of the back-propagating elastic wavefield. Panels (b) and (d) represent the separated P and S wavefields, respectively. Panel (c) shows the difference between the reference (a) and the summation of strong-form decomposed P (b) and S (d) waves. The Z component has a similar phenomenon, which is not shown here.

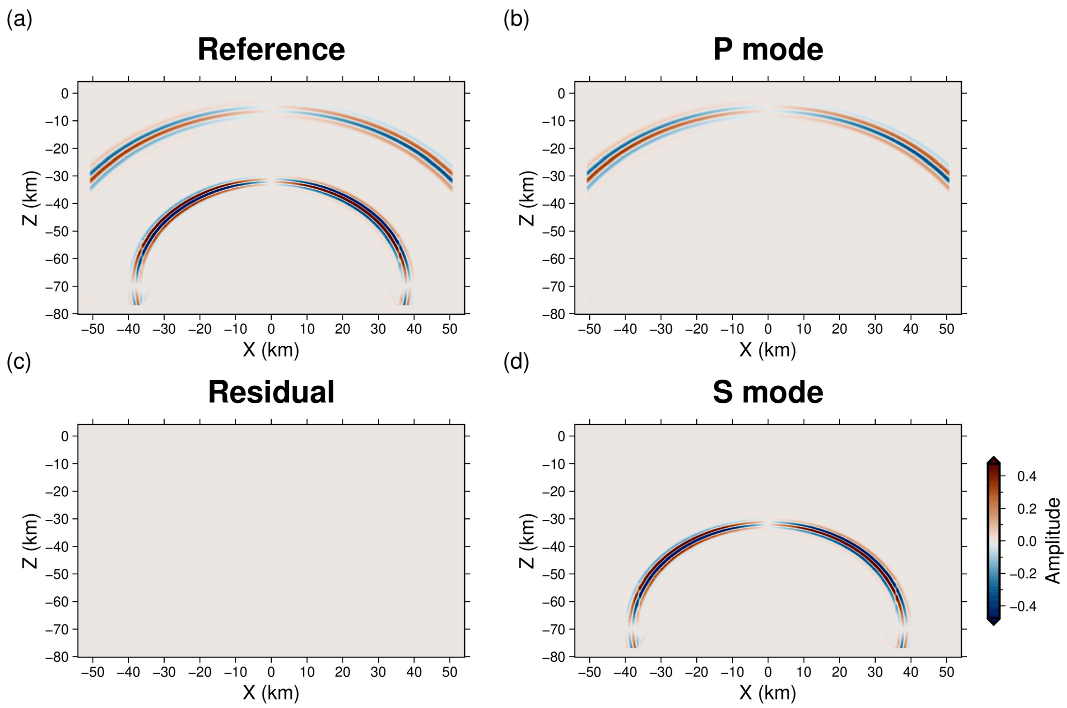

Figure 2: Same as Figure 1 but shows the decomposed wavefields based on Equations 7 and 8.

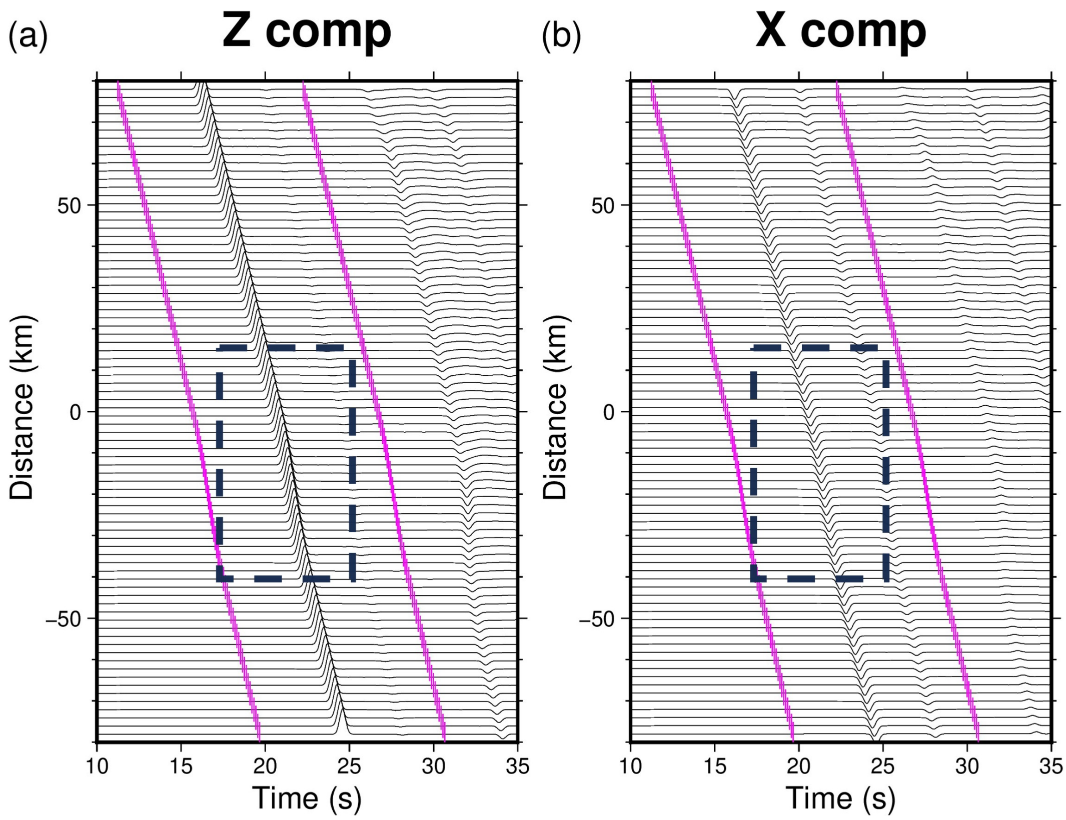

Figure 3: Synthetic teleseismic data with topographic changes in the model shown in Figure 4b. Panels (a) and (b) are Z and X component seismograms, respectively. The plane wave incident depth is 120 km, with a back azimuthal angle of 90°, and an incident angle of 27°. Therefore, X components could be considered as the radial components of teleseismic waves. The black dashed rectangle highlights the effect of topographic changes on recorded data. The magenta short lines denote the time window used to isolate waveforms for RTM.

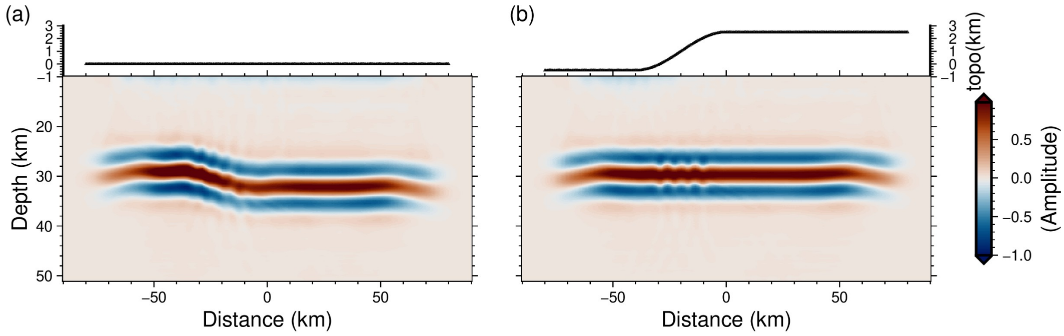

Figure 4: passive source RTM using 12 teleseismic events with incident-angles ranging from 12° to 27°. The back-azimuthal angle for the first six events is 90° and is 270° for the others. The black line on top of the image represents the station locations for injecting adjoint sources during migration. (a) Without considering the topographic variation, i.e., the stations are assumed to be at 0 km depth. (b) By considering the topographic variations, the stations are modeled at the correct elevations.

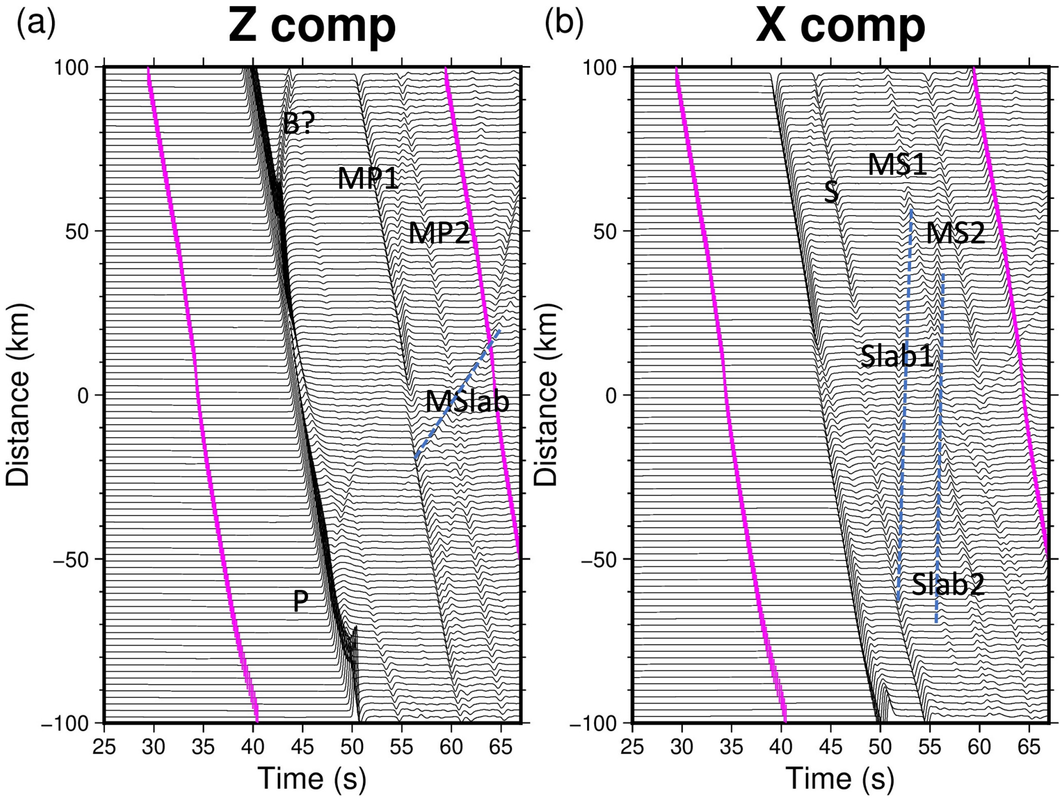

Figure 5: Synthetic Z (a) and X (b) components for the first teleseismic event with an incident angle of 27° and a back azimuthal angle of 90°. The magenta short lines denote the time window used to isolate waveforms for RTM. In panel (a), P denotes teleseismic P waves, MP1 and MP2 represent different-order P wave multiples. MSlab together with the dashed blue line, represent slab-related multiples. B is used to denote reflection artifacts due to absorbing boundary conditions. In panel (b), S denotes Ps-converted waves, MS1 and MS2 are corresponding P-multiple converted waves. Slab1 and Slab2 are slab-related Ps-converted waves.

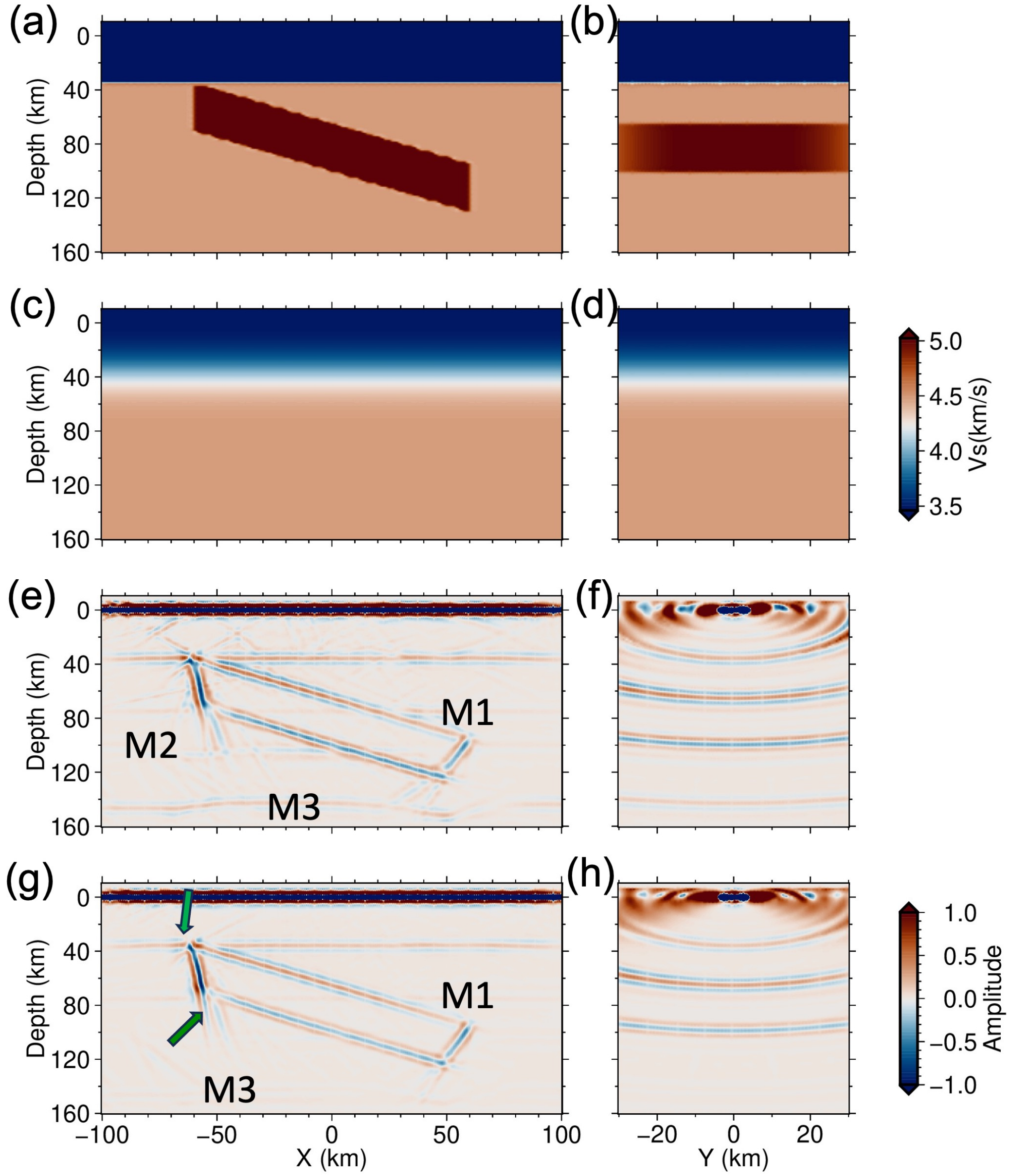

Figure 6: 3-D subducting slab imaging using 12 teleseismic events. The incident angle of the incident wavefield ranges from 12° to 27°. The back-azimuthal angle for events 1, 3, 7, 9 and 11 is 90° and 270° for the others. Panels (a) and (b) show the true velocity profile along the X (west-east) and Y (noth-source) directions for generating synthetic datasets. Panels (c) and (d) show the corresponding migration velocity along the same profiles, which is smoothed from the two-layer background model after removing the slab. Panels (e) and (f) show the stacked images from the first four teleseismic events, while panels (g) and (h) show the final image stacked over all teleseismic events. Panels (e-h) share the same color bars. M1, M2 and M3 in panels (e) and (g) represent multiple artifacts. The artifacts pointed by the green arrows are caused by strong scattering at the sharp edges of the slab.

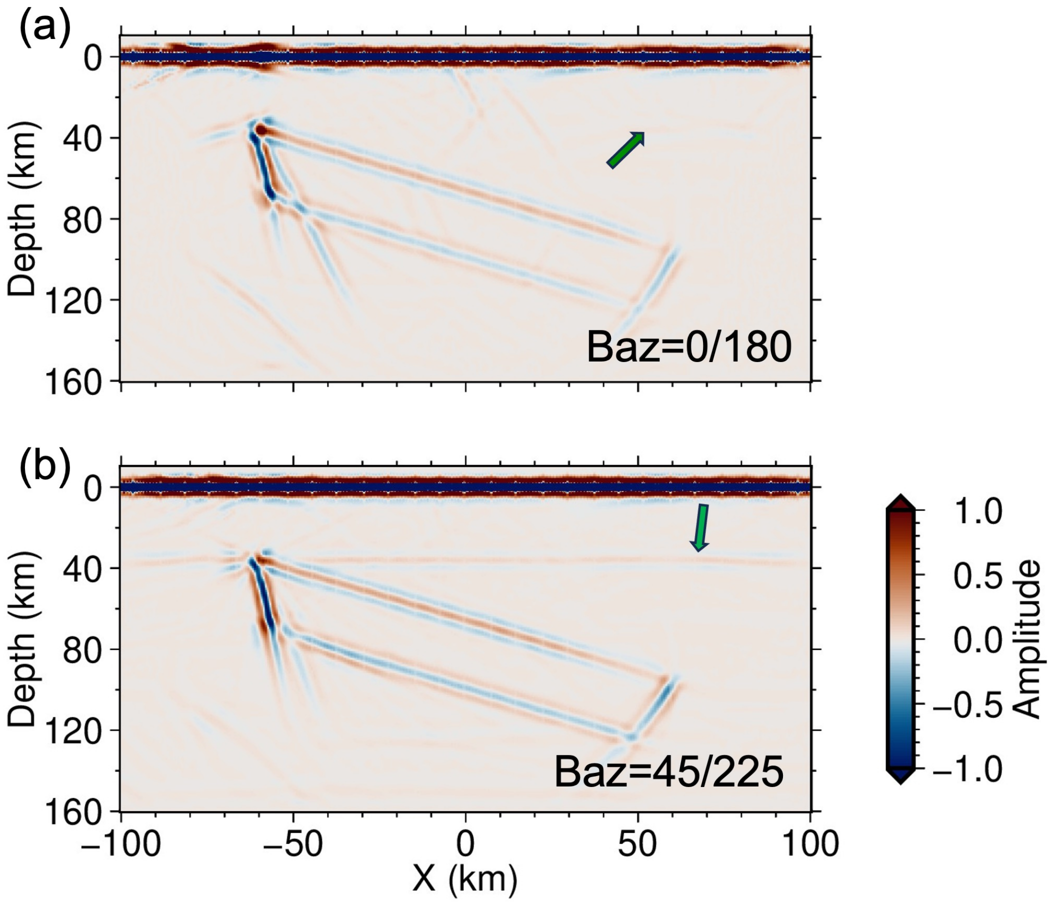

Figure 7: Similar to panel (g) in Figure 6, but the back azimuthal angles used for these two examples are 0° for events 1, 3, 7, 9 and 11, and 180° for the others (a), which are 45° and 225° in panel (b). The green arrows are used to compare imaged Moho interfaces with Figure 6.

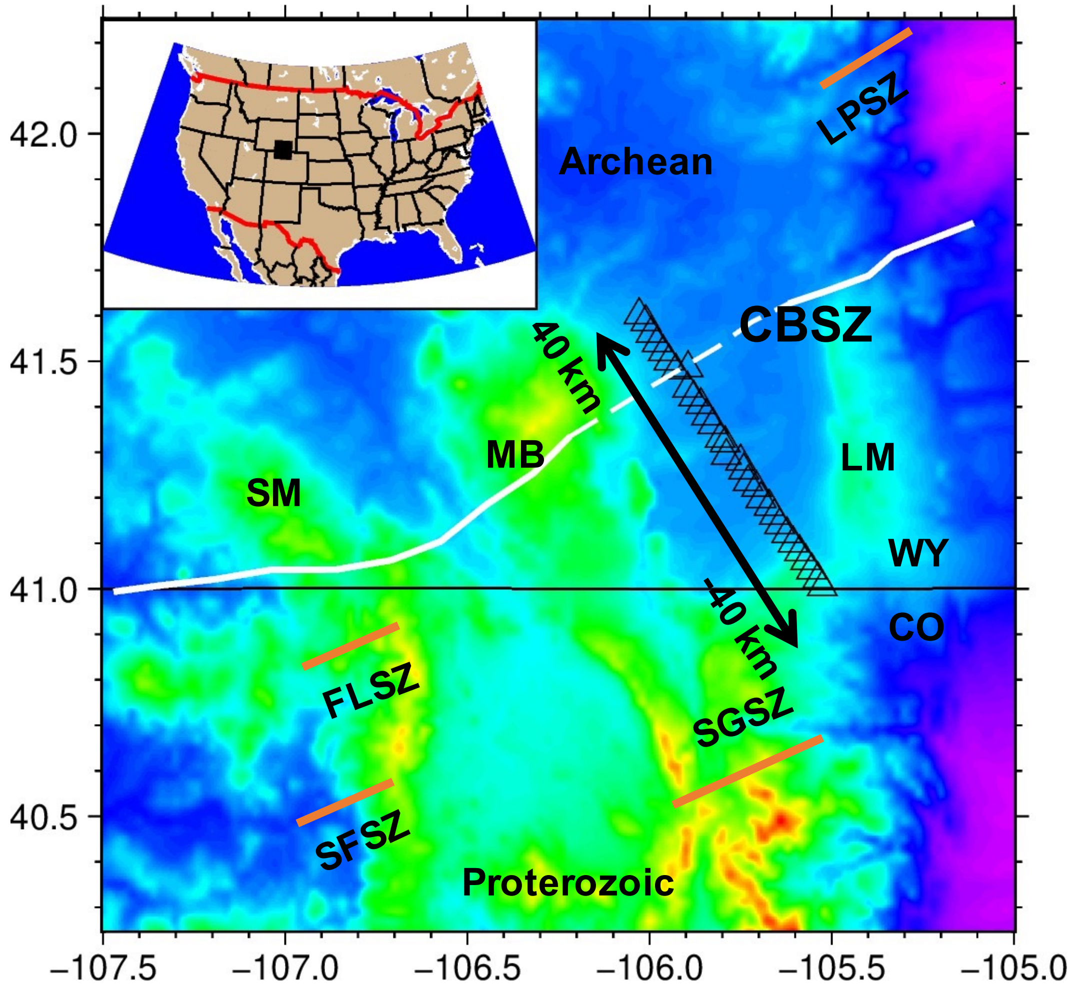

Figure 8: Geological settings of the study region after Hansen and Dueker (2009). The background shows the topography. Several shear zones: LPSZ, Laramie Peak shear zone; FLSZ, Farwell Mt. Lester Mt. suture zone; SFSZ, Soda Creek-Fish Creek shear zone; SGSZ, Skin Gulch shear zone, are denoted by orange lines to illustrate the complexity of the subsurface structures. Other geographic features: SM, Sierra Madres; MB, Medicine Bow Mountains and LM, Laramie Mountains are also labeled. The Cheyenne Belt suture (CB) is denoted by the white line, dashed where it is inferred. WY and CO denotes Wyoming and Colorado, respectively. The black rectangle in the upper-left inset map indicates the location of our study region in North America.

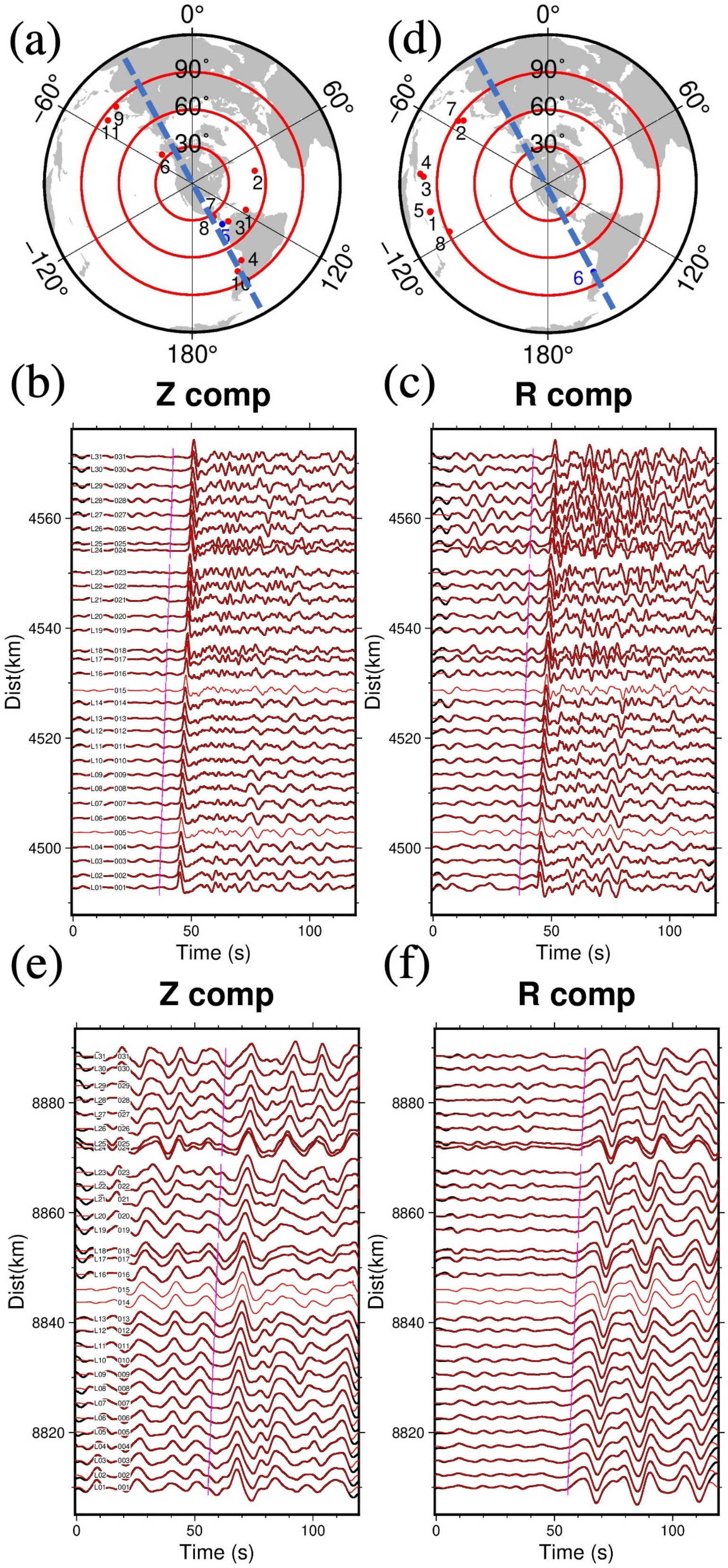

Figure 9: Caption next page.

Figure 9: Telseismic events and data used for migration. Red dots in Panels (a) and (d) represent the distributions of teleseismic P and S events. The light blue dashed line indicates the direction of the Laramie array. Panels (b) and (c) show the vertical (Z) and radial (R) components of the 5th (the blue dot in panel a) teleseismic P events recorded by the Laramie array. The background black solid lines denote the selected high-quality data (some traces are removed due to low signal-to-noise ratio), while the red solid lines represent the 2-D cubic-spline interpolated data at each station. Panels (e) and (f) represent the vertical and radial components of the 6th teleseismic S events. The magenta lines overlaying the seismograms denote either the onsets of P or S waves.

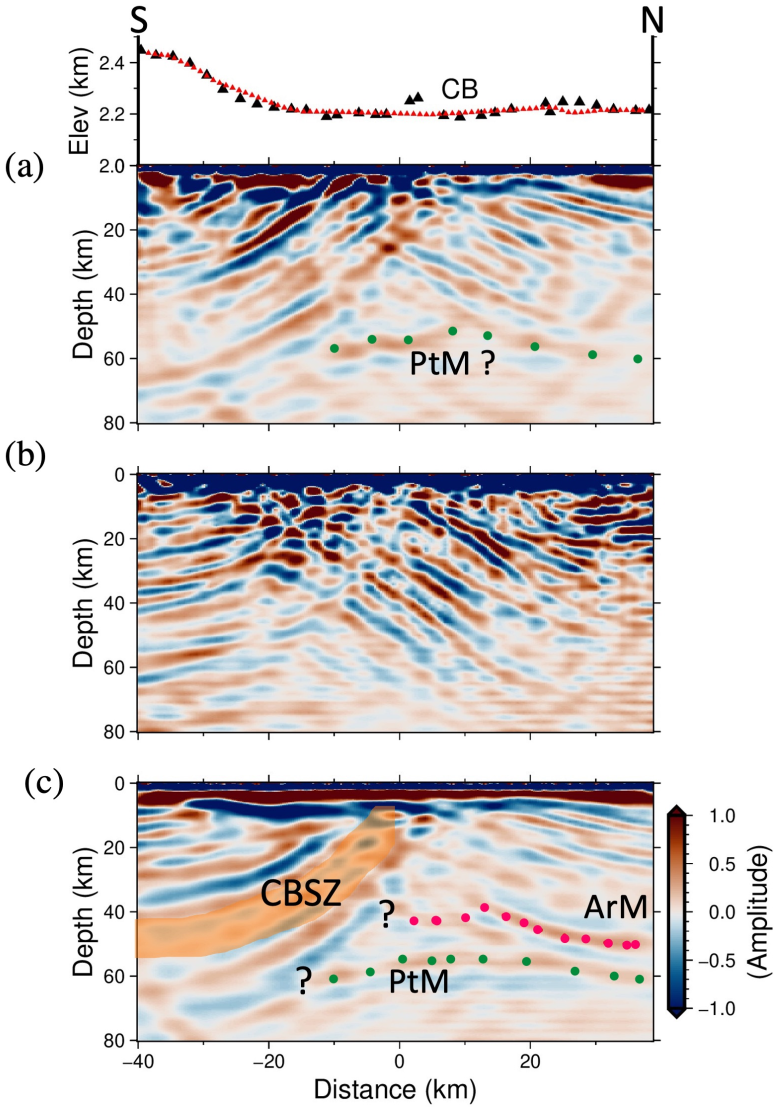

Figure 10: The passive source RTM image beneath the Laramie array. On the top of the figure, we show the elevation of raw (back triangles) and interpolated (red triangles) stations. CB represents the inferred CBSZ location on the surface. Panels (a) and (b) show the images obtained using teleseismic P and S events, respectively. Panel (c) shows the image obtained using interpolated teleseismic P events. The orange belt indicates the interpreted CBSZ. The magenta and dark green dots indicate the interpreted Archean Moho (ArM) and Proterozoic Moho (PtM).

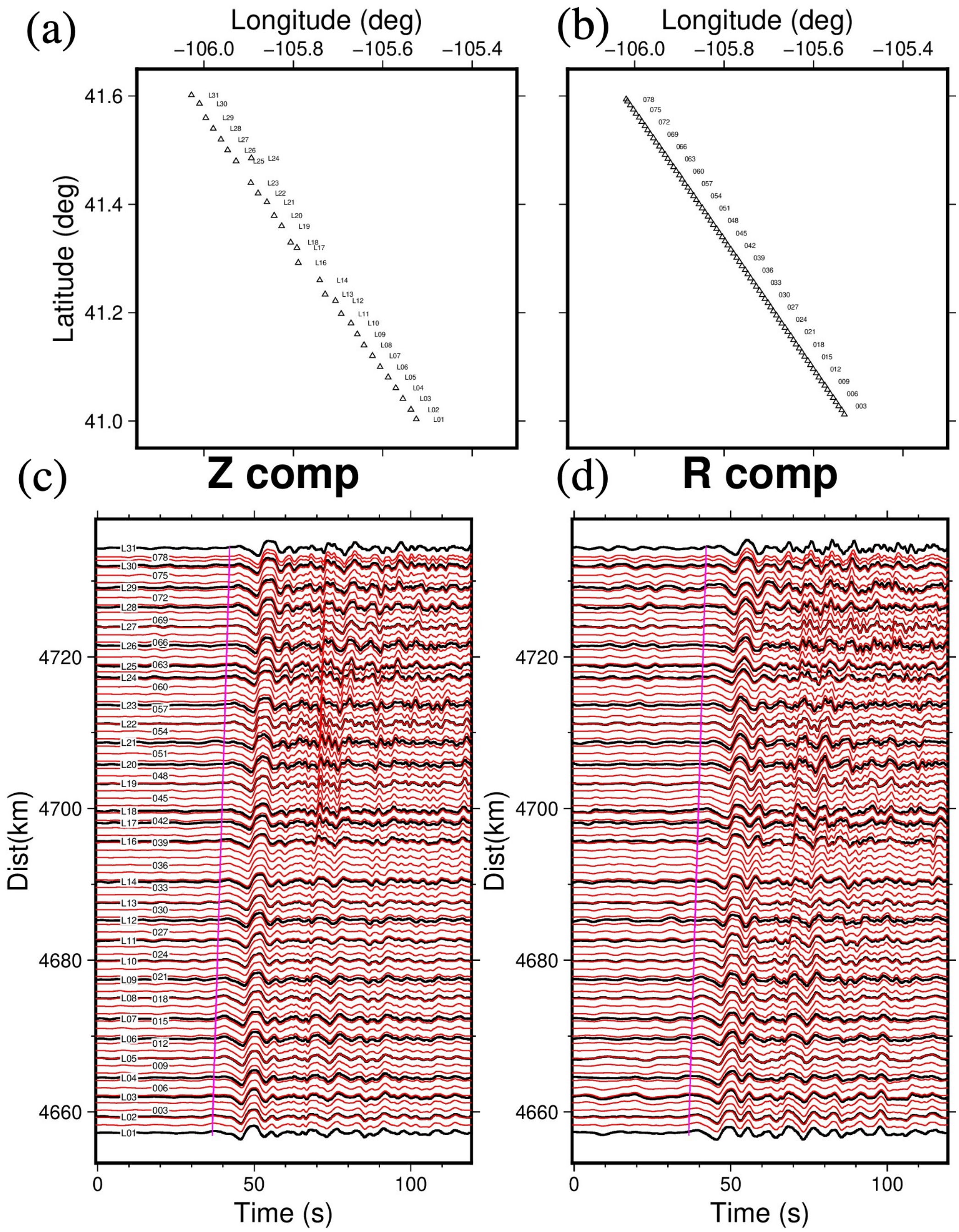

Figure 11: Regularization of the recorded teleseismic data to a fine grid. Panels (a) and (b) compare the raw and interpolation station locations. The interpolated station locations are obtained with GMT projection between the first (L01) and last station (L31) positions of the Laramie array along the great circle for every 1.0 km, which is not on a straight line after the UTM projection. Panels (c) and (d) show comparisons of the raw data (black) and interpolated seismograms (red) for vertical (Z) and radial (R) components, respectively.

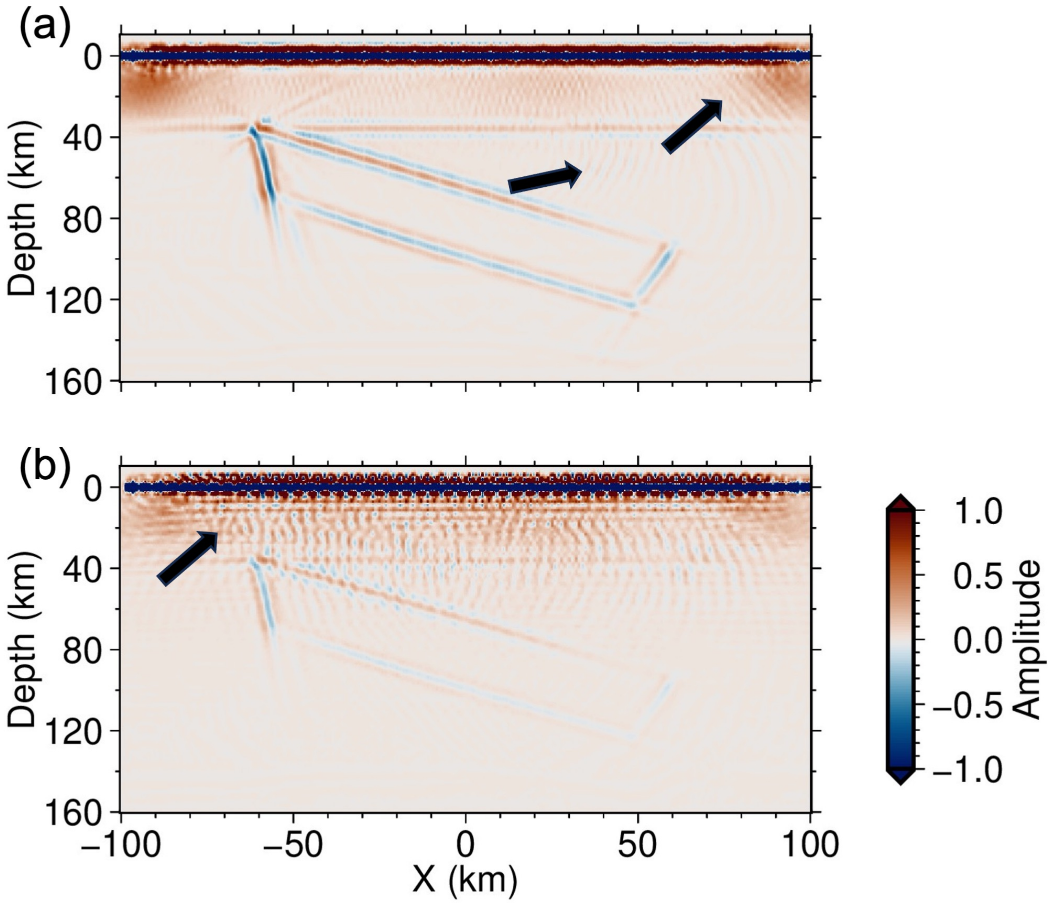

Figure 12: Imaging with sparse station spacing. The imaging parameters are the same as panel (g) in Figure 6 except that the station spacing is 2 km and 4 km for panels (a) and (b), respectively. The aliasing artifacts are illustrated by black arrows.

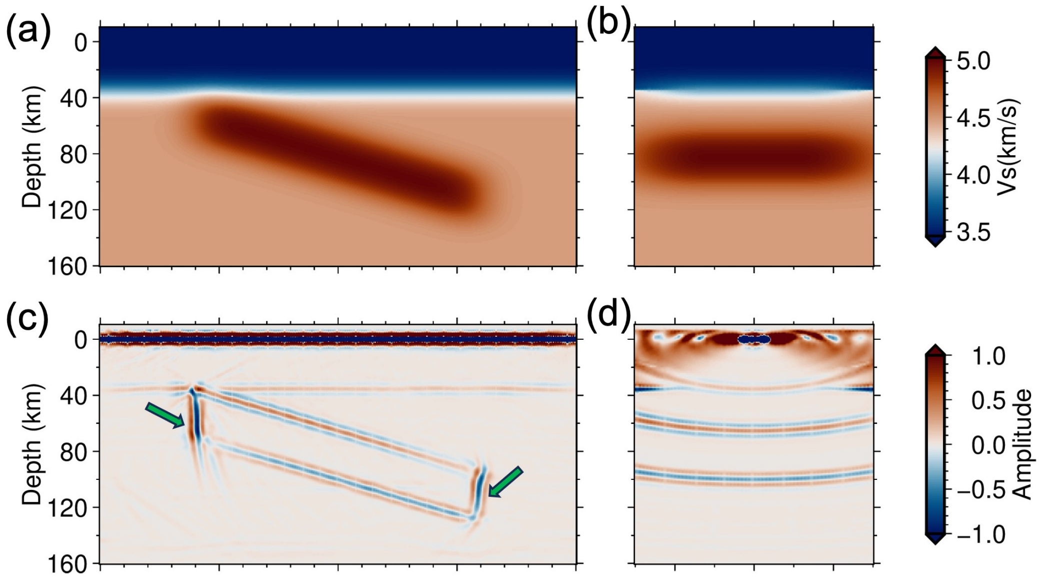

Figure 13: Imaging with a more accurate background migration velocity model. Panels (a) and (b) show the migration velocity profiles along the X (west-east) and Y (noth-source) directions. Panels (c) and (d) show the corresponding RTM images. The green arrows are used to highlight the improvement in imaging of the slab boundaries compared to panel (g) in Figure 6.

Passive source reverse time migration based on the spectral element method

Bin He[1], Yu Chen[1], David Lumley[1,2], Qinya Liu[3,4], Nozomu Takeuchi[5], Hitoshi Kawakatsu[5], and Hejun Zhu[1,2]

[1]Department of Geosciences, The University of Texas at Dallas, Richardson, TX 75080, USA
[2]Department of Physics, The University of Texas at Dallas, Richardson, TX 75080, USA
[3]Department of Physics, University of Toronto, Toronto M5S 1A7, Canada
[4]Department of Earth Sciences, University of Toronto, Toronto M5S 3B1, Canada
[5]Earthquake Research Institute, University of Tokyo, Tokyo 1130032, Japan

Key Points:

- A 3-D passive source reverse time migration based on the spectral element method is proposed to image complex structures.
- Amplitude-preserved vector P and S wavefields are accurately decomposed by solving corresponding weak-form solutions.
- Several south-dipping structures can be identified from P and S migration results beneath the Laramie basin, which are interpreted as the Cheyenne Belt suture zone.

Corresponding author: Hejun Zhu, `hejun.zhu@utdallas.edu`

Abstract

Increasing deployment of dense arrays has facilitated detailed structure imaging for tectonic investigation, hazard assessment and resource exploration. Strong velocity heterogeneity and topographic changes have to be considered during passive source imaging. However, it is quite challenging for ray-based methods, such as Kirchhoff migration or the widely used teleseismic receiver function, to handle these problems. In this study, we propose a 3-D passive source reverse time migration strategy based on the spectral element method. It is realized by decomposing the time reversal full elastic wavefield into amplitude-preserved vector P and S wavefields by solving the corresponding weak-form solutions, followed by a dot-product imaging condition to get images for the subsurface structures. It enables us to use regional 3-D migration velocity models and take topographic variations into account, helping us to locate reflectors at more accurate positions than traditional 1-D model-based methods, like teleseismic receiver functions. Two synthetic tests are used to demonstrate the advantages of the proposed method to handle topographic variations and complex velocity heterogeneities. Furthermore, applications to the Laramie array data using both teleseismic P and S waves enable us to identify several south-dipping structures beneath the Laramie basin in southeast Wyoming, which are interpreted as the Cheyenne Belt suture zone and agree with, and improve upon previous geological interpretations.

Plain Language Summary

Increasing deployment of dense arrays has allowed detailed structure imaging for tectonic investigation, hazard assessment and resource exploration. However, traditional ray-based migration methods or 1-D velocity model-based receiver function methods may greatly degrade the imaging quality without considering the full wavefield propagation effect and velocity heterogeneities. Therefore, in this study, we develop a 3-D passive source migration based on the spectral element method, which is capable of handling topographic variations as well as complex velocity heterogeneities for real data applications. Several synthetic tests and applications to the Laramie array data using both teleseismic P and S waves are used to demonstrate the capability of our method to image complex structures, such as subduction and suture zones.

1 Introduction

In past decades, teleseismic receiver functions have been widely used for imaging discontinuities within the Earth's crust and upper mantle (Burdick & Langston, 1977; Langston & Corvallis, 1977; Vinnik, 1977; Ai et al., 2007; Kawakatsu & Watada, 2007; Kind et al., 2012; H. Zhang et al., 2016; Long et al., 2019). Based on the assumption of a 1-D Earth model where discontinuities are horizontal, common convert point stacking (Dueker & Sheehan, 1997; L. Zhu, 2000; Gilbert et al., 2003) has generally been used to improve the image quality by mapping the receiver functions to depths. In the case of a single station, like the SEIS on Mars (Banerdt et al., 2020; Knapmeyer-Endrun et al., 2020; Lognonné et al., 2020) or sparse station distributions such as the USArray (Meltzer et al., 1999), such simplifications are natural and useful. However, it indeed degrades the image quality of geologically complex structures, such as subsurface environments with steep faults and laterally discontinuous interfaces, without considering the effects of wavefield diffraction and scattering caused by lateral variations of impedance contracts and velocities (L. Chen et al., 2005; Shang et al., 2012). In addition, increasing deployment of dense and nodal arrays has facilitated detailed structure imaging for tectonic investigation, hazard assessment and resource exploration (Okada et al., 2004; Zheng et al., 2008; Nábělek et al., 2009; H. Zhang et al., 2016; X. Yang et al., 2017; X. Chen et al., 2018; Li et al., 2018; Clayton et al., 2019; X. Wang et al., 2021; Onyango et al., 2022; Wu et al., 2023). Therefore, it calls for advanced imaging methods, such as seismic migration/inversion, which exploit the full complexity of recorded wavefields and rely less on a priori information about the Earth's structures, to get accurate images of complex subsurface discontinuities (Sheehan et al., 2000; L. Chen et al., 2005; Shang et al., 2012; Cheng et al., 2016; Li et al., 2018; Millet et al., 2019).

Among many seismic migration approaches, Kirchhoff migration/inversion (Schneider, 1978; Gray & May, 1994) has been widely used in the oil and gas industry to image shallow sedimentary structures owing to its high efficiency and simplicity. It was later introduced to global seismology for imaging large-scale structures using multi-component teleseismic data recorded by local dense arrays (Burridge et al., 1998; Bostock, 1998; Bostock & Rondenay, 1999; Rondenay et al., 2000; Bostock et al., 2001; Bostock, 2002; Levander et al., 2005; Rondenay, 2009; Liu & Levander, 2013; Cheng et al., 2016; Millet et al., 2019). Teleseismic Kirchhoff migration/inversion is implemented by weighting and stacking data along diffraction hyperbola for every possible scattering point in a regular grid

(Schneider, 1978; Gray & May, 1994; Bostock et al., 2001; Cheng et al., 2016; Millet et al., 2019). To date, most Kirchhoff migration/inversion approaches are based on the infinite high-frequency assumption by neglecting the finite frequency property of seismic wave propagation, which enables us to efficiently get images by using ray tracing (Richards & Aki, 1980) or solving the Eikonal equation (Gray & May, 1994; Cheng et al., 2016). However, It is difficult for ray-tracing to handle multiple arrivals, shadow zones, and even chaotic rays in complex subsurface environments (Audebert et al., 1997; L. Chen et al., 2005). Although the Eikonal equation-based Kirchhoff migration is capable of dealing with complex structures, it is not easy to handle the multipathing challenge (H. Zhao, 2005; Waheed et al., 2015; Tong, 2021). Furthermore, Kirchhoff migration requires more efforts to correct image amplitudes, and therefore, the wave-equation Kirchhoff migration has been developed to balance accuracy and efficiency (Andrade et al., n.d.; Jin & Etgen, n.d.). To mitigate the finite-frequency, multi-arrivals and inaccurate amplitude problems, Gaussian beam migration (Hill, 1990, 2001) has been proposed to apply local slant stacks by using complex-valued traveltimes and amplitudes. These complex quantities come from the approximation of seismic wave propagation with a sum of Gaussian beams, which are finite-frequency, ray-theoretical approximations to the wave equation (Notfors et al., n.d.). It is further extended to the wave-equation-based two-way beam wave method, which has comparable accuracy and efficiency in comparison to the wave-equation-based methods (J. Yang et al., 2022).

On the other hand, wave equation-based migration methods can essentially avoid most difficulties from the ray-based method by using the full wavefields (Claerbout, 1985). Among many different types of wave equation-based migration methods, synthetic and field experiments have shown that reverse-time migration (RTM) (Baysal et al., 1983; Whitmore, 1983; McMechan, 1983) has better performance for imaging complex structures. Active source RTM includes a forward wavefield modeling from the source and a backward wavefield modeling from the receivers, followed by applying imaging conditions to these two wavefields. In contrast, passive source RTM only requires one backward wavefield modeling for each earthquake. Therefore, inaccuracies due to source locations and velocity variations between earthquake locations and local study regions could be neglected. During the wavefield back-propagation, P and S wavefields are usually separated by polarization decomposition (Shang et al., 2012; H. Zhu, 2017; J. Yang et al., 2018). Then, the imaging condition is applied to cross-correlate separated P and S wavefields, followed by the summation of individual events. As pointed out by Shang et al. (2012), passive source RTM of converted waves differs fundamentally from single station receiver function analysis, and also in several important ways from more traditional receiver function migration (L. Chen et al., 2005). However, both current 2-D and 3-D pioneer works are based on the finite difference method, which requires projecting station locations on the model grids, and it is not easy to handle complex topography in real applications (Rajasekaran & McMechan, 1995; Bevc, 1997; Shragge, 2014; Shang et al., 2017; Yi et al., 2019). In addition, there are few real data applications for 3-D passive source RTM to image crustal and uppermost mantle structures.

In this study, we combine passive source RTM with the spectral-element method (SEM) (Komatitsch & Vilotte, 1998; Fichtner et al., 2009). Owning to its advantages in handling complex topographic variations, wavefield coupling between different media, flexibility to handle station distributions and so on, the SEM has been widely applied to construct crustal and mantle velocity models at regional and global scales (Tromp et al., 2005; Fichtner et al., 2009; Tape et al., 2009; Fichtner, 2010; Liu & Levander, 2013; H. Zhu et al., 2012; Y. Wang et al., 2016; K. Wang et al., 2020, 2021; Tromp, 2020; H. Zhu et al., 2020; Maguire et al., 2022). Here, we use it for passive source RTM. Because the wave-equation is solved in a weak-form fashion in SEM, directly taking strong-form spatial derivatives for wavefield decomposition results in significant discontinuities between element boundaries. To solve this problem, we propose to solve the corresponding weak-form solutions for P and S wavefield decomposition. This paper is organized into the following parts, we first briefly review passive source RTM based on the wavefield decomposition, followed by the theory of weak-form solutions for wavefield decomposition, and then several synthetic tests are used to demonstrate the advantages of the proposed method. Finally, we apply it to the Laramie array for suture zone imaging.

2 Methodology

2.1 Passive source RTM based on vector wavefield decomposition

Based on the principle that all back-propagating direct P and S receiver wavefields ($\mathbf{u}^P$ and $\mathbf{u}^S$) should coincide at "source" locations, wave-equation-based passive source imaging seeks strong energy in space as the source locations (McMechan, 1982; Nakata & Beroza, 2016; J. Yang et al., 2020; Duan et al., 2021). Similarly, the vector $\mathbf{u}^P$ and

$\mathbf{u}^S$ wavefields constructed by back-propagating multichannel direct P and Ps converted (or direct S and Sp converted) seismograms, should coincide at the scattering locations in depths, such as the Moho (Shang et al., 2012; Li et al., 2018). The imaging condition can be given as

$$I(\mathbf{x}) = \sum_{i_e=1}^{Ne} \int_{t=0}^{T} \boldsymbol{u}(\mathbf{x})_{i_e}^{P}(t) \cdot \boldsymbol{u}(\mathbf{x})_{i_e}^{S}(t) dt \quad , \tag{1}$$

where $I(\mathbf{x})$ is the image, $\boldsymbol{u}(\mathbf{x})_{i_e}^{P}$ and $\boldsymbol{u}(\mathbf{x})_{i_e}^{S}$ are the constructed vector P and S wavefields for i_eth event at the spatial coordinate $\mathbf{x}$. N_e is the total number of events for imaging. t represents the current time and T denotes the total time for wavefield back-propagation. " $\cdot$ " denotes the dot product between two vector fields. The final image is obtained by summing over all the time steps during wavefield back-propagation and all seismic events.

Because the vector $\mathbf{u}^P$ and $\mathbf{u}^S$ wavefields are coupled during elastic wavefield simulations, one may consider back-propagate multichannel P and Ps (or S and Sp) seismograms independently by solving two acoustic wave-equations (Sun et al., 2004; Duan et al., 2021) or decouple them during the wavefield back-propagation. H. Zhu (2017) proposed an amplitude-preserved wavefield decomposition method to decouple the vector $\mathbf{u}^P$ and $\mathbf{u}^S$ from elastic wavefield $\mathbf{u}$ by introducing a vector $\mathbf{w}$ in the form of

$$\nabla^2 \mathbf{w} = \mathbf{u} = \mathbf{u}^P + \mathbf{u}^S \quad , \tag{2}$$

where vector P and S wavefields can be obtained according to

$$\mathbf{u}^P = \nabla(\nabla \cdot \mathbf{w}), \quad \mathbf{u}^S = -\nabla \times \nabla \times \mathbf{w} \quad . \tag{3}$$

Here ∇, $\nabla\cdot$ and $\nabla\times$ are the gradient, divergence and curl operators, respectively. However, solving Equation 3 requires explicitly solving the Poisson's equation in Equation 2. To reduce the computational costs, J. Yang et al. (2018) further extended this method to avoid solving Poisson's equation under the isotropic media assumption with

$$\mathbf{u}^P = \nabla(\nabla \cdot \alpha^2 \hat{\mathbf{u}}), \quad \mathbf{u}^S = -\nabla \times (\nabla \times \beta^2 \hat{\mathbf{u}}) \quad , \tag{4}$$

where $\hat{\mathbf{u}}$ denotes the extrapolated wavefield excited by a double integral of the original seismograms, α and β are the local P and S velocities, respectively.

2.2 Strong- and weak-form solutions for the wavefield decomposition

In this section, we introduce H. Zhu (2017) and J. Yang et al. (2018)'s method to the SEM, so that it is more convenient to handle irregular surface topography and station locations. Different from the finite difference (FD) method, SEM seeks a weak solution $\bar{\boldsymbol{u}}(\mathbf{x},t)$ to the equation of motion in the Galerkin sense (Komatitsch & Vilotte, 1998; Fichtner, 2010). Lagrange polynomials collocated at the Gauss–Lobatto–Legendre(GLL) points are used to interpolate the wavefield at any spatial locations in the form of

$$\boldsymbol{u}(\mathbf{x},t) \approx \bar{\boldsymbol{u}}(\mathbf{x},t) = \sum_{i,j,k=1}^{N+1} \boldsymbol{u}^{ijk}(t) L_{ijk}(\mathbf{x}) \quad , \tag{5}$$

where $\boldsymbol{u}(\mathbf{x},t)$ and $\bar{\boldsymbol{u}}(\mathbf{x},t)$ represent the true and weak-form solutions of the wave-equation, respectively. $\mathbf{x}$ represents the spatial coordinate and t represents time. N denotes the degree of the Lagrange polynomials, and therefore we have $N+1$ GLL points for one element along each direction. $L_{ijk} = l_i(x)l_j(y)l_k(z)$ represents the basis function chosen as the product of three Lagrange polynomials $l(x)$, $l(y)$ and $l(z)$ along the x, y and z directions collocated at the corresponding GLL points.

Owing to the continuous prosperities of the Lagrange polynomials, a straightforward solution of Equation 4 based on SEM, noted as the strong-form solution, can be realized by

$$\mathbf{u}^P = \nabla[\nabla \cdot \alpha^2 \sum_{i,j,k=1}^{N+1} \boldsymbol{u}^{ijk}(t) L_{ijk}(\mathbf{x})], \quad \mathbf{u}^S = -\nabla \times [(\nabla \times \beta^2 \sum_{i,j,k=1}^{N+1} \boldsymbol{u}^{ijk}(t) L_{ijk}(\mathbf{x})] \quad , \tag{6}$$

which is fairly easy to implement because the spatial derivatives from the gradient, divergence and curl operators are taken from the Lagrange polynomials. However, we expect quite strong artifacts in the separated vector wavefields, which could contaminate the final imaging result. As illustrated in Figure 1, strong S mode artifacts appear in the P mode. This is because the solution of SEM is a weak-form approximation, and although the wavefield is continuous cross elements, the continuity of spatial derivatives is not guaranteed. To mitigate this leakage during wavefield decomposition, we use the weak solutions for Equation 4 as follows:

$$\int_{G_e} \mathbf{\Phi} \cdot \mathbf{u}^P d^3\mathbf{x} = \int_{G_e} \mathbf{\Phi} \cdot \nabla(\nabla \cdot \alpha^2 \mathbf{u}) d^3\mathbf{x} = -\int_{G_e} [\nabla \cdot \mathbf{\Phi}][\nabla \cdot (\alpha^2 \mathbf{u})] \quad , \tag{7}$$

$$\int_{G_e} \mathbf{\Phi} \cdot \mathbf{u}^S d^3\mathbf{x} = -\int_{G_e} \mathbf{\Phi} \cdot \nabla \times (\nabla \times \beta^2 \mathbf{u}) d^3\mathbf{x} = \int_{G_e} [\nabla \times \mathbf{\Phi}] \cdot [\nabla \times \beta^2 \mathbf{u}] d^3\mathbf{x} \quad , \tag{8}$$

where $\mathbf{\Phi}$ denotes any arbitrary, differentiable, time-independent test function, which will be chosen as the basis functions similar to the way we get SEM solutions. As shown in Figure 2, both P and S modes are clearly separated without significant leakages. This indicates that the weak-form solutions can significantly improve the quality of wavefield decomposition, which is the basis for the following imaging tests. The deviations of Equations 7 and 8 can be found in the supplementary material.

2.3 The workflow for passive source RTM

The implementation of passive source RTM can be summarised in the following four steps:

1. Teleseimic data preprocessing. During this step, we estimate source time functions for each teleseismic event based on the principle component analysis for the aligned incident waves (Bostock & Rondenay, 1999; Shang et al., 2017), such as P, S or SKS waves. For this purpose, the incident waves are aligned according to the onset time of the incident phases estimated using the TauP package (Crotwell et al., 1999). Then, an iterative time deconvolution (Kikuchi & Kanamori, 1982) is applied to each component of original(unaligned) data to remove the source time function, followed by bandpass filtering for later finite frequency simulations.
2. Injecting the preprocessed teleseismic data for the SEM solver as adjoint sources to the acceleration vector. Given the linear relation between the source time function and wavefield, this step further avoids obtaining the double integral of the teleseismic data, which should be injected to construct the second time integral of the displacement wavefield indicated by Equation 4.
3. During the reverse time wavefield propagation, solving the weak-form solutions shown in Equations 7 and 8 to get vector wavefields $\mathbf{u}_{i_e}^{P}$ and $\mathbf{u}_{i_e}^{S}$, followed by applying the zero-lag cross-correlation imaging condition (Equation 1), noted as $\mathbf{I}_{ie}^{PS}$. To save computational costs, one may consider performing wavefield separation for every several time steps according to the Nyquist rule. We also apply the imaging condition to $\mathbf{u}_{i_e}^{P}$ with $\mathbf{u}_{i_e}^{P}$ to get the PP image as $\mathbf{I}_{i_e}^{PP}$.
4. Sum all corresponding event images to obtain $\mathbf{I}_{PS}$ and $\mathbf{I}_{PP}$, and then get the image with $\mathbf{I}_{PS} = \frac{\mathbf{I}_{PS}}{\mathbf{I}_{PP}+\epsilon}$ to compensate for energies at great depths. Here, ϵ is a small damping value used to avoid dividing by zeros.

3 Applications

In this section, we use two synthetic tests and one real data example to validate our method based on linear array recordings although we are using 3-D modeling and migration. It is well-known that station spacing together with the data frequency are important factors that may result in spatial aliasing during passive source RTM (Gray, 2013; Shang et al., 2012). Therefore, most teleseismic migration methods used to image lithospheric structures rely on dense arrays (station spacing is ∼5 km) (Bostock, 1998; Rondenay et al., 2000; Rondenay, 2009; Shang et al., 2017). Therefore, all synthetic simulations in our tests are implemented using a 3-D plane-wave injection method, FK-SEM (Tong, Komatitsch, et al., 2014; Tong, Chen, et al., 2014) and recorded by a dense linear array. Then, passive source RTM is implemented based on 3-D migration. We note here, there are mainly three advantages to implement 3-D rather than 2-D migration even using recordings from a linear array: 1) no 3-D/2-D transformation is needed ("Line-source simulation for shallow-seismic data. Part 1: Theoretical background, author=Forbriger, Thomas and Groos, Lisa and Schäfer, Martin", 2014; Schäfer et al., 2014; C. Zhang et al., 2018), which is important to correct phase and amplitude differences between 3-D and 2-D simulations; 2) more teleseismic events can be chosen for real data applications; 3) no needs to project stations onto a line, which is required for 2-D migration even with linear arrays because their locations are not critically located on 2-D linear mesh grid (Shang et al., 2017).

3.1 Synthetic test 1: effects of topographic variations

The first synthetic test is used to highlight the effects of topographic variations on passive source migration when using high-frequency teleseismic data. The input model is a two-layer model with an interface at 30 km depth. The density, Vp and Vs for the first layer between 0 and 30 km depth are 2.72 g/cm^3, 5.8 km/s and 3.46 km/s, which are 3.423 g/cm^3, 8.06 km/s and 4.53 km/s between 30 and 60 km depths. These values are taken from the AK135 model (Kennett et al., 1995). The simulation domain spans -90 to 90 km along the X (longitude) direction, -60 to 60 km along the Y (latitude) direction and 0 to 60 km along the depth direction. The element size is 1.0 km, which allows for the wavefield simulation with the highest frequency around 3.0 Hz. The Stacey absorption boundary condition is used for each face of the model except for the top, which is a free-surface boundary condition for our simulations (Mahrer, 1990). A 1.5-D topographic change (no change along the Y direction) following the solid line shown in Figure 4b is designed to validate its effects on passive source RTM. We note here, the model will be stretched in depth direction within the SPECFEM package to handle the topographic changes. 161 stations with a horizontal station spacing of 1.0 km are distributed on the surface of the model. We use a Ricker source wavelet with a peak frequency of 1.0 Hz to initialize the incident plane waves. 12 P-wave plane waves, with incident angles ranging from 12°-27°, are injected into the local simulation domain to simulate the teleseismic waves. The back-azimuthal angles for events 1, 3, 7, 9 and 11 are 90° and 270° for the rest events. This makes a symmetric coverage of plane waves propagating through the model. The corresponding teleseismic data are recorded by the station for each event. Seismograms for the first teleseismic event with an incident angle of 27° and the back-azimuthal angle of 90° are shown in Figure 3. By using the short-time average over long-time average (STA/LTA) algorithm (Withers et al., 1998), it is feasible to detect the onset of the incident wavefield. The magenta lines in Figure 3 denote the time windows used in our imaging, which are 5 seconds before and 6 seconds after the onset of the incident P waves. It helps us to isolate multiple refections that may distort our imaging results. We speculate that the onset of incident P waves in both Z and X components shows the imprint of the topographic changes. Without considering the topographic changes, i.e., injecting teleseismic data at 0 km elevation of each station, a significant imprint of topography can be observed in the imaging result in Figure 4a, which looks like a mirror of the topography. On the contrary, the reflector can be accurately imaged by injecting the teleseismic data at the right locations by considering the topographic changes (Figure 4b).

3.2 Synthetic test 2: imaging subduction slabs

In this synthetic test, we validate the capability of our method to image complex structures in subduction zones. The background model is a two-layer crust and mantle structure, with density, Vp and Vs, the same as the previous example. A 3-D subducting slab (Figure 6a-b) is designed between -60 to 60 km along the X (Longitude) direction, -30 to 30 km along the Y (Latitude) direction and 40 to 140 km in depth with a thickness of 50 km. The Moho depth is 35 km. The model parameters (density, Vp and Vs) of the subducting slab are 12% greater than the background model. Our simulation domain spans from -120 to 120 km along the X direction, -48 to 48 km along the Y direction and 0 to 160 km along the depth direction. We use 201 stations with 1.0 km station spacing evenly distributed from -100.0 km to 100.0 km. 12 teleseismic P wave events with the same back-azimuth and incident angles as the previous example are injected into the local study region, starting from an initial depth at 240 km. The rest parameters are the same as the previous synthetic test. Synthetic Z and X component seismograms for the first teleseismic event are illustrated in Figures 5a and b. Because the back-azimuth angle of this event is 90°, the X components are equal to the radial components, which could be used to investigate Ps-converted waves. Due to the complexity of the velocity model, we speculate several kinds of multiple reflections (Moho and slab-related) for the P waves in Z components. The corresponding Ps-converted waves can be investigated from X components in Figure 5b. Interestingly, despite being weaker than Moho-related converted waves (S), slab-related as well as multiple reflection-related S-converted waves can also be seen.

Our RTM is implemented using a smoothed two-layer background model (Figures 6 c-d) to avoid artifacts arising from sharp velocity interfaces during the wavefield separation (J. Yang et al., 2018). It is smoothed vertically using a Gaussian function with a radius of 5.0 km. This means we do not include the slab in our migration velocity model, which is close to the real cases. After stacking and illuminating, the interfaces of the slab are well imaged as displayed in Figure 6g. It suggests that our method is capable of imaging complex structures, such as velocity anomalies with high dipping angles. Because it is quite difficult to isolate multiple reflections in this case, we also see different-order multiple imaging artifacts in our stacked result. We also show the imaging result from the first four teleseismic events, which also successfully captures the main features of the slab and the Moho, but with stronger artifacts due to not enough stacking. In addition, the images along the Y (Latitude) direction (Figures 6f and h), which is perpendicular to our stations' distribution, indicate that with only several effective stations, the migration will map the converted waveforms along the isochrone interfaces in depths (Schneider, 1978). Because we only use one linear array across the slab, it is necessary to consider the contributions of teleseismic events with back-azimuthal angles away from the array direction. We test another three back-azimuthal angle pairs, which are 0°/180°, 45°/225° and 135°/315° with the same incident angle as the previous test. Figure 7 shows the migration results from the back-azimuthal angle pairs of 0°/180° and 45°/225°. The migration result from 135°/315° azimuthal-angle pair is similar to the one from 45°/225°. As expected, when the azimuthal angles are away from the linear array direction, the interfaces of the imaged slab and the Moho become weaker and more incoherent artifacts become stronger. Interestingly, the Moho interface disappears when using teleseismic events with the 0°/180 ° azimuthal pair. This could be explained by the concept of the Fresnel zone. Bostock (1998) pointed out that the Fresnel zone of the scattering points depends on the dominant frequencies and depths of the interface. Assuming that constructive interference arises for phase differences less than a quarter period, the diameter of the Fresnel zone around the interface varies between ∼25 km for P_mS (Moho converted wave) at 0.5 Hz to ∼160 km for $P_{660}S$ (generated at the 660 km discontinuity) at 0.25 Hz. This means the converted waves recorded at stations that arise from deeper interfaces (e.g., X=0, Y=0 and Z=660 km) could be the response to a larger range of interfaces, e.g., X=[-80, 80], Y=[-80, 80], Z=[580, 740] km. We note here, the estimations of X and Y ranges are fairly rough. For teleseismic events with back-azimuthal angles away from the linear array, their Fresnel zone is also away from the structures beneath the linear array. As a consequence of small Fresnel zones, shallow interfaces, such as the Moho, gradually disappear beneath the linear array due to incoherence stacking from different events. Therefore, reasonable good station, incident angle and azimuthal angle coverages are preferred for our method if we intend to image the interfaces beneath a linear array (Shang et al., 2012; Li et al., 2018).

3.3 Imaging the Cheyenne Belt suture zone (CBSZ) using the Laramie array

3.3.1 Geological setting

The CBSZ is a tectonic suture zone between the Archean Wyoming craton to the north and the Paleoproterozoic Yavapai province to the south (Karlstrom & Houston, 1984; Sims & Stein, 2003; Hansen & Dueker, 2009; Jones et al., 2010). It contains a set of steeply south-dipping shear zones formed during the 1.78–1.75 Ga Medicine Bow orogeny when the Proterozoic Green Mountain arc collided with the passive margin of the Wyoming craton via south-facing subduction (Tyson et al., 2002; Hansen & Dueker, 2009). Steep stretching lineations and shear-sense features indicate south-side-up motion (Tyson et al., 2002; Hansen & Dueker, 2009). To better constrain the structure of the CBSZ, the Laramie array was deployed within the Laramie basin across the inferred trace of the Cheyenne belt (Figure 8) (Hansen & Dueker, 2009). It is a dense 80 km long linear array with broadband seismometers, which consists of 30 sensors spaced 2.2 km apart and was deployed for a period of eight months in 2000–2001. Based on P and S receiver functions together with teleseismic P wave traveltime tomography, Hansen and Dueker (2009) found an imbricated Moho north of the Cheyenne belt. It is basically consistent with the interpretation of seismic results from the CDROM (Continental Dynamics Rocky Mountain) project (Tyson et al., 2002). However, either due to the limited aperture of the Laramie array, or the methodologies, the CBSZ hasn't been clearly imaged as shown in Figure 7 of Hansen and Dueker (2009). Ruigrok et al. (2010) used seismic interferometry to extract reflection responses from the coda of the transmitted energy from distant earthquakes, where they found discontinuities in their migration images, which were interpreted as the CBSZ. Here, we use our passive source RTM method to further investigate the detailed shape of the CBSZ with converted teleseismic P and S waves.

3.3.2 Data

The teleseismic P wave dataset is constructed from 11 events at 30°–90° distance with body-wave magnitudes greater than 5.5. The S wave dataset is selected from 1 S-wave and 7 SKS events from 55°–85° and 85°-120° epicentral distances, respectively (Wilson & Aster, 2005; Yuan et al., 2006). Detailed information about these events can be found in Table 1 and displayed in Figure 9. The data is selected, downloaded and preprocessed with the standing order for data package (SOD) (Owens et al., 2004). For each P wave event, three-component waveforms within the time window of two minutes before and three minutes after direct P arrivals predicted by the AK135 model (Kennett et al., 1995) are collected. The north-south and west-east component seismograms are rotated to radial and transverse components after removing instrument response, linear trend, and mean values, followed by a bandpass filter of 1-20 s. Then, the preprocessed three-component waveforms of each event are visually inspected, and only those with a signal-to-noise ratio (SNR) larger than 3.0 and 2.0 for vertical and radial components are kept. Afterward, we use the open-source software AIMBAT (Lou et al., 2013) to remove bad seismograms with spurious amplitudes and cross-correlation coefficients lower than 0.80 for vertical and radial components. To avoid spatial aliasing, only events with more than 15 seismograms are remained. The data selection process for S and SKS events is similar except: (1) the time window is defined as two minutes before and three minutes after incident S arrivals; (2) seismograms with SNR larger than 2.0 and 3.0 for vertical and radial components are kept. This is because S waves are mainly in radial components. In the end, most events have more than 25 high-quality seismograms for each component.

Gray (2013) and Li et al. (2018) suggested that station spacing is an important factor for spatial aliasing during passive source RTM. For example, 5 km station spacing will result in slightly aliased P-wave migration with 1 Hz data, given the incident angles range from 12 ° to 27°. Therefore, we interpolate those deleted bad seismograms using 2-D cubic-spline interpolation (J. Zhang & Zheng, 2015). The 2-D cubic-spline interpolation was originally used to refine the receiver functions from sparse station distributions. Here, we use it to interpolate the aligned vertical and radial component seismograms. It mainly includes three steps: (1) align the seismograms according to the onset of incident waves (P or S), predicted by the reference model, such as AK135 (Kennett et al., 1995). The reference time could be further adjusted by applying a multichannel cross-correlation algorithm (VanDecar & Crosson, 1990); (2) perform 2-D interpolation for each time step using the cubic-spline method for each component; (3) shift the interpolated data back according to the reference time. We note here, the absolute amplitudes are kept during interpolation for each channel and component, which is different from J. Zhang and Zheng (2015). This is important for dealing with multi-component data. As compared in Figure 9, the interpolated seismograms follow the same trend of nearby stations in great details for both P and S waves. We use 10 s before and 30 s after the onset of P and 30 s before and 30 s after the onset of S waves for the following migration.

3.3.3 Migration

Our computational domain for wavefield propagation spans from -106.25° to -105.30° along longitude, 40.85° to 41.75° along latitude, and -10 to 110 km in the depth direction. We use 48, 60 and 80 elements along these three directions, yielding an average element size of 1.5 km. Given the minimal Vp of 5.05 km/s from our migration model and about two elements for each P wavelength, it allows us to use periods greater than 0.65 s for accurate wave simulation. A 7.5 km (about 3 elements) perfect-matched layer (PML) absorbing boundary condition is applied to each surface of the simulation domain to avoid artificial reflections from the boundaries (Komatitsch & Tromp, 2003). As outlined in section 2.3, source time functions are estimated from the aligned vertical component of each P wave event (radial for S wave), followed by an iterative time deconvolution (Kikuchi & Kanamori, 1982) to remove the source time function effect (Bostock, 1998; Rondenay et al., 2000; Bostock et al., 2001; Bostock, 2002; Shang et al., 2017). Given an average station spacing about 2-3 km, the deconvolved event data are bandpass filtered at 1-20 s as the adjoint sources for finite frequency wavefield modeling. The migration velocity model is extracted from a 3-D regional model US2016 (Shen & Ritzwoller, 2016). We smooth it using a Gaussian function with a radius of 5.0 km both vertically and horizontally. Then, the migration is implemented for each event and summed up to get the final stacked image. In this study, we perform the migration for P and S waves separately.

3.3.4 Results

Due to the finite frequency property, we identify velocity increase as positive migration phases flanked by negative ones as indicated by synthetic tests (Figures 4 and 6). The basement-sediment contact beneath the Laramie basin is identified in the P-wave image as the positive high amplitude phases beneath the negative phases around 2-7 km (Figure 10a), which becomes slightly deeper (dip to the northwest) between 30-40 km in the horizon, right beneath the Laramie basin. Whereas this feature is not clear from the S wave image shown in Figure 10b, possibly due to the back azimuthal angles of most S events being basically perpendicular to the array direction (Figure 9d). The most prominent features in both P and S wave images are the bunches of south-dipping positive/negative phases between -40 and 10 km in lateral direction and 0 and 70 km in depths. They are interpreted as the CBSZ, which situated juxtaposition of accreted Proterozoic terranes with the Archean Wyoming craton (Hansen & Dueker, 2009; Tyson et al., 2002). The northward crustal thickening seems to be indicated by the Proterozoic Moho, highlighted by dark green dots in the P wave image (Figure 10a). However, due to spatial aliasing in both P and S wave images between 20 and 40 km horizontally, the Archean Moho is not well constrained (Hansen & Dueker, 2009). Therefore, we try to suppress the spatial aliasing effect by refining the stations for every 1.0 km as illustrated in Figure 11. The comparison of the interpolated seismograms shows a good match both in trends and amplitudes of different events. We conduct P wave migration again using the refined data. As shown in Figure 11c, most spatial aliasing artifacts are suppressed and both the Archean Moho ($\sim$45 km) and the Proterozoic Moho ($\sim$60 km) can be clearly identified. They are slightly dipping northward to the north of the CBSZ. These are consistent with previous studies (Allmendinger et al., 1982; Prodehl et al., 1989; Snelson et al., 1998; Morozova et al., 2002). However, our Proterozoic Moho seems to be distorted with the CBSZ around 15 km in the horizontal direction (south of the CBSZ), whereas Hansen and Dueker (2009) found it to be continuous beneath the entire array. Nevertheless, we interpreted the CBSZ as the orange shadow zones in Figure 11c. Further investigation for a detailed migration velocity model will be helpful for better imaging and interpretation.

4 Discussions

We combine full wavefield passive source RTM with the spectral element method so that it is convenient to handle topographic changes and velocity heterogeneities. Both synthetic and suture zone imaging examples demonstrate the performance of our method.

4.1 2-D data interpolation

Migration antialiasing due to spatial frequency components (station spacing) is a longstanding problem in seismic imaging, for example, 5-D data interpolation (Trad, 2009) has been developed to improve the imaging quality. Therefore, it is important to consider the effects of station spacing for passive RTM (L. Chen et al., 2005; Li et al., 2018). The Nyquist-Shannon sampling theorem suggests that the station spacing is required to be smaller than the apparent half-wavelength to fully construct the wavefield from recorded seismograms at the surface (Gray, 2013; Li et al., 2018). Therefore, given constant crustal P and S wave velocities of 5.8 and 3.2 km/s, respectively, and incident angles of 12° to 27°, full construction of 1.0 Hz P waves at near-surface requires a station spacing ranging from 6.4 to 14.5 km, but 3.5 to 8.0 km for 1.0 Hz S waves. This gives us an upper bound limit for the station spacing. Smaller station spacing is expected because the incident angle for converted Ps waves could be larger, especially when the subsurface structures are complex, like subduction and suture zones. For example, given a high-frequency cut about 2.5 Hz, a 2.0 km station spacing would result in slight spatial aliasing as shown in Figure 12a compared to the result obtained with a 1.0 km station spacing shown in Figure 6g. As expected, a 4.0 km station spacing would result in even stronger spatial aliasing as shown in Figure 12b. Depending on the specific imaging target, 2-D data interpolation might be necessary for migration. However, most data interpolation (regularization) strategies developed for seismic exploration, like FX domain trace interpolation (Spitz, 1991), antileakage Fourier transformation (Xu et al., 2005) or curvelet transformation (Herrmann & Hennenfent, 2008; Shang et al., 2017) require linearity of station distributions, which is not straightforward to handle 2-D irregularly-spaced (3-D if we consider the station elevations) data. Therefore, we prefer to use the 2-D cubic-spline interpolation (J. Zhang & Zheng, 2015) or the radial function-based method (Shepard, n.d.), which can naturally handle irregularly-spaced data for our migration. We note here that, unlike its first application for interpolating 2-D receiver functions (J. Zhang & Zheng, 2015), we need to align the multi-channel data prior to interpolation for each component, and then shift the interpolated data back according to the onsets of incident waves for migration.

4.2 Source time function estimations

It is straightforward to estimate the source time functions for P waves, which has been successfully used for teleseismic full waveform inversion (Y. Wang et al., 2016; K. Wang et al., 2021). However, the estimation of source time functions for S waves should be carefully considered, because of relatively larger incident angles compared to P waves. This results in the leakage of S waves into vertical and transverse components. Therefore, rotation of vertical, radial and transverse components into P, SV and SH polarization directions could be helpful for source time function estimations for S waves (Bostock, 1998; Rondenay, 2009).

4.3 Migration velocity models

One advantage of our methodology is that we are able to implement migration based on 3-D velocity models with strong heterogeneities. The accuracy of migration velocity models is essential for mapping seismograms to correct locations and avoiding stacking artifacts (Mora, 1989; He & Liu, 2020). To illustrate the advantages of using more accurate migration velocity models for imaging, we conduct another migration for slab imaging, which is shown in Figure 13. The migration velocity model is obtained by smoothing the true velocity model using a Gaussian function with a radius of 5.0 km both horizontally and vertically. We speculate that, with a more reasonable migration velocity model, the vertical boundaries (see true model in Figure 6a) on the left and right sides of the slab are better constrained compared to those shown in Figure 6g. However, for our suture zone imaging, a smoothed regional 3-D model is not accurate enough because the grid spacing ($\sim$25 km) of model US2016 (Shen & Ritzwoller, 2016) is too large to capture velocity heterogeneities in such a small study region. Therefore, teleseismic body wave traveltime tomography (D. Zhao et al., 1992; Tong, 2021) or ambient noise tomography (C. Zhang et al., 2018) could be used to construct a more reasonable migration velocity model for our imaging in the future.

5 Conclusion

In this study, we propose to solve weak-form solutions to decompose elastic wavefields into vector P and S waves for teleseismic reverse time migration based on the spectral element method. Both synthetic tests and Cheyenne Belt suture zone imaging demonstrate the capability of our method to image complex structures with strong velocity heterogeneity. For linear array migration, our synthetic tests show that teleseismic events with back azimuthal angles parallel to the linear array direction contribute more to subsurface migration images than those away from the linear array direction. However, the latter could still contribute to the image beneath the array thanks to larger Fresnel zone contributions at greater depths. In addition, we reveal several south-dipping structures in the Laramie basin, which are interpreted as the Cheyenne Belt suture zone, and are consistent with geological interpretations from previous studies. For better performance of the migration-based imaging method, 2-D/3-D data interpolation is required to avoid spatial aliasing during the construction of wavefields in the subsurface.

Open Research

The Laramie array seismic data used in this study can be obtained from the IRIS Data Management Center (`https://ds.iris.edu/ds`) under the network codes XF. We use SPECFEM3-D Cartesian 4.0.0 (Komatitsch et al., 1999; Komatitsch & Tromp, 2002b, 2002a) published under the GPL 3 license for synthetic and real data simulations. PyGMT (Wessel et al., 2019) download from (`https://www.pygmt.org/latest/`) is used to plot figures.

Acknowledgments

This paper is contribution no. *** from the Department of Geosciences at the University of Texas at Dallas. The numerical results are computed through the Optane nodes on the UTD Seismology Group HPC clusters. This research is partially supported by the sponsors of the UT Dallas 3D + 4D Seismic Full Waveform Inversion research consortium.

Author Contributions

The authors confirm their contribution to the paper as follows: study conception and design: Hejun Zhu; Weak-form solutions were first proposed by Yu Chen, then theoretically derivated and tested by Bin He. Data collection: Bin He; Analysis and interpretation of results: Bin He, Hejun Zhu, David Lumley, Qinya Liu, Hitoshi Kawakatsu and Nozomu Takeuch; Draft manuscript preparation: Bin He, Hejun Zhu. All authors review the results and approve the final version of the manuscript.

References

Ai, Y., Chen, Q.-f., Zeng, F., Hong, X., & Ye, W. (2007). The crust and upper mantle structure beneath southeastern China. *Earth and Planetary Science Letters*, *260*(3-4), 549–563.

Allmendinger, R., Brewer, J., Brown, L., Kaufman, S., Oliver, J., & Houston, R. (1982). COCORP profiling across the Rocky Mountain Front in southern Wyoming, Part 2: Precambrian basement structure and its influence on Laramide deformation. *Geological Society of America Bulletin*, *93*(12), 1253–1263.

Andrade, P. N., Pestana, R. C., & dos Santos, A. W. (n.d.). Kirchhoff depth migration using maximum amplitude traveltimes computed by the Chebyshev polynomial recursion. In *14th International Congress of the Brazilian Geophysical Society & EXPOGEF, Rio de Janeiro, Brazil, 3-6 August 2015, pages=1109–1113, year=2015, organization=Brazilian Geophysical Society.*

Audebert, F., Nichols, D., Rekdal, T., Biondi, B., Lumley, D. E., & Urdaneta, H. (1997). Imaging complex geologic structure with single-arrival Kirchhoff prestack depth migration. *Geophysics*, *62*(5), 1533–1543.

Banerdt, W. B., Smrekar, S. E., Banfield, D., Giardini, D., Golombek, M., Johnson, C. L., ... others (2020). Initial results from the InSight mission on Mars. *Nature Geoscience*, *13*(3), 183–189.

Baysal, E., Kosloff, D. D., & Sherwood, J. W. (1983). Reverse time migration. *Geophysics*, *48*(11), 1514–1524.

Bevc, D. (1997). Flooding the topography: Wave-equation datuming of land data with rugged acquisition topography. *Geophysics*, *62*(5), 1558–1569.

Bostock, M. (1998). Mantle stratigraphy and evolution of the Slave province. *Jour-*

nal of Geophysical Research: Solid Earth, *103*(B9), 21183–21200.

Bostock, M. (2002). Kirchhoff-approximate inversion of teleseismic wavefields. *Geophysical Journal International*, *149*(3), 787–795.

Bostock, M., & Rondenay, S. (1999). Migration of scattered teleseismic body waves. *Geophysical journal international*, *137*(3), 732–746.

Bostock, M., Rondenay, S., & Shragge, J. (2001). Multiparameter two-dimensional inversion of scattered teleseismic body waves 1. Theory for oblique incidence. *Journal of Geophysical Research: Solid Earth*, *106*(B12), 30771–30782.

Burdick, L. J., & Langston, C. A. (1977). Modeling crustal structure through the use of converted phases in teleseismic body-wave forms. *Bulletin of the Seismological Society of America*, *67*(3), 677–691.

Burridge, R., de Hoop, M. V., Miller, D., & Spencer, C. (1998). Multiparameter inversion in anisotropic elastic media. *Geophysical Journal International*, *134*(3), 757–777.

Chen, L., Wen, L., & Zheng, T. (2005). A wave equation migration method for receiver function imaging: 1. Theory. *Journal of Geophysical Research: Solid Earth*, *110*(B11).

Chen, X., Li, Y., & Levin, V. (2018). Shear wave splitting beneath eastern North American continent: evidence for a multilayered and laterally variable anisotropic structure. *Geochemistry, Geophysics, Geosystems*, *19*(8), 2857–2871.

Cheng, C., Bodin, T., & Allen, R. M. (2016). Three-dimensional pre-stack depth migration of receiver functions with the fast marching method: a Kirchhoff approach. *Geophysical Journal International*, *205*(2), 819–829.

Claerbout, J. F. (1985). *Imaging the earth's interior* (Vol. 1). Blackwell Scientific Publications Oxford.

Clayton, R., Persaud, P., Denolle, M., & Polet, J. (2019). Exposing Los Angeles's shaky geologic underbelly, Eos, 100. *EOS. https://doi. org/10.1029*.

Crotwell, H. P., Owens, T. J., Ritsema, J., et al. (1999). The TauP Toolkit: Flexible seismic travel-time and ray-path utilities. *Seismological Research Letters*, *70*, 154–160.

Duan, C., Lumley, D., & Zhu, H. (2021). Estimation of micro-earthquake source locations based on full adjoint P and S wavefield imaging. *Geophysical Journal*

International, *226* (3), 2116–2144.

Dueker, K. G., & Sheehan, A. F. (1997). Mantle discontinuity structure from midpoint stacks of converted P to S waves across the Yellowstone hotspot track. *Journal of Geophysical Research: Solid Earth*, *102* (B4), 8313–8327.

Fichtner, A. (2010). *Full seismic waveform modelling and inversion.* Springer Science & Business Media.

Fichtner, A., Kennett, B. L., Igel, H., & Bunge, H.-P. (2009). Full seismic waveform tomography for upper-mantle structure in the Australasian region using adjoint methods. *Geophysical Journal International*, *179* (3), 1703–1725.

Gilbert, H. J., Sheehan, A. F., Dueker, K. G., & Molnar, P. (2003). Receiver functions in the western United States, with implications for upper mantle structure and dynamics. *Journal of Geophysical Research: Solid Earth*, *108* (B5).

Gray, S. H. (2013). Spatial sampling, migration aliasing, and migrated amplitudes. *Geophysics*, *78* (3), S157–S164.

Gray, S. H., & May, W. P. (1994). Kirchhoff migration using eikonal equation traveltimes. *Geophysics*, *59* (5), 810–817.

Hansen, S., & Dueker, K. (2009). P-and S-wave receiver function images of crustal imbrication beneath the Cheyenne Belt in southeast Wyoming. *Bulletin of the Seismological Society of America*, *99* (3), 1953–1961.

He, B., & Liu, Y. (2020). Wave-equation migration velocity analysis using Radon-domain common-image gathers. *Journal of Geophysical Research: Solid Earth*, *125* (2), e2019JB018938.

Herrmann, F. J., & Hennenfent, G. (2008). Non-parametric seismic data recovery with curvelet frames. *Geophysical Journal International*, *173* (1), 233–248.

Hill, N. R. (1990). Gaussian beam migration. *Geophysics*, *55* (11), 1416–1428.

Hill, N. R. (2001). Prestack Gaussian-beam depth migration. *Geophysics*, *66* (4), 1240–1250.

Jin, H., & Etgen, J. (n.d.). Evaluating Kirchhoff migration using wave-equation generated maximum amplitude traveltimes. In *SEG Technical Program Expanded Abstracts 2020, pages=2968–2972, year=2020, publisher=Society of Exploration Geophysicists.*

Jones, D. S., Snoke, A. W., Premo, W. R., & Chamberlain, K. R. (2010). New models for Paleoproterozoic orogenesis in the Cheyenne belt region: Evidence from the geology and U-Pb geochronology of the Big Creek Gneiss, southeastern Wyoming. *Bulletin*, *122*(11-12), 1877–1898.

Karlstrom, K., & Houston, R. (1984). The Cheyenne belt: Analysis of a Proterozoic suture in southern Wyoming. *Precambrian research*, *25*(4), 415–446.

Kawakatsu, H., & Watada, S. (2007). Seismic evidence for deep-water transportation in the mantle. *Science*, *316*(5830), 1468–1471.

Kennett, B. L., Engdahl, E., & Buland, R. (1995). Constraints on seismic velocities in the Earth from traveltimes. *Geophysical Journal International*, *122*(1), 108–124.

Kikuchi, M., & Kanamori, H. (1982). Inversion of complex body waves. *Bulletin of the Seismological Society of America*, *72*(2), 491–506.

Kind, R., Yuan, X., & Kumar, P. (2012). Seismic receiver functions and the lithosphere-asthenosphere boundary. *Tectonophysics*, *536*, 25–43.

Knapmeyer-Endrun, B., Bissig, F., Compaire, N., Garcia, R., Joshi, R., Khan, A., ... others (2020). First seismic constraints on the Martian crust-receiver functions for InSight.

Komatitsch, D., & Tromp, J. (2002a). Spectral-element simulations of global seismic wave propagation—II. Three-dimensional models, oceans, rotation and self-gravitation. *Geophysical Journal International*, *150*(1), 303–318.

Komatitsch, D., & Tromp, J. (2002b). Spectral-element simulations of global seismic wave propagation—I. Validation. *Geophysical Journal International*, *149*(2), 390–412.

Komatitsch, D., & Tromp, J. (2003). A perfectly matched layer absorbing boundary condition for the second-order seismic wave equation. *Geophysical Journal International*, *154*(1), 146–153.

Komatitsch, D., & Vilotte, J.-P. (1998). The spectral element method: an efficient tool to simulate the seismic response of 2D and 3D geological structures. *Bulletin of the seismological society of America*, *88*(2), 368–392.

Komatitsch, D., Vilotte, J.-P., Vai, R., Castillo-Covarrubias, J. M., & Sánchez-Sesma, F. J. (1999). The spectral element method for elastic wave equations—application to 2-D and 3-D seismic problems. *International Journal for numerical methods in engineering*, *45*(9), 1139–1164.

Langston, C., & Corvallis, O. (1977). crustal and upper mantle receiver structure from teleseismic P-waves and S-waves. *Bull. Seismol. Soc. Am*, *67*, 713–724.

Levander, A., Niu, F., Symes, W. W., & Nolet, G. (2005). Imaging teleseismic P to S scattered waves using the Kirchhoff integral. *GEOPHYSICAL MONOGRAPH-AMERICAN GEOPHYSICAL UNION*, *157*, 149.

Li, J., Shen, Y., & Zhang, W. (2018). Three-dimensional passive-source reverse-time migration of converted waves: The method. *Journal of Geophysical Research: Solid Earth*, *123*(2), 1419–1434.

Line-source simulation for shallow-seismic data. Part 1: Theoretical background, author=Forbriger, Thomas and Groos, Lisa and Schäfer, Martin. (2014). *Geophysical Journal International*, *198*(3), 1387–1404.

Liu, K., & Levander, A. (2013). Three-dimensional Kirchhoff-approximate generalized Radon transform imaging using teleseismic P-to-S scattered waves. *Geophysical Journal International*, *192*(3), 1196–1216.

Lognonné, P., Banerdt, W. B., Pike, W., Giardini, D., Christensen, U., Garcia, R. F., ... others (2020). Constraints on the shallow elastic and anelastic structure of Mars from InSight seismic data. *Nature Geoscience*, *13*(3), 213–220.

Long, M. D., Benoit, M. H., Aragon, J. C., & King, S. D. (2019). Seismic imaging of mid-crustal structure beneath central and eastern North America: Possibly the elusive Grenville deformation? *Geology*, *47*(4), 371–374.

Lou, X., Van Der Lee, S., & Lloyd, S. (2013). AIMBAT: A python/matplotlib tool for measuring teleseismic arrival times. *Seismological Research Letters*, *84*(1), 85–93.

Maguire, R., Schmandt, B., Li, J., Jiang, C., Li, G., Wilgus, J., & Chen, M. (2022). Magma accumulation at depths of prior rhyolite storage beneath Yellowstone Caldera. *Science*, *378*(6623), 1001–1004.

Mahrer, K. D. (1990). Numerical time step instability and Stacey's and Clayton-Engquist's absorbing boundary conditions. *Bulletin of the Seismological Society of America*, *80*(1), 213–217.

McMechan, G. A. (1982). Determination of source parameters by wavefield extrapolation. *Geophysical Journal International*, *71*(3), 613–628.

McMechan, G. A. (1983). Migration by extrapolation of time-dependent boundary values. *Geophysical prospecting*, *31*(3), 413–420.

Meltzer, A., Rudnick, R., Zeitler, P., Levander, A., Humphreys, G., Karlstrom, K.,

... others (1999). The USArray initiative. *Geological Society of America Today*, *9*, 8–10.

Millet, F., Bodin, T., & Rondenay, S. (2019). Multimode 3-D Kirchhoff migration of receiver functions at continental scale. *Journal of Geophysical Research: Solid Earth*, *124*(8), 8953–8980.

Mora, P. (1989). Inversion= migration+ tomography. *Geophysics*, *54*(12), 1575–1586.

Morozova, E., Wan, X., Chamberlain, K. R., Smithson, S. B., Morozov, I. B., Boyd, N. K., ... Foster, C. (2002). Geometry of Proterozoic sutures in the central Rocky Mountains from seismic reflection data: Cheyenne belt and Farwell Mountain structures. *Geophysical Research Letters*, *29*(13), 17–1.

Nábělek, J., Hetényi, G., Vergne, J., Sapkota, S., Kafle, B., Jiang, M., ... Team, t. H.-C. (2009). Underplating in the Himalaya-Tibet collision zone revealed by the Hi-CLIMB experiment. *Science*, *325*(5946), 1371–1374.

Nakata, N., & Beroza, G. C. (2016). Reverse time migration for microseismic sources using the geometric mean as an imaging condition. *Geophysics*, *81*(2), KS51–KS60.

Notfors, C., Xie, Y., & Gray, S. (n.d.). Gaussian Beam Migration-A Viable Alternative to Kirchhoff? In *68th EAGE Conference and Exhibition incorporating SPE EUROPEC 2006, pages=cp–2, year=2006, organization=EAGE Publications BV.*

Okada, Y., Kasahara, K., Hori, S., Obara, K., Sekiguchi, S., Fujiwara, H., & Yamamoto, A. (2004). Recent progress of seismic observation networks in Japan—Hi-net, F-net, K-NET and KiK-net. *Earth, Planets and Space*, *56*(8), xv–xxviii.

Onyango, E. A., Worthington, L. L., Schmandt, B., & Abers, G. A. (2022). Subduction Zone Interface Structure within the Southern MW9. 2 1964 Great Alaska Earthquake Asperity: Constraints from Receiver Functions Across a Spatially Dense Node Array. *Geophysical Research Letters*, *49*(15), e2022GL098334.

Owens, T. J., Crotwell, H. P., Groves, C., & Oliver-Paul, P. (2004). SOD: Standing order for data. *Seismological Research Letters*, *75*(4), 515–520.

Prodehl, C., Lipman, P. W., Pakiser, L., & Mooney, W. (1989). Crustal structure of the Rocky Mountain region. *Geophysical framework of the continental United*

States, *172*, 249–284.

Rajasekaran, S., & McMechan, G. A. (1995). Prestack processing of land data with complex topography. *Geophysics*, *60*(6), 1875–1886.

Richards, P. G., & Aki, K. (1980). *Quantitative seismology: theory and methods* (Vol. 859). Freeman San Francisco, CA.

Rondenay, S. (2009). Upper mantle imaging with array recordings of converted and scattered teleseismic waves. *Surveys in geophysics*, *30*, 377–405.

Rondenay, S., Bostock, M. G., Hearn, T. M., White, D. J., & Ellis, R. M. (2000). Lithospheric assembly and modification of the SE Canadian Shield: Abitibi-Grenville teleseismic experiment. *Journal of Geophysical Research: Solid Earth*, *105*(B6), 13735–13754.

Ruigrok, E., Campman, X., Draganov, D., & Wapenaar, K. (2010). High-resolution lithospheric imaging with seismic interferometry. *Geophysical Journal International*, *183*(1), 339–357.

Schäfer, M., Groos, L., Forbriger, T., & Bohlen, T. (2014). Line-source simulation for shallow-seismic data. Part 2: Full-waveform inversion—A synthetic 2-D case study. *Geophysical Journal International*, *198*(3), 1405–1418.

Schneider, W. A. (1978). Integral formulation for migration in two and three dimensions. *Geophysics*, *43*(1), 49–76.

Shang, X., de Hoop, M. V., & van der Hilst, R. D. (2012). Beyond receiver functions: Passive source reverse time migration and inverse scattering of converted waves. *Geophysical Research Letters*, *39*(15).

Shang, X., de Hoop, M. V., & van der Hilst, R. D. (2017). Common conversion point stacking of receiver functions versus passive-source reverse time migration and wavefield regularization. *Geophysical Journal International*, *209*(2), 923–934.

Sheehan, A. F., Shearer, P. M., Gilbert, H. J., & Dueker, K. G. (2000). Seismic migration processing of P-SV converted phases for mantle discontinuity structure beneath the Snake River Plain, western United States. *Journal of Geophysical Research: Solid Earth*, *105*(B8), 19055–19065.

Shen, W., & Ritzwoller, M. H. (2016). Crustal and uppermost mantle structure beneath the United States. *Journal of Geophysical Research: Solid Earth*, *121*(6), 4306–4342.

Shepard, D. (n.d.). A two-dimensional interpolation function for irregularly-spaced data. In *Proceedings of the 1968 23rd ACM national conference, pages=517–524, year=1968.*

Shragge, J. (2014). Reverse time migration from topography. *Geophysics*, *79*(4), S141–S152.

Sims, P. K., & Stein, H. J. (2003). Tectonic evolution of the Proterozoic Colorado province, Southern Rocky Mountains: A summary and appraisal. *Rocky Mountain Geology*, *38*(2), 183–204.

Snelson, C. M., Henstock, T. J., Keller, G. R., Miller, K. C., & Levander, A. (1998). Crustal and uppermost mantle structure along the Deep Probe seismic profile. *Rocky Mountain Geology*, *33*(2), 181–198.

Spitz, S. (1991). Seismic trace interpolation in the FX domain. *Geophysics*, *56*(6), 785–794.

Sun, R., McMechan, G. A., Hsiao, H.-H., & Chow, J. (2004). Separating P-and S-waves in prestack 3D elastic seismograms using divergence and curl. *Geophysics*, *69*(1), 286–297.

Tape, C., Liu, Q., Maggi, A., & Tromp, J. (2009). Adjoint tomography of the southern California crust. *Science*, *325*(5943), 988–992.

Tong, P. (2021). Adjoint-state traveltime tomography: Eikonal equation-based methods and application to the Anza Area in Southern California. *Journal of Geophysical Research: Solid Earth*, *126*(5), e2021JB021818.

Tong, P., Chen, C.-w., Komatitsch, D., Basini, P., & Liu, Q. (2014). High-resolution seismic array imaging based on an SEM-FK hybrid method. *Geophysical Journal International*, *197*(1), 369–395.

Tong, P., Komatitsch, D., Tseng, T.-L., Hung, S.-H., Chen, C.-W., Basini, P., & Liu, Q. (2014). A 3-D spectral-element and frequency-wave number hybrid method for high-resolution seismic array imaging. *Geophysical Research Letters*, *41*(20), 7025–7034.

Trad, D. (2009). Five-dimensional interpolation: Recovering from acquisition constraints. *Geophysics*, *74*(6), V123–V132.

Tromp, J. (2020). Seismic wavefield imaging of Earth's interior across scales. *Nature Reviews Earth & Environment*, *1*(1), 40–53.

Tromp, J., Tape, C., & Liu, Q. (2005). Seismic tomography, adjoint methods, time reversal and banana-doughnut kernels. *Geophysical Journal International*, *160* (1), 195–216.

Tyson, A. R., Morozova, E., Karlstrom, K., Dueker, K. C. S. S. K., & Foster, C. (2002). Proterozoic Farwell Mountain–Lester Mountain suture zone, northern Colorado: Subduction flip and progressive assembly of arcs. *Geology*, *30* (10), 943–946.

VanDecar, J., & Crosson, R. (1990). Determination of teleseismic relative phase arrival times using multi-channel cross-correlation and least squares. *Bulletin of the Seismological Society of America*, *80* (1), 150–169.

Vinnik, L. (1977). Detection of waves converted from P to SV in the mantle. *Physics of the Earth and planetary interiors*, *15* (1), 39–45.

Waheed, U. B., Yarman, C. E., & Flagg, G. (2015). An iterative, fast-sweeping-based eikonal solver for 3D tilted anisotropic media. *Geophysics*, *80* (3), C49–C58.

Wang, K., Jiang, C., Yang, Y., Schulte-Pelkum, V., & Liu, Q. (2020). Crustal deformation in southern California constrained by radial anisotropy from ambient noise adjoint tomography. *Geophysical Research Letters*, *47* (12), e2020GL088580.

Wang, K., Yang, Y., Jiang, C., Wang, Y., Tong, P., Liu, T., & Liu, Q. (2021). Adjoint tomography of ambient noise data and teleseismic P waves: Methodology and applications to central California. *Journal of Geophysical Research: Solid Earth*, *126* (6), e2021JB021648.

Wang, X., Zhan, Z., Zhong, M., Persaud, P., & Clayton, R. W. (2021). Urban basin structure imaging based on dense arrays and bayesian array-based coherent receiver functions. *Journal of Geophysical Research: Solid Earth*, *126* (9), e2021JB022279.

Wang, Y., Chevrot, S., Monteiller, V., Komatitsch, D., Mouthereau, F., Manatschal, G., … others (2016). The deep roots of the western Pyrenees revealed by full waveform inversion of teleseismic P waves. *Geology*, *44* (6), 475–478.

Wessel, P., Luis, J., Uieda, L., Scharroo, R., Wobbe, F., Smith, W. H., & Tian, D. (2019). The generic mapping tools version 6. *Geochemistry, Geophysics, Geosystems*, *20* (11), 5556–5564.

Whitmore, N. D. (1983). Iterative depth migration by backward time propagation.

In *Seg technical program expanded abstracts 1983* (pp. 382–385). Society of Exploration Geophysicists.

Wilson, D., & Aster, R. (2005). Seismic imaging of the crust and upper mantle using regularized joint receiver functions, frequency–wave number filtering, and multimode Kirchhoff migration. *Journal of Geophysical Research: Solid Earth*, *110*(B5).

Withers, M., Aster, R., Young, C., Beiriger, J., Harris, M., Moore, S., & Trujillo, J. (1998). A comparison of select trigger algorithms for automated global seismic phase and event detection. *Bulletin of the Seismological Society of America*, *88*(1), 95–106.

Wu, S.-M., Huang, H.-H., Lin, F.-C., Farrell, J., & Schmandt, B. (2023). Extreme seismic anisotropy indicates shallow accumulation of magmatic sills beneath Yellowstone caldera. *Earth and Planetary Science Letters*, *616*, 118244.

Xu, S., Zhang, Y., Pham, D., & Lambaré, G. (2005). Antileakage Fourier transform for seismic data regularization. *Geophysics*, *70*(4), V87–V95.

Yang, J., Huang, J., Zhu, H., McMechan, G., & Li, Z. (2022). Introduction to a Two-Way Beam Wave Method and Its Applications in Seismic Imaging. *Journal of Geophysical Research: Solid Earth*, *127*(6), e2021JB023357.

Yang, J., Zhu, H., & Lumley, D. (2020). Time-lapse imaging of coseismic ruptures for the 2019 ridgecrest earthquakes using multiazimuth backprojection with regional seismic data and a 3-D crustal velocity model. *Geophysical Research Letters*, *47*(9), e2020GL087181.

Yang, J., Zhu, H., Wang, W., Zhao, Y., & Zhang, H. (2018). Isotropic elastic reverse time migration using the phase-and amplitude-corrected vector P-and S-wavefields. *Geophysics*, *83*(6), S489–S503.

Yang, X., Pavlis, G. L., Hamburger, M. W., Marshak, S., Gilbert, H., Rupp, J., … Carpenter, N. S. (2017). Detailed crustal thickness variations beneath the Illinois Basin area: Implications for crustal evolution of the midcontinent. *Journal of Geophysical Research: Solid Earth*, *122*(8), 6323–6345.

Yi, J., Liu, Y., Yang, Z., Lu, H., He, B., & Zhang, Z. (2019). A least-squares correlation-based full traveltime inversion for shallow subsurface velocity reconstruction. *Geophysics*, *84*(4), R613–R624.

Yuan, X., Kind, R., Li, X., & Wang, R. (2006). The S receiver functions: synthetics and data example. *Geophysical Journal International*, *165*(2), 555–564.

Zhang, C., Yao, H., Liu, Q., Zhang, P., Yuan, Y. O., Feng, J., & Fang, L. (2018). Linear array ambient noise adjoint tomography reveals intense crust-mantle interactions in North China Craton. *Journal of Geophysical Research: Solid Earth*, *123*(1), 368–383.

Zhang, H., van der Lee, S., Wolin, E., Bollmann, T. A., Revenaugh, J., Wiens, D. A., ... others (2016). Distinct crustal structure of the North American Midcontinent Rift from P wave receiver functions. *Journal of Geophysical Research: Solid Earth*, *121*(11), 8136–8153.

Zhang, J., & Zheng, T. (2015). Receiver function imaging with reconstructed wavefields from sparsely scattered stations. *Seismological Research Letters*, *86*(1), 165–172.

Zhao, D., Hasegawa, A., & Horiuchi, S. (1992). Tomographic imaging of P and S wave velocity structure beneath northeastern Japan. *Journal of Geophysical Research: Solid Earth*, *97*(B13), 19909–19928.

Zhao, H. (2005). A fast sweeping method for eikonal equations. *Mathematics of computation*, *74*(250), 603–627.

Zheng, T., Zhao, L., & Zhu, R. (2008). Insight into the geodynamics of cratonic reactivation from seismic analysis of the crust-mantle boundary. *Geophysical Research Letters*, *35*(8).

Zhu, H. (2017). Elastic wavefield separation based on the Helmholtz decompositionElastic wavefield separation. *Geophysics*, *82*(2), S173–S183.

Zhu, H., Bozdağ, E., Peter, D., & Tromp, J. (2012). Structure of the European upper mantle revealed by adjoint tomography. *Nature Geoscience*, *5*(7), 493–498.

Zhu, H., Stern, R. J., & Yang, J. (2020). Seismic evidence for subduction-induced mantle flows underneath Middle America. *Nature communications*, *11*(1), 2075.

Zhu, L. (2000). Crustal structure across the San Andreas Fault, southern California from teleseismic converted waves. *Earth and Planetary Science Letters*, *179*(1), 183–190.

Table 1: Teleseismic event information for passive source RTM using the Laramie array.

Event	Original Time	Lon(°)	Lat(°)	Depth(km)
P1	2000_10_04_14_37_44	-62.5590	11.1240	110.3
P2	2000_10_05_13_39_11	-40.9580	31.7320	10
P3	2000_11_08_06_59_58	-77.8290	7.0420	17
P4	2000_11_29_10_25_13	-70.8860	-24.8690	58.2
P5	2000_12_12_05_26_45	-82.6790	6.0150	10
P6	2001_01_10_16_02_42	-153.2810	56.7744	36.4
P7	2001_01_13_17_33_32	-88.6600	13.0490	60
P8	2001_02_13_14_22_05	-88.9380	13.6710	10
P9	2001_03_24_06_27_53	132.5260	34.0830	50
P10	2001_04_09_09_00_57	-73.1090	-32.6680	11
P11	2001_04_14_23_27_26	141.7680	30.0920	10
S1	2000_10_04_16_58_44	166.9100	-15.4210	23
S2	2000_10_27_04_21_51	140.4600	26.2660	388
S3	2000_10_29_08_37_08	153.9450	-4.7660	50
S4	2000_12_21_01_01_27	151.1220	-5.7060	33
S5	2001_01_09_16_49_28	167.1700	-14.9280	103
S6	2001_04_09_09_00_57	-73.1090	-32.6680	11
S7	2001_04_14_23_27_26	141.7680	30.0920	10
S8	2001_04_28_04_49_53	-176.9370	-18.0640	351.8

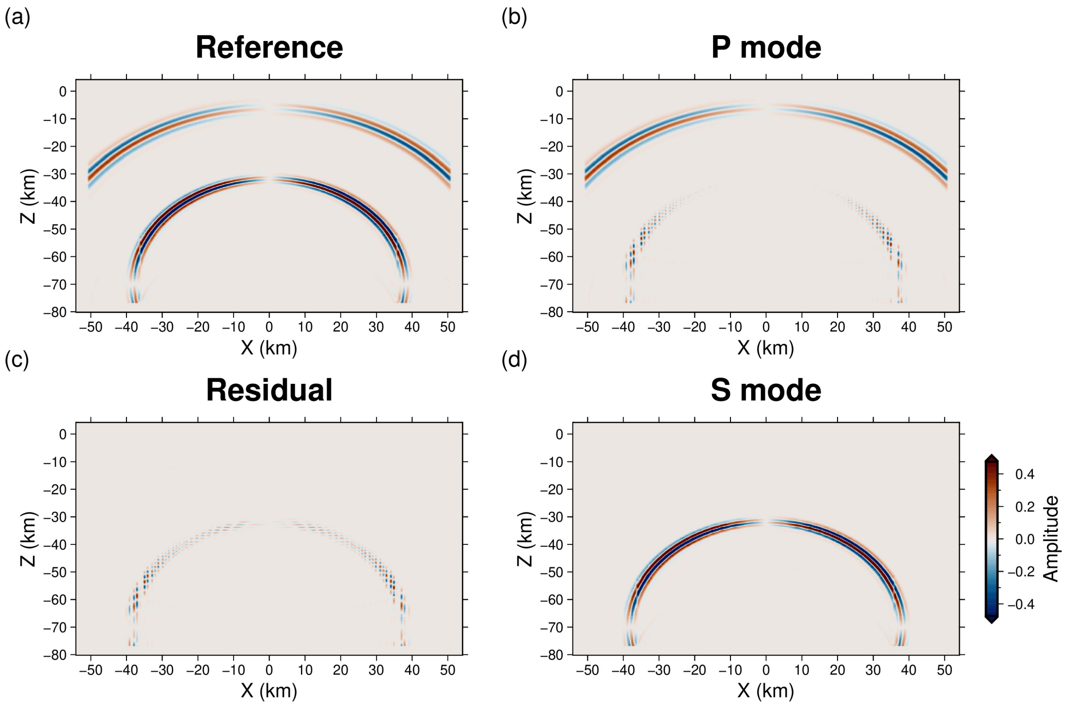

Figure 1: Strong-form solutions for wavefield decomposition based on Equation 6. Panel (a) shows the X component of the back-propagating elastic wavefield. Panels (b) and (d) represent the separated P and S wavefields, respectively. Panel (c) shows the difference between the reference (a) and the summation of strong-form decomposed P (b) and S (d) waves. The Z component has a similar phenomenon, which is not shown here.

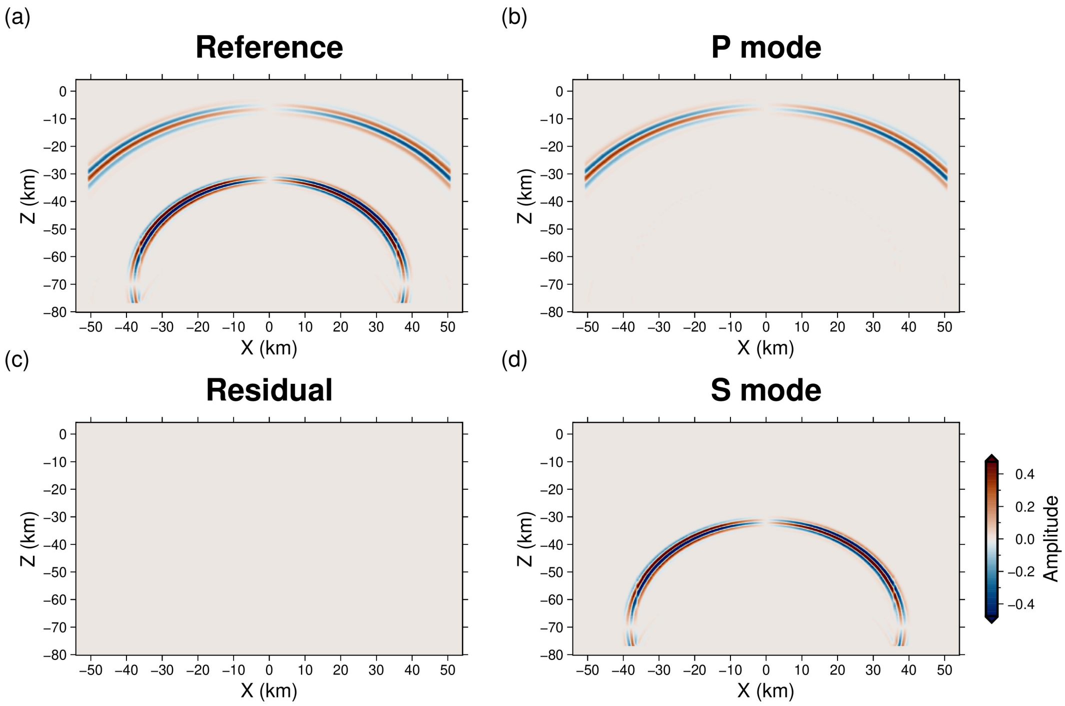

Figure 2: Same as Figure 1 but shows the decomposed wavefields based on Equations 7 and 8.

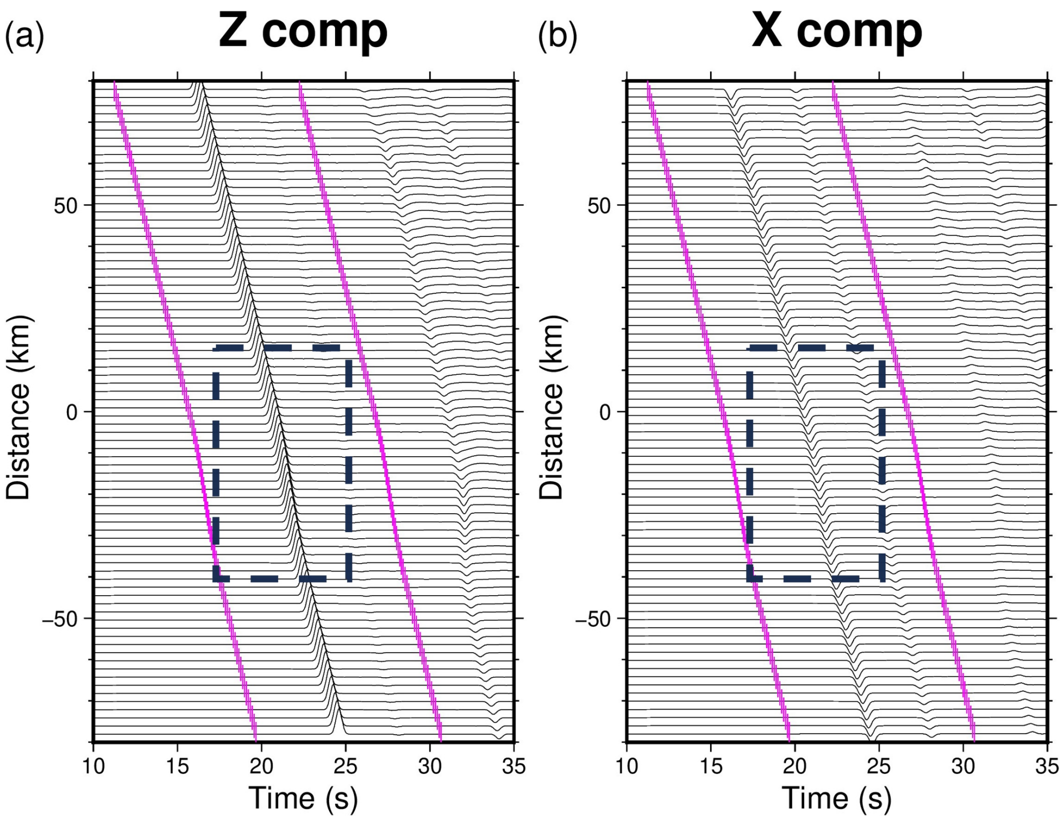

Figure 3: Synthetic teleseismic data with topographic changes in the model shown in Figure 4b. Panels (a) and (b) are Z and X component seismograms, respectively. The plane wave incident depth is 120 km, with a back azimuthal angle of 90°, and an incident angle of 27°. Therefore, X components could be considered as the radial components of teleseismic waves. The black dashed rectangle highlights the effect of topographic changes on recorded data. The magenta short lines denote the time window used to isolate waveforms for RTM.

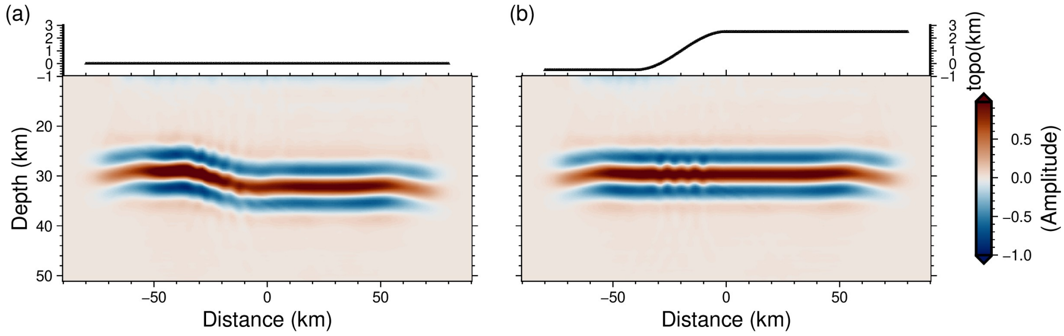

Figure 4: passive source RTM using 12 teleseismic events with incident-angles ranging from 12° to 27°. The back-azimuthal angle for the first six events is 90° and is 270° for the others. The black line on top of the image represents the station locations for injecting adjoint sources during migration. (a) Without considering the topographic variation, i.e., the stations are assumed to be at 0 km depth. (b) By considering the topographic variations, the stations are modeled at the correct elevations.

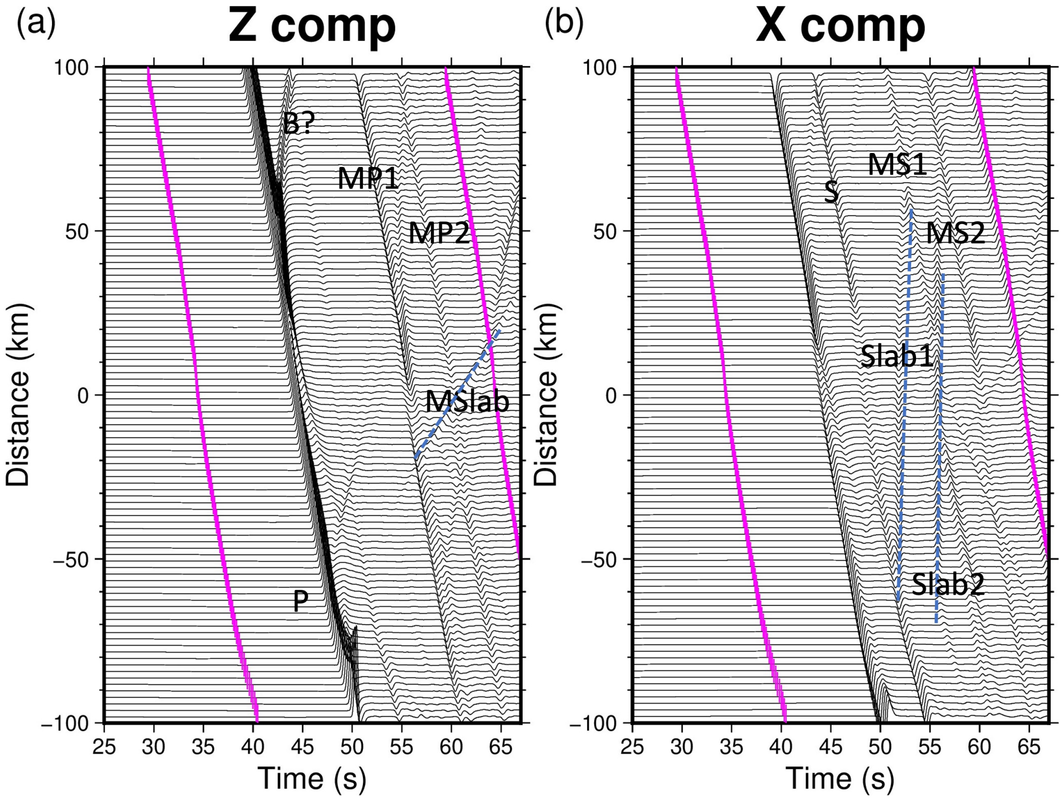

Figure 5: Synthetic Z (a) and X (b) components for the first teleseismic event with an incident angle of 27° and a back azimuthal angle of 90°. The magenta short lines denote the time window used to isolate waveforms for RTM. In panel (a), P denotes teleseismic P waves, MP1 and MP2 represent different-order P wave multiples. MSlab together with the dashed blue line, represent slab-related multiples. B is used to denote reflection artifacts due to absorbing boundary conditions. In panel (b), S denotes Ps-converted waves, MS1 and MS2 are corresponding P-multiple converted waves. Slab1 and Slab2 are slab-related Ps-converted waves.

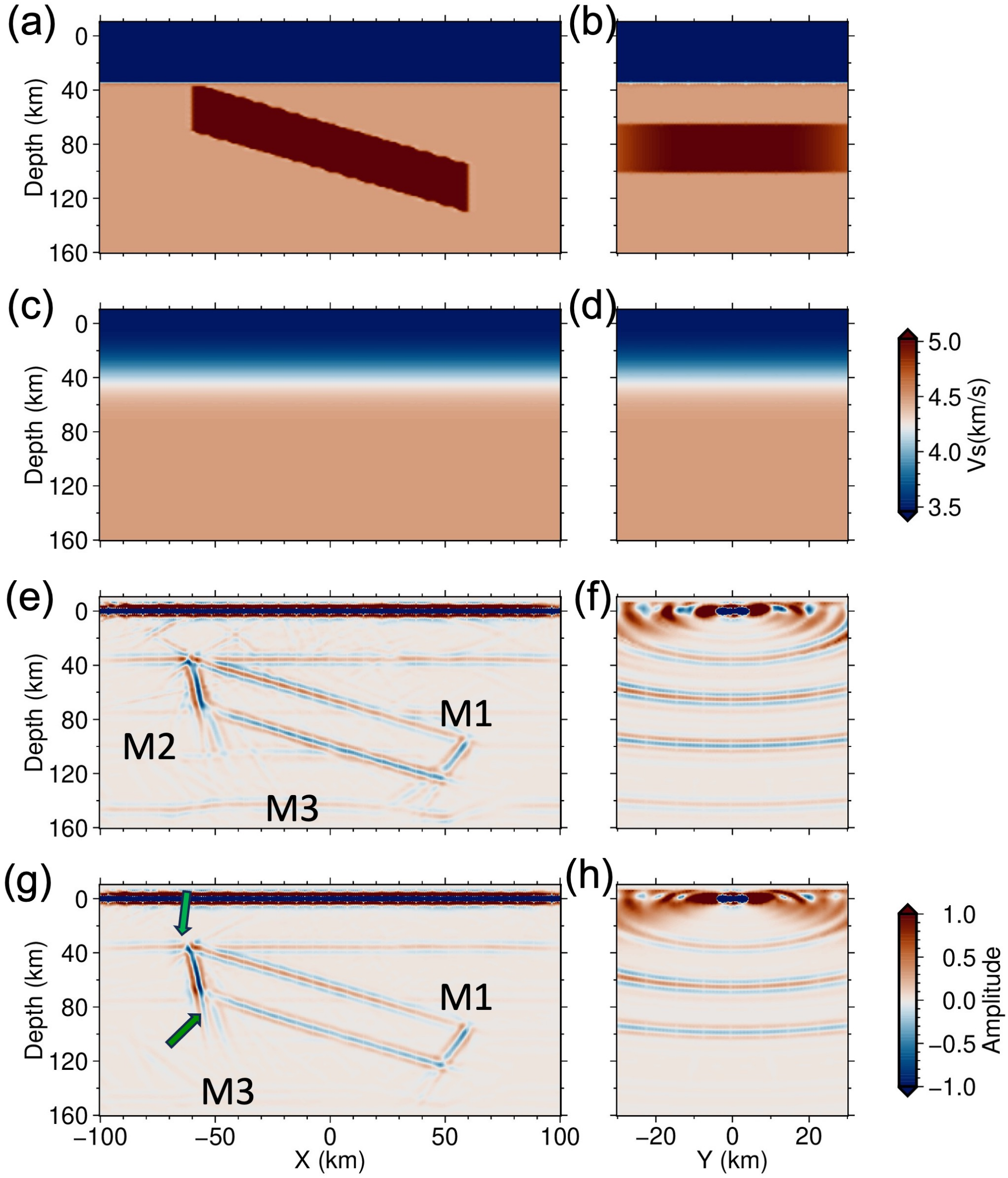

Figure 6: 3-D subducting slab imaging using 12 teleseismic events. The incident angle of the incident wavefield ranges from 12° to 27°. The back-azimuthal angle for events 1, 3, 7, 9 and 11 is 90° and 270° for the others. Panels (a) and (b) show the true velocity profile along the X (west-east) and Y (noth-source) directions for generating synthetic datasets. Panels (c) and (d) show the corresponding migration velocity along the same profiles, which is smoothed from the two-layer background model after removing the slab. Panels (e) and (f) show the stacked images from the first four teleseismic events, while panels (g) and (h) show the final image stacked over all teleseismic events. Panels (e-h) share the same color bars. M1, M2 and M3 in panels (e) and (g) represent multiple artifacts. The artifacts pointed by the green arrows are caused by strong scattering at the sharp edges of the slab.

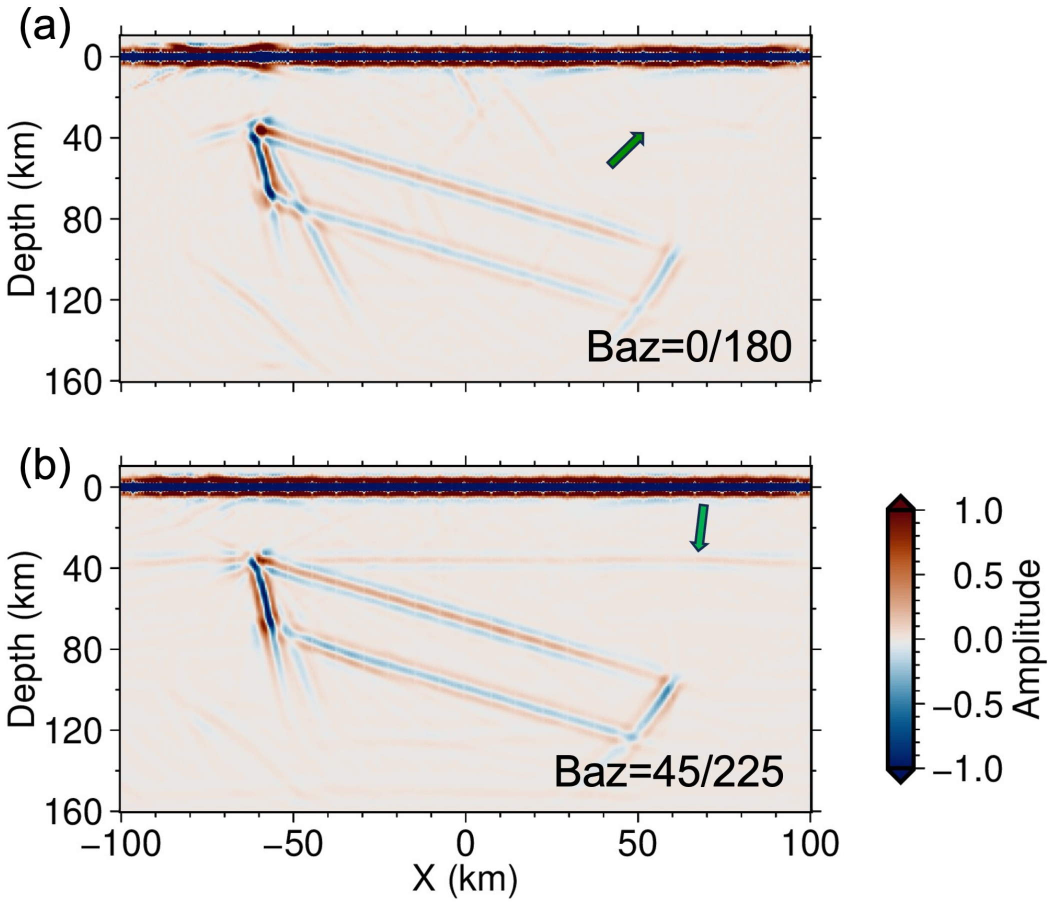

Figure 7: Similar to panel (g) in Figure 6, but the back azimuthal angles used for these two examples are 0° for events 1, 3, 7, 9 and 11, and 180° for the others (a), which are 45° and 225° in panel (b). The green arrows are used to compare imaged Moho interfaces with Figure 6.

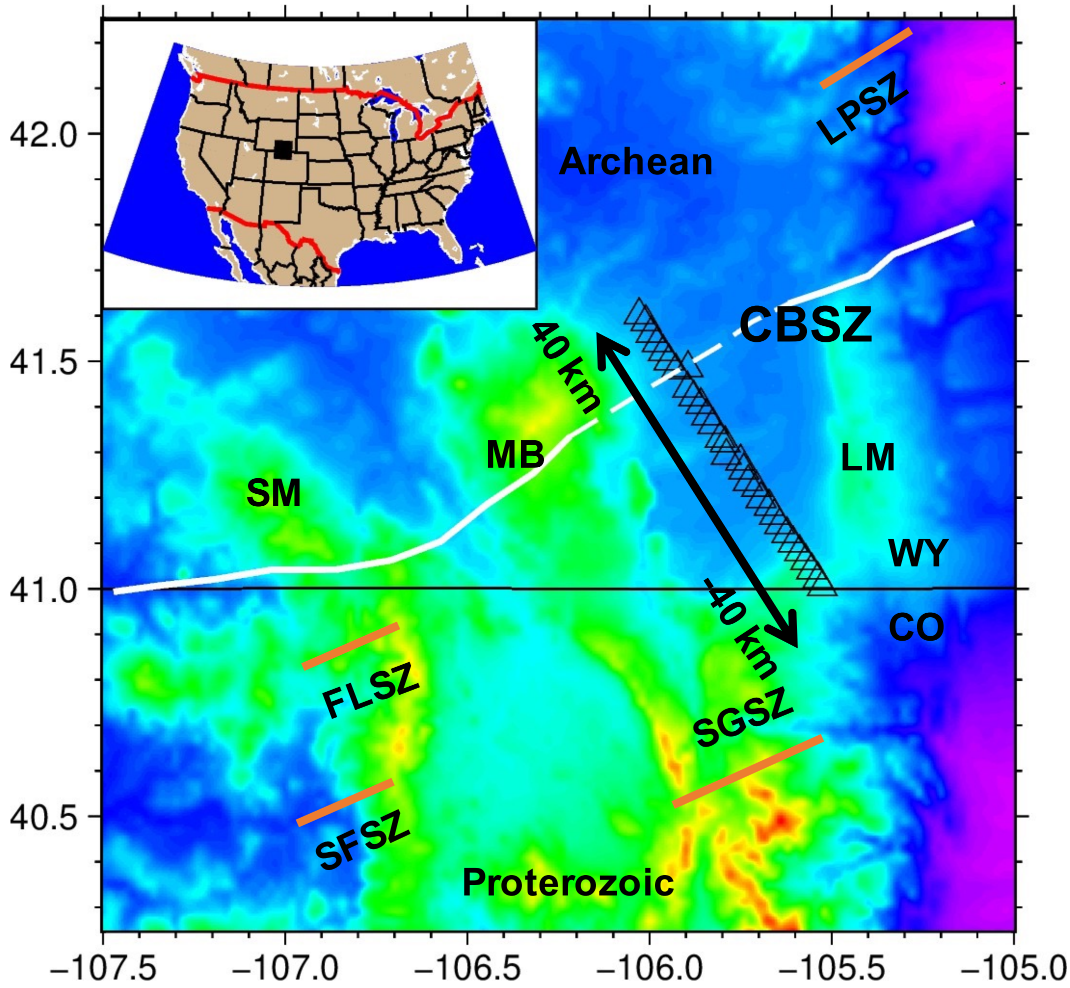

Figure 8: Geological settings of the study region after Hansen and Dueker (2009). The background shows the topography. Several shear zones: LPSZ, Laramie Peak shear zone; FLSZ, Farwell Mt. Lester Mt. suture zone; SFSZ, Soda Creek-Fish Creek shear zone; SGSZ, Skin Gulch shear zone, are denoted by orange lines to illustrate the complexity of the subsurface structures. Other geographic features: SM, Sierra Madres; MB, Medicine Bow Mountains and LM, Laramie Mountains are also labeled. The Cheyenne Belt suture (CB) is denoted by the white line, dashed where it is inferred. WY and CO denotes Wyoming and Colorado, respectively. The black rectangle in the upper-left inset map indicates the location of our study region in North America.

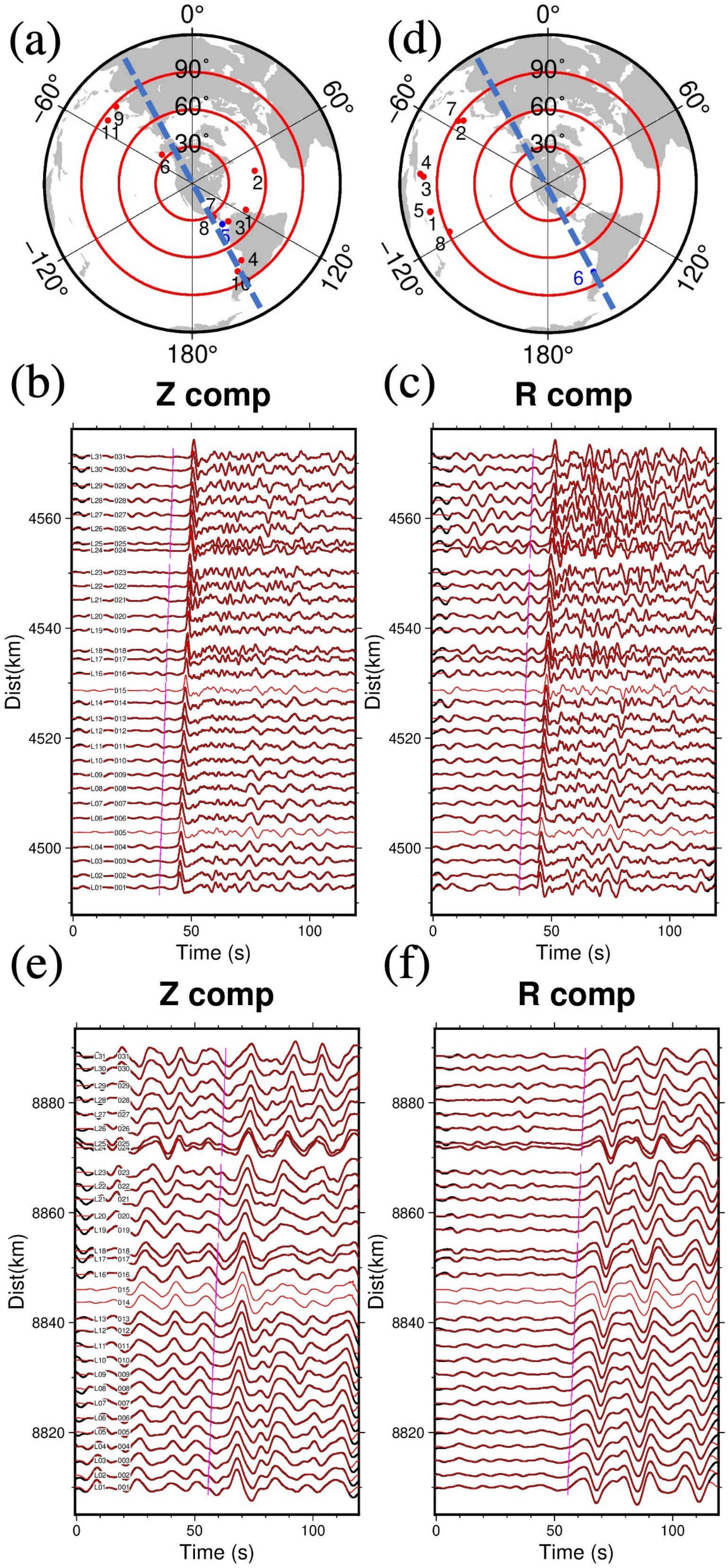

Figure 9: Caption next page.

Figure 9: Telseismic events and data used for migration. Red dots in Panels (a) and (d) represent the distributions of teleseismic P and S events. The light blue dashed line indicates the direction of the Laramie array. Panels (b) and (c) show the vertical (Z) and radial (R) components of the 5th (the blue dot in panel a) teleseismic P events recorded by the Laramie array. The background black solid lines denote the selected high-quality data (some traces are removed due to low signal-to-noise ratio), while the red solid lines represent the 2-D cubic-spline interpolated data at each station. Panels (e) and (f) represent the vertical and radial components of the 6th teleseismic S events. The magenta lines overlaying the seismograms denote either the onsets of P or S waves.

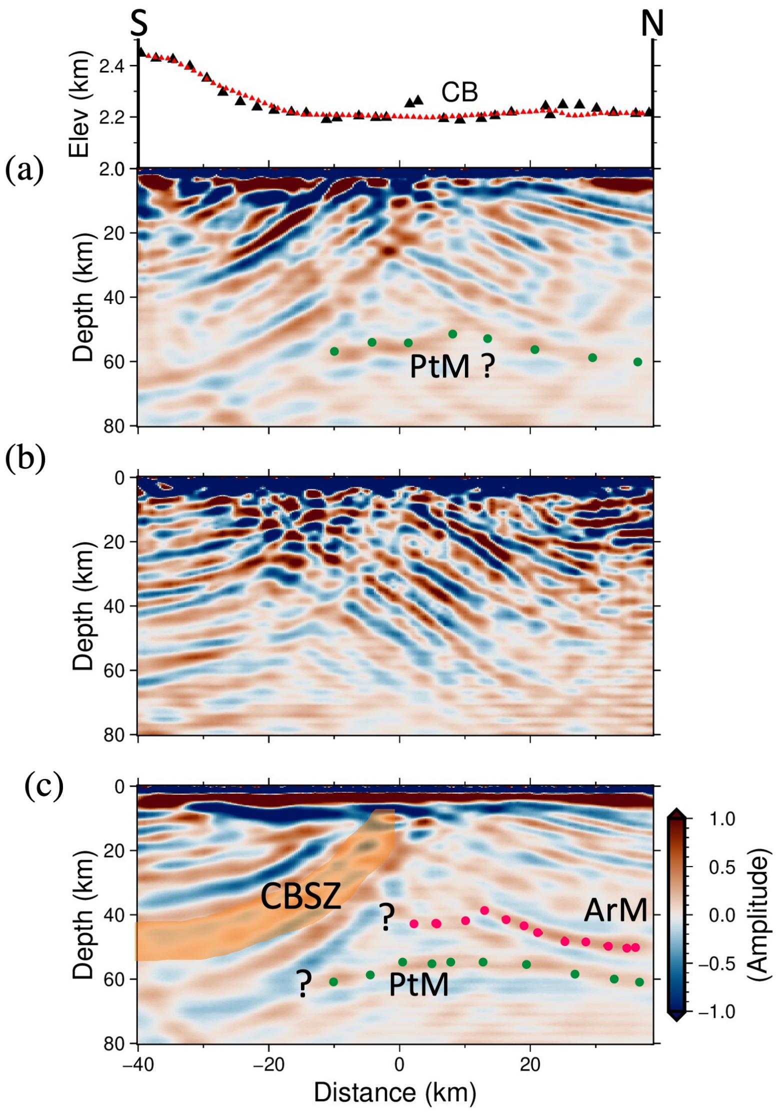

Figure 10: The passive source RTM image beneath the Laramie array. On the top of the figure, we show the elevation of raw (back triangles) and interpolated (red triangles) stations. CB represents the inferred CBSZ location on the surface. Panels (a) and (b) show the images obtained using teleseismic P and S events, respectively. Panel (c) shows the image obtained using interpolated teleseismic P events. The orange belt indicates the interpreted CBSZ. The magenta and dark green dots indicate the interpreted Archean Moho (ArM) and Proterozoic Moho (PtM).

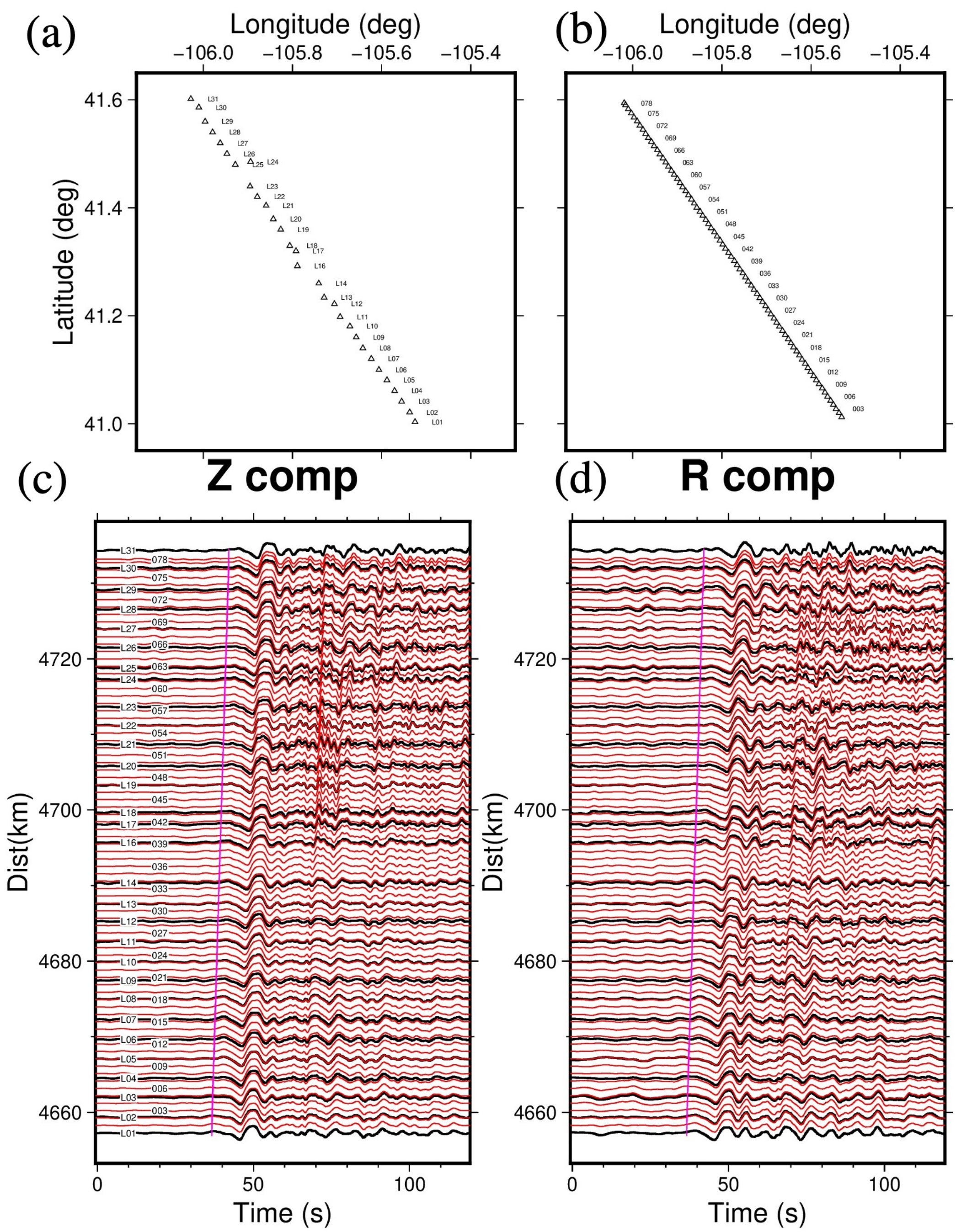

Figure 11: Regularization of the recorded teleseismic data to a fine grid. Panels (a) and (b) compare the raw and interpolation station locations. The interpolated station locations are obtained with GMT projection between the first (L01) and last station (L31) positions of the Laramie array along the great circle for every 1.0 km, which is not on a straight line after the UTM projection. Panels (c) and (d) show comparisons of the raw data (black) and interpolated seismograms (red) for vertical (Z) and radial (R) components, respectively.

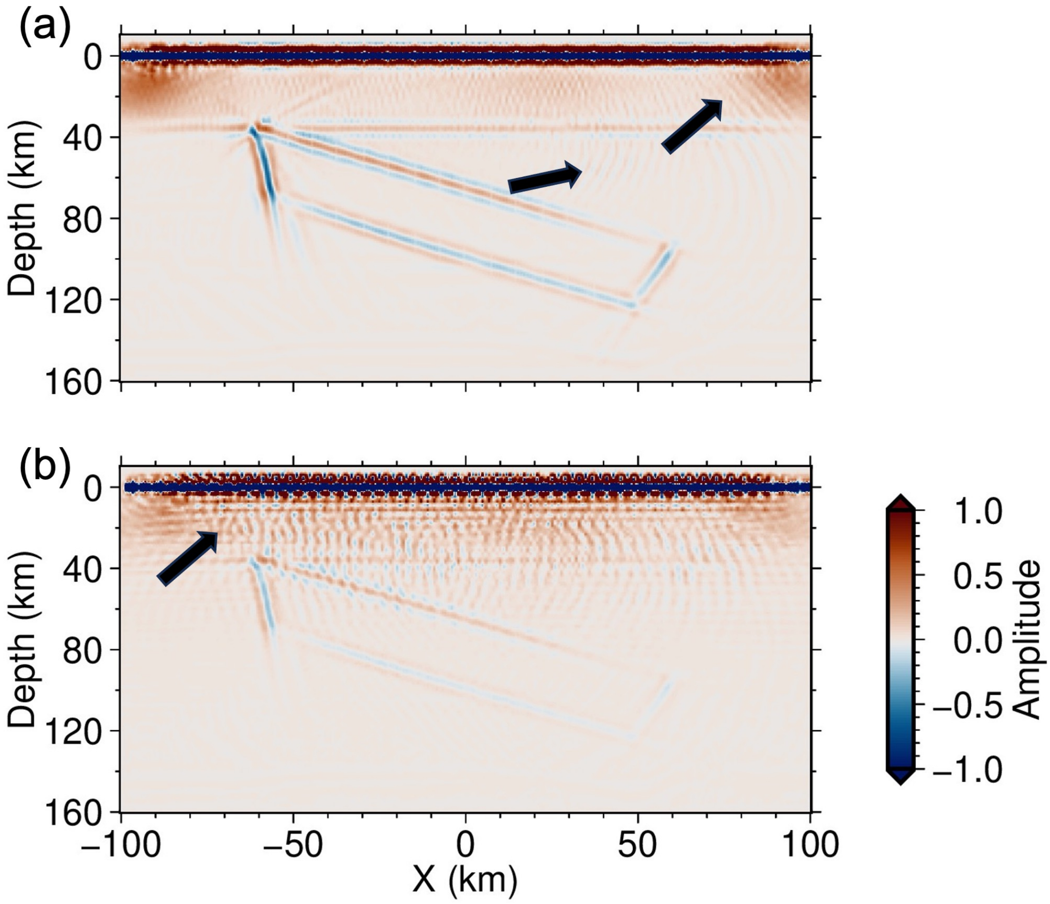

Figure 12: Imaging with sparse station spacing. The imaging parameters are the same as panel (g) in Figure 6 except that the station spacing is 2 km and 4 km for panels (a) and (b), respectively. The aliasing artifacts are illustrated by black arrows.

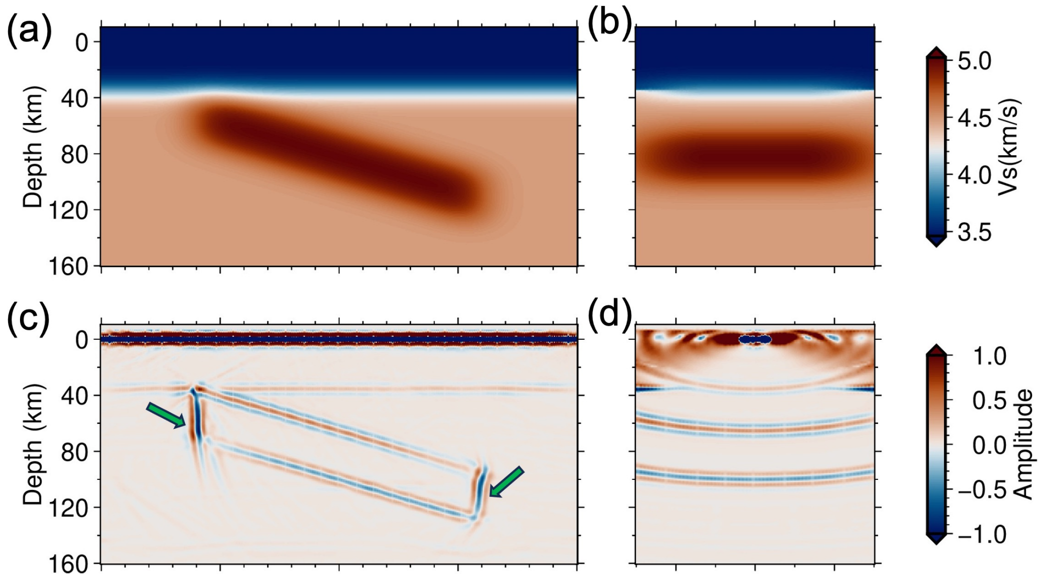

Figure 13: Imaging with a more accurate background migration velocity model. Panels (a) and (b) show the migration velocity profiles along the X (west-east) and Y (noth-source) directions. Panels (c) and (d) show the corresponding RTM images. The green arrows are used to highlight the improvement in imaging of the slab boundaries compared to panel (g) in Figure 6.

Supporting Information for "Passive source reverse time migration based on the spectral element method"

Bin He[1], Yu Chen[1], David Lumley[1,2], Qinya Liu[3,4], Nozomu Takeuchi[5],

Hitoshi Kawakatsu[5], and Hejun Zhu[1,2]

[1]Department of Geosciences, The University of Texas at Dallas, Richardson, TX 75080, USA

[2]Department of Physics, The University of Texas at Dallas, Richardson, TX 75080, USA

[3]Department of Physics, University of Toronto, Toronto M5S 1A7, Canada

[4]Department of Earth Sciences, University of Toronto, Toronto M5S 3B1, Canada

[5]Earthquake Research Institute, University of Tokyo, Tokyo 1130032, Japan

Contents of this file

Introduction

In this supporting information, we show how to get the weak-form solutions for wavefield decomposition. If you are familiar with the spectral element method, please go to section 3 directly. For detailed deviations, please refer to Fichtner (2010).

Text S1. Notes for understanding the weak solutions

1. Weak Solutions for the elastic wave-equation

The strong displacement-stress variant of the equations of motion:

$$\rho(\mathbf{x})\ddot{\mathbf{u}}(\mathbf{x},t) - \nabla \cdot \sigma(\mathbf{x},t) = \mathbf{f}(\mathbf{x},t) \quad , \tag{1}$$

$$\sigma(\mathbf{x},t) = \mathbf{C}(\mathbf{x}) : \nabla\mathbf{u}(\mathbf{x},t) \quad , \tag{2}$$

subject to the boundary and initial conditions

$$\mathbf{n} \cdot \sigma|_{\mathbf{x}\in\partial G} = 0 \quad , \quad \mathbf{u}|_{t=0} = \dot{\mathbf{u}}|_{t=0} = 0 \quad . \tag{3}$$

For the moment we disregard dissipation, i.e., the time dependence of the elastic tensor $\mathbf{C}$. Multiply Eq.(1) by an arbitrary, differentiable, time-independent test function $\mathbf{w}$ and integrating over G gives

$$\int_G \rho\mathbf{w} \cdot \ddot{\mathbf{u}} d^3\mathbf{x} - \int_G \mathbf{w} \cdot (\nabla \cdot \sigma) d^3\mathbf{x} = \int_G \mathbf{w} \cdot \mathbf{f} d^3\mathbf{x} \quad . \tag{4}$$

Invoking the identity

$$\mathbf{w} \cdot (\nabla \cdot \sigma) = \nabla \cdot (\mathbf{w} \cdot \sigma) - \nabla\mathbf{w} : \sigma \quad . \tag{5}$$

Poof:

$$\nabla \cdot (\mathbf{w} \cdot \sigma) = \partial_i(w_j\sigma_{ij}) = (\partial_i w_j)\sigma_{ij} + w_j(\partial_i\sigma_{ij}) = \nabla\mathbf{w} : \sigma + \mathbf{w} \cdot (\nabla \cdot \sigma) \quad .$$

Together with Gauss's theorem, yields,

$$\int_G \rho\mathbf{w} \cdot \ddot{\mathbf{u}} d^3\mathbf{x} - \int_{\partial G} \mathbf{w} \cdot \sigma \cdot \mathbf{n} d^2\mathbf{x} + \int_G \nabla\mathbf{w} : \sigma d^3\mathbf{x} = \int_G \mathbf{w} \cdot \mathbf{f} d^3\mathbf{x} \quad . \tag{6}$$

Upon inserting the free surface boundary condition, Eq. (6) condenses to

$$\int_G \rho\mathbf{w} \cdot \ddot{\mathbf{u}} d^3\mathbf{x} + \int_G \nabla\mathbf{w} : \sigma d^3\mathbf{x} = \int_G \mathbf{w} \cdot \mathbf{f} d^3\mathbf{x} \quad . \tag{7}$$

Finding a weak solution to the equations of motion means finding a displacement field $\mathbf{u}$ that satisfies the integral relation Eq. (7) and

$$\int_G \mathbf{w} \cdot \sigma d^3\mathbf{x} = \int_G \mathbf{w} \cdot (\mathbf{C} : \nabla \mathbf{u}) d^3\mathbf{x} \quad . \tag{8}$$

for any test function $\mathbf{w}$ and subject to the initial conditions.

2. Discretisation of the Equations of Motion

By using the Galerkin method, we approximate the p-component u_p of the displacement field $\mathbf{u}$ by a superposition of basis functions

$$\psi_{ijk}(\mathbf{x}) = \psi_{ijk}(x_1, x_2, x_3) \quad , \tag{9}$$

weighted by expansion coefficients u_p^{ijk}:

$$u_p(\mathbf{x}, t) \approx \bar{u}_p(\mathbf{x}, t) = \sum_{i,j,k=1}^{N+1} u_p^{ijk}(t) \psi_{ijk}(\mathbf{x}) \quad . \tag{10}$$

The corresponding approximation of the stress tensor components σ_{pq} is

$$\sigma_{pq}(\mathbf{x}, t) \approx \bar{\sigma}_{pq}(\mathbf{x}, t) = \sum_{i,j,k=1}^{N+1} \sigma_{pq}^{ijk}(t) \psi_{ijk}(\mathbf{x}) \quad . \tag{11}$$

To find a weak solution in the Galerkin sense, we replace the exact weak formulation forms from Eqs. (7) and (8) by the requirement that approximations $\bar{\mathbf{u}}$ and $\bar{\sigma}$ satisfy

$$\int_G \rho \mathbf{w} \cdot \ddot{\bar{\mathbf{u}}} d^3\mathbf{x} + \int_G \nabla \mathbf{w} : \bar{\sigma} d^3\mathbf{x} = \int_G \mathbf{w} \cdot \mathbf{f} d^3\mathbf{x} \quad ,$$
$$\int_G \mathbf{w} \cdot \bar{\sigma} d^3\mathbf{x} = \int_G \mathbf{w} \cdot (\mathbf{C} : \nabla \bar{\mathbf{u}}) d^3\mathbf{x} \quad ,$$

for any test function, $w_{ijk}^p = \psi_{ijk}\mathbf{e}_p$ in the form of

$$\int_{G_e} \rho \psi_{ijk}\mathbf{e}_p \cdot \ddot{\bar{\mathbf{u}}} d^3\mathbf{x} + \int_{G_e} \nabla(\psi_{ijk}\mathbf{e}_p) : \bar{\sigma} d^3\mathbf{x} = \int_{G_e} \psi_{ijk}\mathbf{e}_p \cdot \mathbf{f} d^3\mathbf{x} \tag{12}$$
$$\int_{G_e} \psi_{ijk}\mathbf{e}_p \cdot \bar{\sigma} d^3\mathbf{x} = \int_{G_e} \psi_{ijk}\mathbf{e}_p \cdot (\mathbf{C} : \nabla \bar{\mathbf{u}}) d^3\mathbf{x} \quad . \tag{13}$$

Here Eqs. (12) and (13) already assume that u_p and σ_{pq} are considered inside an element $G_e \subset \mathbb{R}^3$,where they can be represented by $(N+1)^3$ basis functions.

For the first term on the left-hand side of Eq. (12), we find

$$\begin{aligned} \mathbb{F}_{qrs}(\rho \ddot{u}_p) &:= \int_{G_e} \rho \psi_{qrs} \mathbf{e}_p \cdot \ddot{\mathbf{u}} d^3\mathbf{x} = \sum_{i,j,k=1}^{N+1} \int_{G_e} \rho \psi_{qrs} \ddot{u}_p^{ijk} \psi_{ijk} d^3\mathbf{x} \\ &= \sum_{i,j,k=1}^{N+1} \int_{\Lambda} \rho[\mathbf{x}(\xi)] \psi_{qrs}[\mathbf{x}(\xi)] \ddot{u}_p^{ijk}(t) \psi_{ijk}[\mathbf{x}(\xi)] J(\xi) d^3\xi \quad . \end{aligned} \tag{14}$$

For the basis function $\psi_{ijk}[\mathbf{x}(\xi)]$ we chose the product of three Lagrange polynomial collocated at the GLL points:

$$\psi_{ijk}[\mathbf{x}(\xi)] = l_i(\xi_1) l_j(\xi_2) l_k(\xi_3) \quad , \tag{15}$$

then we have

$$\mathbb{F}_{qrs}(\rho \ddot{u}_p) = \sum_{i,j,k=1}^{N+1} \int_{\Lambda} \rho(\xi) l_q(\xi_1) l_r(\xi_2) l_s(\xi_3) \ddot{u}_p^{ijk}(t) l_i(\xi_1) l_j(\xi_2) l_k(\xi_3) J(\xi^{qrs}) d^3\xi \quad . \tag{16}$$

Apply the GLL quadrature rule to Eq. (16) yields the following simple expression:

$$\begin{aligned} \mathbb{F}_{qrs}(\rho \ddot{u}_p) &= \sum_{i,j,k=1}^{N+1} \sum_{f,g,h=1}^{N+1} w_f(\xi_1) w_g(\xi_2) w_h(\xi_3) \\ &\cdot \rho(\xi^{fgh}) \ddot{u}_p^{ijk}(t) J(\xi^{gh}) l_q^f(\xi_1) l_r^g(\xi_2) l_s^h(\xi_3) l_i^f(\xi_1) l_j^g(\xi_2) l_k^h(\xi_3) \\ &= \rho(\xi^{qrs}) w_q(\xi_1) w_r(\xi_2) w_s(\xi_3) \ddot{u}_p^{qrs}(t) J(\xi^{qrs}) \quad , \end{aligned} \tag{17}$$

here, J represents the Jacobin matrix. For the second term on the left-hand side of Eq. (12), we need to know that, according to the proof for Eq. (5), $\nabla \mathbf{w} : \sigma$ actually represents a double inner product for two matrices, which is in the form of $\mathbf{A} : \mathbf{B} = \sum_{i,j} A_{ij} B_{ij}$.

Therefore, $\nabla \mathbf{w} : \sigma = \sum_{i,j=1}^{3} \partial_j w_i \sigma_{i,j}$ then we have

$$
\begin{aligned}
\mathbb{F}_{qrs}(\nabla : \sigma)_p &:= \int_{G_e} \nabla(\psi_{qrs}\mathbf{e}_p) : \bar{\sigma} d^3\mathbf{x} \\
&= \int_{G_e} \sum_{m,n=1}^{3} [\frac{\partial_n(\psi_{qrs}e_p)}{dx_m}] : \bar{\sigma} d^3\mathbf{x} \\
&= \int_{G_e} \sum_{m,n=1}^{3} [\frac{\partial(\psi_{qrs}e_p^n)}{dx_m}] \bar{\sigma}_{mn} d^3\mathbf{x} \\
&= \int_{G_e} \sum_{m,n=1}^{3} \frac{\partial(\psi_{qrs})}{dx_m} \delta_n^p \bar{\sigma}_{mn} d^3\mathbf{x} \\
&= \int_{G_e} \sum_{m=1}^{3} \frac{\partial(\psi_{qrs})}{dx_m} \bar{\sigma}_{mp} d^3\mathbf{x} \\
&= \int_{\Lambda} \sum_{m,n=1}^{3} \frac{\partial(\psi_{qrs})}{d\xi_n} \frac{d\xi_n}{dx_m}(\xi) \bar{\sigma}_{mp}(\xi) J(\xi) d^3\xi \\
&= \int_{\Lambda} \sum_{m,n=1}^{3} \frac{\partial[l_q(\xi_1) l_s(\xi_2)]}{d\xi_n} \frac{d\xi_n}{dx_m} \bar{\sigma}_{mp}[x(\xi)] J[x(\xi)] d^3\xi \\
&= \int_{\Lambda} \sum_{m}^{3} \dot{l}_q(\xi_1) l_r(\xi_2) l_s(\xi_3) \frac{d\xi_1}{dx_m} \bar{\sigma}_{mp}(\xi) J(\xi) d^3\xi \\
&+ \int_{\Lambda} \sum_{m}^{3} l_q(\xi_1) \dot{l}_r(\xi_2) l_s(\xi_3) \frac{d\xi_2}{dx_m} \bar{\sigma}_{mp}(\xi) J(\xi) d^3\xi \\
&+ \int_{\Lambda} \sum_{m}^{3} l_q(\xi_1) l_r(\xi_2) \dot{l}_s(\xi_3) \frac{d\xi_3}{dx_m} \bar{\sigma}_{mp}(\xi) J(\xi) d^3\xi \quad .
\end{aligned}
\tag{18}
$$

Now if we bring the GLL quadrature rule to Eq. (19), we have

$$
\begin{aligned}
\mathbb{F}_{qrs}(\nabla:\sigma)_p = & \sum_{i,j,k=1}^{N+1}\sum_{m=1}^{3} w_q w_r w_s \dot{l}_q^i(\xi_1) l_r^j(\xi_2) l_s^k(\xi_3) \frac{d\xi_1}{dx_m}(\xi^{ijk})\bar{\sigma}_{mp}(\xi^{ijk})J(\xi^{ijk})d^3\xi \\
& + \sum_{i,j,k=1}^{N+1}\sum_{m=1}^{3} w_q w_r w_s l_q^i(\xi_1) \dot{l}_r^j(\xi_2) l_s^k(\xi_3) \frac{d\xi_2}{dx_m}(\xi^{ijk})\bar{\sigma}_{mp}(\xi^{ijk})J(\xi^{ijk})d^3\xi \\
& + \sum_{i,j,k=1}^{N+1}\sum_{m=1}^{3} w_q w_r w_s l_q(\xi_1) l_r(\xi_2) \dot{l}_s(\xi_3) \frac{d\xi_3}{dx_m}(\xi^{ijk})\bar{\sigma}_{mp}(\xi^{ijk})J(\xi^{ijk})d^3\xi \\
& = \sum_{m=1}^{3}\sum_{i=1}^{N+1} w_q w_r w_s \dot{l}_q^i(\xi_1) \frac{d\xi_1}{dx_m}(\xi^{irs})\bar{\sigma}_{mp}(\xi^{irs})J(\xi^{irs})d^3\xi \\
& + \sum_{m=1}^{3}\sum_{i=1}^{N+1} w_q w_r w_s \dot{l}_r^i(\xi_2) \frac{d\xi_2}{dx_m}(\xi^{qis})\bar{\sigma}_{mp}(\xi^{qis})J(\xi^{qis})d^3\xi \\
& + \sum_{m=1}^{3}\sum_{i=1}^{N+1} w_q w_r w_s \dot{l}_s^i(\xi_3) \frac{d\xi_3}{dx_m}(\xi^{qri})\bar{\sigma}_{mp}(\xi^{qri})J(\xi^{qri})d^3\xi \quad .
\end{aligned}
\tag{19}
$$

Repeating the above procedure for the source term in Eq. (12)gives

$$
\mathbb{F}_{qrs}(\mathbf{f}_p) := w_q w_r w_s f_p(\xi^{qrs})J(\xi^{qrs}) \tag{20}
$$

It remains to consider the approximate weak form of the constitutive relation as specified by Eq. (13). For the left-hand term:

$$
\begin{aligned}
\mathbb{F}_{qrs}(\sigma_{mn}) &:= \int_{G_e} \psi_{qrs}(\mathbf{e}_m\cdot\bar{\sigma})_n d^3\mathbf{x} \\
&= \int_{G_e} \psi_{qrs} \sum_{i,j,k=1}^{N+1} \sigma_{mn}^{ijk}(t)\psi_{ijk}(\mathbf{x})d^3\mathbf{x} \\
&= \int_{\Lambda} \psi_{qrs} \sum_{i,j,k=1}^{N+1} \sigma_{mn}^{ijk}(t)\psi_{ijk}(\xi)J(\xi)d^3\xi \\
&= \int_{\Lambda} \sum_{i,j,k=1}^{N+1} \sigma_{mn}^{ijk}(t) l_q(\xi_1) l_r(\xi_2) l_s(\xi_3) l_i(\xi_1) l_j(\xi_2) l_k(\xi_3) J(\xi) d^3\xi \\
&= w_p(\xi_1) w_r(\xi_2) w_s(\xi_3)\sigma_{mn}^{qrs}(t)J(\xi^{qrs}) \quad ,
\end{aligned}
\tag{21}
$$

while the right-hand term could be simplified by

$$
\begin{aligned}
\mathbb{F}_{qrs}(\mathbf{C}:\nabla\mathbf{u})_{mn} &:= \int_{G_e}[\psi_{qrs}\mathbf{e}_m\cdot(\mathbf{C}:\nabla\bar{\mathbf{u}})]_n d^3\mathbf{x} \\
&= \int_{G_e}\psi_{qrs}\sum_{a,b=1}^{3}C_{mnab}(\nabla\bar{\mathbf{u}})_{ab}d^3\mathbf{x} \\
&= \int_{G_e}\sum_{a,b=1}^{3}\psi_{qrs}C_{mnab}\sum_{i,j,k=1}^{N+1}\frac{\partial\psi_{ijk}}{dx_a}u_b^{ijk}d^3\mathbf{x} \\
&= \int_{\Lambda}\sum_{a,b=1}^{3}\sum_{i,j,k=1}^{N+1}\psi_{qrs}C_{mnab}\frac{\partial(l_i(\xi_1)l_j(\xi_2)l_k(\xi_3))}{d\xi_1}\frac{d\xi_1}{dx_a}u_b^{ijk}Jd^3\xi \\
&+ \int_{\Lambda}\sum_{a,b=1}^{3}\sum_{i,j,k=1}^{N+1}\psi_{qrs}C_{mnab}\frac{\partial(l_i(\xi_1)l_j(\xi_2)l_k(\xi_3))}{d\xi_2}\frac{d\xi_2}{dx_a}u_b^{ijk}Jd^3\xi \\
&+ \int_{\Lambda}\sum_{a,b=1}^{3}\sum_{i,j,k=1}^{N+1}\psi_{qrs}C_{mnab}\frac{\partial(l_i(\xi_1)l_j(\xi_2)l_k(\xi_3))}{d\xi_3}\frac{d\xi_3}{dx_a}u_b^{ijk}Jd^3\xi \\
&= \int_{\Lambda}\sum_{a,b=1}^{3}\sum_{i,j,k=1}^{N+1}[l_q(\xi_1)l_s(\xi_2)]C_{mnab}\dot{l}_i(\xi_1)l_j(\xi_2)l_k(\xi_3)\frac{d\xi_1}{dx_a}[\xi]u_b^{ijk}J(\xi)d^3\xi \\
&+ \int_{\Lambda}\sum_{a,b=1}^{3}\sum_{i,j,k=1}^{N+1}[l_q(\xi_1)l_r(\xi_2)l_s(\xi_3)]C_{mnab}l_i(\xi_1)\dot{l}_j(\xi_2)l_k(\xi_3)\frac{d\xi_2}{dx_a}[\xi]u_b^{ijk}J(\xi)d^3\xi \\
&+ \int_{\Lambda}\sum_{a,b=1}^{3}\sum_{i,j,k=1}^{N+1}[l_q(\xi_1)l_r(\xi_2)l_s(\xi_3)]C_{mnab}l_i(\xi_1)l_j(\xi_2)\dot{l}_k(\xi_3)\frac{d\xi_2}{dx_a}[\xi]u_b^{ijk}J(\xi)d^3\xi \\
&= \sum_{f,g,h=1}^{N+1}w_fw_gw_h\sum_{a,b=1}^{3}\sum_{i,j,k=1}^{N+1}[l_q^f(\xi_1)l_r^g(\xi_2)l_s^h(\xi_3)]C_{mnab}\dot{l}_i^f(\xi_1)l_j^g(\xi_2)l_j^h(\xi_3)\frac{d\xi_1}{dx_a}(\xi^{fgh})u_b^{ijk}J(\xi^{fgh}) \\
&+ \sum_{f,g,h=1}^{N+1}w_fw_gw_h\sum_{a,b=1}^{3}\sum_{i,j,k=1}^{N+1}[l_q^f(\xi_1)l_r^g(\xi_2)l_s^h(\xi_3)]C_{mnab}l_i^f(\xi_1)\dot{l}_j^g(\xi_2)l_j^h(\xi_3)\frac{d\xi_1}{dx_a}(\xi^{fgh})u_b^{ijk}J(\xi^{fgh}) \\
&\sum_{f,g,h=1}^{N+1}w_fw_gw_h\sum_{a,b=1}^{3}\sum_{i,j,k=1}^{N+1}[l_q^f(\xi_1)l_r^g(\xi_2)l_s^h(\xi_3)]C_{mnab}l_i^f(\xi_1)l_j^g(\xi_2)\dot{l}_j^h(\xi_3)\frac{d\xi_1}{dx_a}(\xi^{fgh})u_b^{ijk}J(\xi^{fgh}) \\
&= w_qw_rw_s\sum_{a,b=1}^{3}\sum_{i=1}^{N+1}C_{mnab}\dot{l}_i^q(\xi_1)\frac{d\xi_1}{dx_a}(\xi^{qrs})u_b^{iqs}J(\xi^{qrs}) \\
&+ w_qw_rw_s\sum_{a,b=1}^{3}\sum_{i=1}^{N+1}C_{mnab}\dot{l}_i^r(\xi_2)\frac{d\xi_2}{dx_a}(\xi^{qrs})u_b^{qik}J(\xi^{qrs}) \\
&+ w_qw_rw_s\sum_{a,b=1}^{3}\sum_{i=1}^{N+1}C_{mnab}\dot{l}_i^s(\xi_2)\frac{d\xi_2}{dx_a}(\xi^{qrs})u_b^{qri}J(\xi^{qrs}) \quad .
\end{aligned}
\tag{22}
$$

Let's see if the above equation is right or not (with the 2D case for simple) with the Voigt notation for the tensor index as:

$$\begin{array}{ccccccccc} ij & = & 11 & 22 & 33 & 23,32 & 13,31 & 12,21 \\ \Downarrow & = & \Downarrow & \Downarrow & \Downarrow & \Downarrow & \Downarrow & \Downarrow \\ \alpha & = & 1 & 2 & 3 & 4 & 5 & 6 \end{array} \tag{23}$$

$$C_{ijkl} \Rightarrow C_{\alpha\beta} = \begin{bmatrix} C_{11} & C_{12} & C_{13} & C_{14} & C_{15} & C_{16} \\ C_{12} & C_{22} & C_{23} & C_{24} & C_{25} & C_{26} \\ C_{13} & C_{23} & C_{33} & C_{34} & C_{35} & C_{36} \\ C_{14} & C_{24} & C_{34} & C_{44} & C_{45} & C_{46} \\ C_{15} & C_{25} & C_{35} & C_{45} & C_{55} & C_{56} \\ C_{16} & C_{26} & C_{36} & C_{46} & C_{56} & C_{66} \end{bmatrix} \tag{24}$$

For the isotropic case, it only has 2 independent elements:

$$C_{\alpha\beta} = \begin{bmatrix} K+4\mu/3 & K-2\mu/3 & K-2\mu/3 & 0 & 0 & 0 \\ K-2\mu/3 & K+4\mu/3 & K-2\mu/3 & 0 & 0 & 0 \\ K-2\mu/3 & K-2\mu/3 & K+4\mu/3 & 0 & 0 & 0 \\ 0 & 0 & 0 & \mu & 0 & 0 \\ 0 & 0 & 0 & 0 & \mu & 0 \\ 0 & 0 & 0 & 0 & 0 & \mu \end{bmatrix} \tag{25}$$

$$
\begin{aligned}
\sigma_{11}^{qrs} &= c_{1111}\sum_{i=1}^{N+1}[\dot{l}_i^q(\xi_1)\frac{d\xi_1}{dx_1}u_1^{is} + \dot{l}_i^1(\xi_2)\frac{d\xi_2}{dx_1}u_1^{qi}] \\
&+ c_{1112}\sum_{i=1}^{N+1}[\dot{l}_i^q(\xi_1)\frac{d\xi_1}{dx_1}u_2^{is} + \dot{l}_i^1(\xi_2)\frac{d\xi_2}{dx_1}u_2^{qi}] \\
&+ c_{1121}\sum_{i=1}^{N+1}[\dot{l}_i^q(\xi_1)\frac{d\xi_1}{dx_2}u_1^{is} + \dot{l}_i^1(\xi_2)\frac{d\xi_2}{dx_2}u_1^{qi}] \\
&+ c_{1122}\sum_{i=1}^{N+1}[\dot{l}_i^q(\xi_1)\frac{d\xi_1}{dx_2}u_2^{is} + \dot{l}_i^1(\xi_2)\frac{d\xi_2}{dx_2}u_2^{qi}] \\
\sigma_{12}^{qrs} &= c_{1211}\sum_{i=1}^{N+1}[\dot{l}_i^q(\xi_1)\frac{d\xi_1}{dx_1}u_1^{is} + \dot{l}_i^1(\xi_2)\frac{d\xi_2}{dx_1}u_1^{qi}] \\
&+ c_{1212}\sum_{i=1}^{N+1}[\dot{l}_i^q(\xi_1)\frac{d\xi_1}{dx_1}u_2^{is} + \dot{l}_i^1(\xi_2)\frac{d\xi_2}{dx_1}u_2^{qi}] \\
&+ c_{1221}\sum_{i=1}^{N+1}[\dot{l}_i^q(\xi_1)\frac{d\xi_1}{dx_2}u_1^{is} + \dot{l}_i^1(\xi_2)\frac{d\xi_2}{dx_2}u_1^{qi}] \\
&+ c_{1222}\sum_{i=1}^{N+1}[\dot{l}_i^q(\xi_1)\frac{d\xi_1}{dx_2}u_2^{is} + \dot{l}_i^1(\xi_2)\frac{d\xi_2}{dx_2}u_2^{qi}] \\
\sigma_{21}^{qrs} &= c_{2111}\sum_{i=1}^{N+1}[\dot{l}_i^q(\xi_1)\frac{d\xi_1}{dx_1}u_1^{is} + \dot{l}_i^1(\xi_2)\frac{d\xi_2}{dx_1}u_1^{qi}] \\
&+ c_{2112}\sum_{i=1}^{N+1}[\dot{l}_i^q(\xi_1)\frac{d\xi_1}{dx_1}u_2^{is} + \dot{l}_i^1(\xi_2)\frac{d\xi_2}{dx_1}u_2^{qi}] \\
&+ c_{2121}\sum_{i=1}^{N+1}[\dot{l}_i^q(\xi_1)\frac{d\xi_1}{dx_2}u_1^{is} + \dot{l}_i^1(\xi_2)\frac{d\xi_2}{dx_2}u_1^{qi}] \\
&+ c_{2122}\sum_{i=1}^{N+1}[\dot{l}_i^q(\xi_1)\frac{d\xi_1}{dx_2}u_2^{is} + \dot{l}_i^1(\xi_2)\frac{d\xi_2}{dx_2}u_2^{qi}] \\
\sigma_{22}^{qrs} &= c_{2211}\sum_{i=1}^{N+1}[\dot{l}_i^q(\xi_1)\frac{d\xi_1}{dx_1}u_1^{is} + \dot{l}_i^1(\xi_2)\frac{d\xi_2}{dx_1}u_1^{qi}] \\
&+ c_{2212}\sum_{i=1}^{N+1}[\dot{l}_i^q(\xi_1)\frac{d\xi_1}{dx_1}u_2^{is} + \dot{l}_i^1(\xi_2)\frac{d\xi_2}{dx_1}u_2^{qi}] \\
&+ c_{2221}\sum_{i=1}^{N+1}[\dot{l}_i^q(\xi_1)\frac{d\xi_1}{dx_2}u_1^{is} + \dot{l}_i^1(\xi_2)\frac{d\xi_2}{dx_2}u_1^{qi}] \\
&+ c_{2222}\sum_{i=1}^{N+1}[\dot{l}_i^q(\xi_1)\frac{d\xi_1}{dx_2}u_2^{is} + \dot{l}_i^1(\xi_2)\frac{d\xi_2}{dx_2}u_2^{qi}]
\end{aligned} \tag{26}
$$

Here for the isotropic, $K = \lambda + 2/3\mu$, so that $c_{1111} = \lambda + 2\mu$,$c_{1122} = \lambda$, $c_{1112} = c_{1121} = \mu$, therefore, Eq. (26) could be simplified by

$$
\begin{aligned}
\sigma_{11}^{qrs} &= (\lambda + 2\mu)\sum_{i=1}^{N+1}[\dot{l}_i^q(\xi_1)\frac{d\xi_1}{dx_1}u_1^{is} + \dot{l}_i^1(\xi_2)\frac{d\xi_2}{dx_1}u_1^{qi}] \\
&+\lambda\sum_{i=1}^{N+1}[\dot{l}_i^q(\xi_1)\frac{d\xi_1}{dx_2}u_2^{is} + \dot{l}_i^1(\xi_2)\frac{d\xi_2}{dx_2}u_2^{qi}] \\
\sigma_{12}^{qrs} &= \mu\sum_{i=1}^{N+1}[\dot{l}_i^q(\xi_1)\frac{d\xi_1}{dx_1}u_2^{is} + \dot{l}_i^1(\xi_2)\frac{d\xi_2}{dx_1}u_2^{qi}] \\
&+\mu\sum_{i=1}^{N+1}[\dot{l}_i^q(\xi_1)\frac{d\xi_1}{dx_2}u_1^{is} + \dot{l}_i^1(\xi_2)\frac{d\xi_2}{dx_2}u_1^{qi}] \\
\sigma_{21}^{qrs} &= \mu\sum_{i=1}^{N+1}[\dot{l}_i^q(\xi_1)\frac{d\xi_1}{dx_1}u_2^{is} + \dot{l}_i^1(\xi_2)\frac{d\xi_2}{dx_1}u_2^{qi}] \\
&+\mu\sum_{i=1}^{N+1}[\dot{l}_i^q(\xi_1)\frac{d\xi_1}{dx_2}u_1^{is} + \dot{l}_i^1(\xi_2)\frac{d\xi_2}{dx_2}u_1^{qi}] \\
\sigma_{22}^{qrs} &= \lambda\sum_{i=1}^{N+1}[\dot{l}_i^q(\xi_1)\frac{d\xi_1}{dx_1}u_1^{is} + \dot{l}_i^1(\xi_2)\frac{d\xi_2}{dx_1}u_1^{qi}] \\
&+(\lambda + 2\mu)\sum_{i=1}^{N+1}[\dot{l}_i^q(\xi_1)\frac{d\xi_1}{dx_2}u_2^{is} + \dot{l}_i^1(\xi_2)\frac{d\xi_2}{dx_2}u_2^{qi}]
\end{aligned}
\tag{27}
$$

3. Isotropic weak solutions for the PS decoupling

Given the equation for separating amplitude-preserved vector S wave fields as

$$
\mathbf{u^s} = -\nabla \times (v_s^2 \nabla \times \mathbf{u}) \quad . \tag{28}
$$

To get a weak solution, we use the test function as

$$
\int_{G_e} \mathbf{w} \cdot \mathbf{u^s} d^3\mathbf{x} = -\int_{G_e} \mathbf{w} \cdot \nabla \times (v_s^2 \nabla \times \mathbf{u}) d^3\mathbf{x} \quad . \tag{29}
$$

Since $a \cdot (b \times c) = b \cdot (c \times a) = c \cdot (a \times b)$, and note $\Phi := v_s^2 \nabla \times \mathbf{u}$ therefore,

$$
\begin{aligned}
\int_{G_e} \mathbf{w} \cdot \mathbf{u^s} d^3\mathbf{x} &= -\int_{G_e} \mathbf{w} \cdot (\nabla \times \mathbf{\Phi}) d^3\mathbf{x} \\
&= \int_{G_e} \nabla \times \mathbf{w} \cdot \mathbf{\Phi} d^3\mathbf{x} \quad .
\end{aligned}
\tag{30}
$$

For any test function, $w_{ijk}^p = \psi_{ijk}\mathbf{e}_p$, the right hand of Eq. (1.30) has the form of

$$
\begin{aligned}
\mathbb{F}_{qrs}(\Phi)_p :=& \int_{G_e} \nabla \times \psi_{qrs}\mathbf{e}_p \cdot \bar{\mathbf{\Phi}} d^3\mathbf{x} \\
=& \int_{G_e} \sum_{m,n,p=1}^{3} \epsilon_{mnp} \frac{\partial \psi_{qrs} e_p}{\partial x_n} \Phi_m d^3\mathbf{x} \\
=& \int_{G_e} \sum_{m,n,p=1}^{3} \epsilon_{mnp} \dot{l}_q(\xi_1) l_r(\xi_2) l_s(\xi_3) \frac{\partial \xi_1}{\partial x_n}(\xi) \Phi_m e_p J(\xi) d^3\xi \\
&+ \int_{G_e} \sum_{m,n,p=1}^{3} \epsilon_{mnp} l_q(\xi_1) \dot{l}_r(\xi_2) l_s(\xi_3) \frac{\partial \xi_2}{\partial x_n}(\xi) \Phi_m e_p J(\xi) d^3\xi \\
&+ \int_{G_e} \sum_{m,n,p=1}^{3} \epsilon_{mnp} l_q(\xi_1) l_r(\xi_2) \dot{l}_s(\xi_3) \frac{\partial \xi_3}{\partial x_n}(\xi) \Phi_m e_p J(\xi) d^3\xi \\
=& \sum_{m,n,p=1}^{3} \epsilon_{mnp} \sum_{i=1}^{N+1} w_i w_r w_s \dot{l}_q^i(\xi_1) \frac{\partial \xi_1}{\partial x_n}(\xi^{irs}) \Phi_m e_p J(\xi^{irs}) d^3\xi \\
&+ \sum_{m,n,p=1}^{3} \epsilon_{mnp} \sum_{i=1}^{N+1} w_q w_i w_s \dot{l}_q^i(\xi_2) \frac{\partial \xi_2}{\partial x_n}(\xi^{qis}) \Phi_m e_p J(\xi^{qis}) d^3\xi \\
&+ \sum_{m,n,p=1}^{3} \epsilon_{mnp} \sum_{i=1}^{N+1} w_q w_r w_i \dot{l}_q^i(\xi_3) \frac{\partial \xi_3}{\partial x_n}(\xi^{qri}) \Phi_m e_p J(\xi^{qri}) d^3\xi \quad .
\end{aligned} \tag{31}
$$

Now let's solve $\Phi := v_s^2 \nabla \times \mathbf{u}$ by neglecting the v_s^2 term, similarly, for any test function,

$$
\begin{aligned}
\mathbb{F}_{qrs}[\nabla\times\mathbf{u}]_m &:= \int_{G_e}\mathbf{w}\cdot\nabla\times\mathbf{u}d^3\mathbf{x}\\
&= \int_{G_e}[\psi_{qrs}\mathbf{e}]_m\cdot[\nabla\times\mathbf{u}]_m d^3\mathbf{x}\\
&= \int_{G_e}[\psi_{qrs}\mathbf{e}]_m\cdot[\sum_{m,n,p=1}^{3}\epsilon_{mnp}\frac{\partial u_p}{\partial x_n}e_m]d^3\mathbf{x}\\
&= \int_{G_e}\sum_{m,n,p=1}^{3}\psi_{qrs}\epsilon_{mnp}\frac{\partial u_p}{\partial x_n}e_m d^3\mathbf{x}\\
&= \int_{G_e}\sum_{m,n,p=1}^{3}\psi_{qrs}\epsilon_{mnp}[\frac{\partial u_p}{\partial \xi_1}\frac{\partial \xi_1}{\partial x_n}+\frac{\partial u_p}{\partial \xi_2}\frac{\partial \xi_2}{\partial x_n}+\frac{\partial u_p}{\partial \xi_3}\frac{\partial \xi_3}{\partial x_n}]e_m J(\xi)d^3\xi\\
&= \int_{G_e}\sum_{m,n,p=1}^{3}\psi_{qrs}\epsilon_{mnp}e_m J(\xi)\sum_{i,j,k=1}^{N+1}\dot{l}_i(\xi_1)l_j(\xi_2)l_k(\xi_3)\frac{\partial \xi_1}{\partial x_n}(\xi)d^3\xi\\
&+ \int_{G_e}\sum_{m,n,p=1}^{3}\psi_{qrs}\epsilon_{mnp}e_m J(\xi)\sum_{i,j,k=1}^{N+1}l_i(\xi_1)\dot{l}_j(\xi_2)l_k(\xi_3)\frac{\partial \xi_2}{\partial x_n}(\xi)d^3\xi\\
&+ \int_{G_e}\sum_{m,n,p=1}^{3}\psi_{qrs}\epsilon_{mnp}e_m J(\xi)\sum_{i,j,k=1}^{N+1}l_i(\xi_1)l_j(\xi_2)\dot{l}_k(\xi_3)\frac{\partial \xi_3}{\partial x_n}(\xi)d^3\xi\\
&= \sum_{f,g,h=1}^{N+1}w_f w_g w_h l_q^f(\xi_1)l_r^g(\xi_2)l_s^h(\xi_3)\sum_{m,n,p=1}^{3}\epsilon_{mnp}e_m J(\xi^{fgh})\sum_{i,j,k=1}^{N+1}\dot{l}_i^f(\xi_1)l_j^g(\xi_2)l_k^h(\xi_3)\frac{\partial \xi_1}{\partial x_n}(\xi)\\
&+ \sum_{f,g,h=1}^{N+1}w_f w_g w_h l_q^f(\xi_1)l_r^g(\xi_2)l_s^h(\xi_3)\sum_{m,n,p=1}^{3}\epsilon_{mnp}e_m J(\xi^{fgh})\sum_{i,j,k=1}^{N+1}l_i^f(\xi_1)\dot{l}_j^g(\xi_2)l_k^h(\xi_3)\frac{\partial \xi_2}{\partial x_n}(\xi)\\
&+ \sum_{f,g,h=1}^{N+1}w_f w_g w_h l_q^f(\xi_1)l_r^g(\xi_2)l_s^h(\xi_3)\sum_{m,n,p=1}^{3}\epsilon_{mnp}e_m J(\xi^{fgh})\sum_{i,j,k=1}^{N+1}l_i^f(\xi_1)l_j^g(\xi_2)\dot{l}_k^h(\xi_3)\frac{\partial \xi_3}{\partial x_n}(\xi)\\
&= w_q w_r w_s\sum_{m,n,p=1}^{3}\epsilon_{mnp}e_m J(\xi^{qrs})\sum_{i=1}^{N+1}\dot{l}_i^q(\xi_1)\frac{\partial \xi_1}{\partial x_n}(\xi_{qrs})\\
&+ w_q w_r w_s\sum_{m,n,p=1}^{3}\epsilon_{mnp}e_m J(\xi^{qrs})\sum_{i=1}^{N+1}\dot{l}_i^r(\xi_2)\frac{\partial \xi_2}{\partial x_n}(\xi_{qrs})\\
&+ w_q w_r w_s\sum_{m,n,p=1}^{3}\epsilon_{mnp}e_m J(\xi^{qrs})\sum_{i=1}^{N+1}\dot{l}_i^s(\xi_3)\frac{\partial \xi_3}{\partial x_n}(\xi_{qrs}) \quad .
\end{aligned}
\tag{32}
$$

If given the equation for separating amplitude-preserved vector P wave fields as

$$\mathbf{u}^{\mathbf{P}} = \nabla(v_p^2\nabla\cdot\mathbf{u}) \quad , \tag{33}$$

then the weak solution could be

$$\int_{G_e} \mathbf{w} \cdot \mathbf{u^p} d^3\mathbf{x} = \int_{G_e} \mathbf{w} \cdot \nabla(v_p^2 \nabla \cdot \mathbf{u}) d^3\mathbf{x} \quad . \tag{34}$$

According to the Wiki ($https : //en.m.wikipedia.org/wiki/Vector_calculus_identities$), the integral by parts of the vector dot product is in the form of

$$\iiint \alpha \nabla \cdot A d\mathbf{V} = \oint_{\partial V} \alpha A \cdot d\mathbf{S} - \iiint A \cdot \nabla \alpha d\mathbf{V} \quad . \tag{35}$$

According to Eq. (3), we get the integral by paths of Eq. (34) in the form of

$$\int_{G_e} \mathbf{w} \cdot \mathbf{u^p} d^3\mathbf{x} = \int_{\partial G} \alpha \mathbf{w} \cdot \mathbf{n} d^2\mathbf{x} - \int_{G_e} \alpha \nabla \cdot \mathbf{w} \quad . \tag{36}$$

If we take the boundary condition into the first term of the last equation, we have

$$\int_{G_e} \mathbf{w} \cdot \mathbf{u^p} d^3\mathbf{x} = - \int_{G_e} \alpha \nabla \cdot \mathbf{w} \quad , \tag{37}$$

where we note $\alpha = v_p^2 \nabla \cdot u$. Now let's try to get the weak form solution,

$$
\begin{aligned}
\mathbb{F}_{qrs}[\nabla \cdot \mathbf{w}]_p := \int_{G_e} [\nabla \cdot (\psi_{qrs} \mathbf{e_p})] \alpha^{qrs} d^3\mathbf{x} \\
= \int_{G_e} \frac{\partial \psi^{qrs}}{\partial x_p} \alpha d^3\mathbf{x} \\
= \int_{G_e} \dot{l}_q l_r l_s \frac{\partial \xi_1}{\partial x_p} \alpha(\xi) J(\xi) d^3\xi \\
+ \int_{G_e} l_q \dot{l}_r l_s \frac{\partial \xi_2}{\partial x_p} \alpha(\xi) J(\xi) d^3\xi \\
+ \int_{G_e} l_q l_r \dot{l}_s \frac{\partial \xi_3}{\partial x_p} \alpha(\xi) J(\xi) d^3\xi \\
= \sum_{ijk}^{N+1} w_i w_j w_k \dot{l}_q^i l_r^j l_s^k \frac{\partial \xi_1}{\partial x_p}(\xi^{ijk}) \alpha(\xi^{ijk}) J(\xi^{ijk}) \\
+ \sum_{ijk}^{N+1} w_i w_j w_k l_q^i \dot{l}_r^j l_s^k \frac{\partial \xi_2}{\partial x_p}(\xi^{ijk}) \alpha(\xi^{ijk}) J(\xi^{ijk}) \\
+ \sum_{ijk}^{N+1} w_i w_j w_k l_q^i \dot{l}_r^j l_s^k \frac{\partial \xi_3}{\partial x_p}(\xi^{ijk}) \alpha(\xi^{ijk}) J(\xi^{ijk}) \\
= \sum_{i=1}^{N+1} w_i w_r w_s \dot{l}_q^i \frac{\partial \xi_1}{\partial x_p}(\xi^{irs}) \alpha(\xi^{irs}) J(\xi^{irs}) \\
+ \sum_{i=1}^{N+1} w_i w_r w_s \dot{l}_r^i \frac{\partial \xi_2}{\partial x_p}(\xi^{qis}) \alpha(\xi^{qis}) J(\xi^{irs}) \\
+ \sum_{i=1}^{N+1} w_i w_r w_s \dot{l}_s^i \frac{\partial \xi_3}{\partial x_p}(\xi^{qri}) \alpha(\xi^{qri}) J(\xi^{irs}) \quad .\mathring{a}
\end{aligned}
\tag{38}
$$

It is not necessary to get this weak form of this term $\alpha = v_p^2 \nabla \cdot u$, since it is fairly easy.

References

Fichtner, A. (2010). *Full seismic waveform modelling and inversion.* Springer Science & Business Media.